UNIVERSITÀ
DEGLI STUDI
DI PADOVA

DEPARTMENT OF CHEMICAL SCIENCE

Ph.D. SCHOOL IN MOLECULAR SCIENCE

CHEMICAL SCIENCE

XXIII CYCLE

OXYGEN OPTICAL SENSORS BASED ON LUMINESCENCE QUENCHING OF ORGANOMETALLIC COMPLEXES EMBEDDED IN POLIMERIC MATRIXES

Supervisor: Ch.mo Prof. Paolo Pastore

School Director: Ch.mo Prof. Maurizio Casarin

Ph.D. Student: Andrea Mondin

INDEX

1. ABSTRACT

1.1 ITALIANO

L'argomento di ricerca sviluppato durante la Scuola di Dottorato è stato lo studio di sensori ottici per il monitoraggio dell'ossigeno molecolare. Il principio di funzionamento di questi sensori è dato dallo spegnimento della luminescenza di luminofori metallorganici inglobati in una matrice polimerica. La luminescenza viene indotta per eccitazione del luminoforo con una sorgente LED e è raccolta da un rilevatore a fotodiodo. I sensori basati su questo principio costituiscono una valida alternativa ai sensori elettrochimici attualmente in uso, in quanto permettono misure "*in situ*" e in tempo reale, ed in modo non distruttivo. Sono inoltre più robusti limitando sia la necessità di frequenti calibrazioni che la frequente sostituzione delle membrane.

È stata focalizzata l'attenzione principalmente sui sensori che si basano sulla misura delle intensità luminose, piuttosto che su quella dei tempi di vita, in quanto più promettenti per realizzare sensori a basso costo adatti per applicazioni industriali. L'obiettivo finale è quello di realizzare un sensore robusto ed economico, in grado di misurare l'ossigeno in un ampio intervallo di concentrazioni e di sopportare temperature fino ai 90°C, condizione per la quale non esistono a tutt'oggi prodotti commerciali. Lo spegnimento della luminescenza è legato alla quantità di ossigeno molecolare a seguito di *quenching,* secondo il modello di Stern-Volmer (SV), da cui si ottiene la seguente relazione:

$$\frac{I_0}{I} = \frac{\tau_0}{\tau} = 1 + K'_{SV} \cdot \%O_2$$

dove con I_0/I si indica il rapporto tra l'intensità luminosa emessa in assenza e in presenza di ossigeno e con τ_0/τ l'analogo rapporto tra i tempi di vita nelle due situazioni. Questo rapporto è proporzionale alla percentuale di ossigeno $\%O_2$ secondo una costante K'_{SV} che risulta proporzionale al tempo di vita in assenza di ossigeno, τ_0, al coefficiente di diffusione dell'ossigeno nella membrana, D_{O_2} e alla sua solubilità, s_{O_2}.

Al fine di ottimizzare le caratteristiche analitiche delle membrane sensibili sono stati testati svariati luminofori con differenti tempi di vita in assenza di ossigeno: Rutenio *tris*(4,7-difenil-1,10-fenantrolina) (Ru(dpp), τ_0=6μs), Platino 5,10,15,20-*tetra*fenilporfirina (PtTPP, τ_0=50μs), Platino-5,10,15,20-*tetra*(pentafluorofenil)porfirina (PtTFPP, τ_0=70μs), Palladio5,10,15,20-*tetra*(pentafluorofenil)porfirina (PdTFPP, τ_0=850μs) e Palladio2,3,7,8,12,13,17,18-*otta*etilporfirina (PdOEP τ_0=990μs). Questi luminofori sono stati

inglobati all'interno di polimeri organici: polisulfone (PSF) e polivinilcloruro (PVC). Sono state ottimizzate le procedure di deposizione sia per *spin-coating* che per *dip-coating*, .

E' stata introdotta una modifica al modello di SV, al fine di scorporare dal valore di emissione sperimentale i contributi non contemplati dal modello di SV. In particolare la nuova procedura permette di scorporare il contributo di emissione attribuibile alla parte di luminoforo all'interno della membrana non raggiungibile dall'ossigeno. Questa modifica ha permesso di constatare che la curvatura della calibrazione di SV documentata in diversi lavori riportati in letteratura è dovuta al citato contributo. Operando in questo modo è stata dimostrata la linearità del modello di SV per tre differenti tipologie di membrane utilizzate, contenenti differenti luminofori (Ru(dpp), PtTPP e PdTFPP) inglobati in PSF e caratterizzate da differenti K'_{SV} (0.014, 0.136, 1.79).

È stato poi analizzato l'effetto della deriva dell'intensità luminosa nel tempo, dovuta a fenomeni di degradazione del luminoforo, sviluppando un algoritmo di correzione di tali effetti. È stato osservato che il complesso del rutenio presenta una deriva significativa del segnale di $-1{,}01\cdot10^{-4}\,s^{-1}$ a 30 °C, mentre per tutte le porfirine essa è risultata di due ordini di grandezza più bassa. Il problema della deriva diviene fondamentale quando si considera il funzionamento del sensore ad alte temperature, situazioni nelle quali il contributo della termodegradazione del luminoforo può diventare rilevante.

Lo studio di questi sistemi ha permesso di ricavare alcune importanti caratteristiche chimico-fisiche come le energie di attivazione dei differenti processi coinvolti. A questo scopo è stato studiato specificamente il comportamento dell'emissione di un sensore contenente PtTFPP inglobata in PSF. Dalle misure dell'andamento della costante di Stern-Volmer (K'_{SV}), dell'intensità di emissione (I_0) e del tempo di risposta (t_1) al variare della temperatura, utilizzando opportuni modelli fisici quali l'equazione di Arrhenius, sono state ricavate le energie libere di attivazione ($\Delta G^{\ddagger}$) dei processi di diffusione e di decadimento radiativo che sono risultate pari a 2.8(0.3) *kJ/mol*e e 16.5(0.5) *kJ/mol*, rispettivamente. E' stato determinato inoltre il ΔH relativo alla solubilità dell'ossigeno all'interno della membrana polimerica, risultato pari a 13(3) *kJ/mol*.

Oltre alla determinazione della sensibilità di calibrazione è stato determinato il limite massimo di misura $\%O_2^{\max}$ di differenti membrane. Le membrane con K'_{SV} elevati presentano $\%O_2^{\max}$ più basse. In particolare, per Ru(dpp)OS-PSF $\%O_2^{\max}=98$, per (PtTPP-PSF) $\%O_2^{\max}=50$ e per PdTFPP-PSF $\%O_2^{\max}=25$.

Per estendere l'intervallo di lavoro verso l'alto senza dover rinunciare completamente a un'elevata sensibilità sono state seguite due vie: 1) calibrazione dinamica; 2) sistema "bi-label".

1) La prima via sfrutta un modello di calibrazione "dinamico" che non si basa sulle intensità in condizioni di equilibrio bensì sulla forma dei profili di intensità nel tempo. E' stato dimostrato teoricamente e confermato con dati sperimentali che la forma transiente dell'intensità durante l'uscita dell'ossigeno dalla membrana ha la forma di una sigmoide. La forma di tale sigmoide è indipendente dalla concentrazione di ossigeno da cui si parte, e l'unica cosa che varia è la posizione nel tempo del punto di flesso, che può quindi essere utilizzata come grandezza sperimentale diagnostica al posto dell'intensità luminosa. Il vantaggio è che la posizione del punto di flesso è misurabile a qualunque livello di concentrazione anche per membrane molto sensibili. La verifica di questo modello è stata effettuata su membrane contenenti Ru(dpp), PtTPP o PdTFPP inglobati in PSF. E' stato dimostrato che le misure "classiche", basate sulla misura delle intensità all'equilibrio, hanno una precisione approssimativamente costante all'aumentare della $\%O_2$ e mediamente pari al 3.5, 0.7 e 0.4 %, rispettivamente. Con il modello dinamico di calibrazione essa è invece decrescente con l'aumentare della $\%O_2$. Da questo punto di vista esso è preferibile rispetto al modello classico per basse concentrazioni di ossigeno (inferiori al 97%, 9.2%, e 7.2%, per membrane contenenti Ru(dpp), PtTPP o PdTFPP, rispettivamente). Per quanto riguarda la sensibilità è stato determinato che le misure "classiche", risultano più sensibili rispetto alle misure secondo il metodo dinamico da noi sviluppato per membrane con elevate K'_{SV} e a alte $\%O_2$, mentre la situazione si inverte per basse K'_{SV} e $\%O_2$. Una sensibilità equivalente dei due metodi di misura si ottiene per $\%O_2$ pari al 60%, 6% e 2% per membrane contenenti Ru(dpp), PtTPP o PdTFPP, rispettivamente. Il metodo dinamico di calibrazione risulta quindi preferibile, oltre che per le applicazioni che richiedono un intervallo di lavoro esteso al di fuori di quello consentito dal metodo "classico", anche per misure di basse concentrazioni di ossigeno. Per contro, la misura del profilo di emissione è più laboriosa rispetto a quella della misura diretta dell'intensità emessa in condizioni e richiede l'utilizzo di un gas di riferimento (generalmente azoto), limitando le prospettive di applicazione nel campo dei sensori portatili.

2) Il secondo approccio ha portato alla realizzazione di un sensore contenente due luminofori inglobati nella stessa matrice. È stato razionalizzato il comportamento di tali sensori dal punto di vista teorico e ne sono state verificate le caratteristiche sperimentalmente per due casi studio: una miscela di Ru(dpp) e PtTPP in PSF e una di PtTPP e PdTFPP in PVC. E' stato dimostrato che, all'interno della matrice, i due luminofori si

comportano indipendentemente tra di loro. In questo modo è stato possibile ricavare un grafico di lavoro che predice le composizioni ottimali per ottenere sensori in grado di effettuare misure in un intervallo di concentrazioni prestabilite, ottimizzando la sensibilità. Nei casi considerati, volendo ottenere sensori in grado di monitorare tutto l'intervallo 0-100 $\% O_2$, sono state scelte coppie di luminofori con K'_{SV} vicine a 0.02 (K'_{SV} (Ru(dpp) in PSF)= 0.014, K'_{SV}(PtTPP in PVC)=0.019) e a 0.2 (K'_{SV} (PtTPP in PSF)= 0.14, K'_{SV}(PdTFPP in PVC)=0.27). La frazione molare ottimale dei due luminofori deve essere scelta in modo che la frazione di intensità luminosa emessa dalla PtTPP nelle due membrane sensibili sia pari a 0.45 e 0.31 per PSF e PVC, rispettivamente.

Lo studio effettuato ha permesso di realizzare un prototipo di sensore per un utilizzo commerciale. Le caratteristiche ricercate di massima robustezza e indipendenza da fattori strumentali della misura dell'intensità luminosa, sono state ottenute mediante l'uso di sorgenti pulsate per ridurre la fotodegradazione dello strato sensibile e di fibre ottiche per isolare le sorgenti LED ed i rivelatori a fotodiodo dalle variazioni di temperatura dell'ambiente di misura. È stato inoltre sviluppato un software in grado di controllare simultaneamente le diverse strumentazioni necessarie (flussimetri, generatore di segnale, termostato, ecc.) e di automatizzare sia le misure sia i calcoli necessari per gestire e monitorare il comportamento dei sensori durante i test di prova, che sono consistiti in calibrazioni in continuo per 24 ore al giorno e per 30 giorni. Al termine del test a temperatura ambiente su membrane contenenti PtTFPP in PSF si è osservato un calo medio dell'intensità luminosa del 7.1%, e un'ottima ripetibilità delle misure. A 90°C il calo di intensità per membrane analoghe è stato decisamente superiore, pari al 28.7%, ma una volta corretto con l'algoritmo sopra menzionato la ripetibilità delle misure è risultata comunque ottima.

E' stato infine realizzato e testato un prototipo di sensore adatto alle prove sul campo, in particolare per un'applicazione particolarmente complessa che prevede il monitoraggio in continuo dell'ossigeno in una massa di rifiuto umido in fase di compostaggio, nella quale si può raggiungere la temperatura di 80°C. La precisione del sensore è stata stimata dalla deviazione standard sulla mediana delle misure, ottenendo valori inferiori a 0.3% O_2 per ogni livello di concentrazione. Come stima dell'esattezza è stato preso l'errore relativo della misura di miscele a titolo noto, ottenendo valori inferiori al 4%.

1.2 ENGLISH

The subject of the present research deals with optical sensors for detecting oxygen. They are based on the quenching by oxygen of the luminescence of organometallic complexes embedded in polymeric matrixes. Excitation light is provided by a LED source and a photodiode is employed as detector. Optical sensor may substitute electrochemical ones, because they allow in situ, real time, non destructive measurements. They are more robust than electrochemical ones reducing the need of frequent calibration and membrane replacement.

Attention has been focused on luminescence-intensity-based sensors, instead of lifetime-based ones, because they are more promising to build low cost industrial sensors. Final aim is the realization of a sensor working in a wide concentration range and up to 90°C. No commercial sensor with such characteristics is available.

Stern Volmer model describes dynamic quenching, and oxygen concentration may be obtained from luminescence quenching according to:

$$\frac{I_0}{I} = \frac{\tau_0}{\tau} = 1 + K'_{SV} \cdot \%O_2$$

where I and τ are the luminescence intensity and excited-state lifetime of the luminophore, respectively. I_0 and τ_0 denote the same parameters in the absence of oxygen. The Stern Volmer constant K'_{SV} is proportional to the luminophore lifetime in the absence of oxygen, τ_0, oxygen diffusion coefficient in the polymeric membrane, D_{O_2} and oxygen solubility into the membrane, s_{O_2}.

Various luminophores having various lifetimes in the absence of oxygen has been tested in order to optimize sensor analytical performances ruthenium tris-(4,7-diphenyl-1,10-phenanthroline) bis(octylsulphate) (Ru(dpp)OS, τ_0=6μs), 5,10,15,20-Tetrakisphenyl-21*H*,23*H*-porphine platinum(II) (PtTPP, τ_0=50μs), platinum 5,10,15,20-Tetrakis(pentafluorophenyl)-21*H*,23*H*-porphine platinum(II) (PtTFPP τ_0=70μs), 5,10,15,20-Tetrakis(pentafluorophenyl)-21*H*,23*H*-porphine palladium(II) (PdTFPP, τ_0=850μs) and 2,3,7,8,12,13,17,18-Octaethyl-21*H*,23*H*-porphine palladium(II) (PdOEP, τ_0=990μs). They have been embedded in polysulfone (PSF) or polyvinylchloride (PVC). Dip-coating and spin-coating deposition procedures have been optimized. Stern Volmer model has been modified to take into account contributions to light intensity not considered in Stern Volmer model. In particular, a new procedure may determine light emission contribution from luminophores enclosed in sites where oxygen cannot enter. This correction allowed to demonstrate that curvatures of the SV calibration, often cited in the literature, come just from the cited contribution. In particular, SV calibration of three different PSF membranes embedding Ru(dpp)OS, PtTPP and PdTFPP, are linear.

Luminophore degradation influence over luminescence drift has been analyzed, and a correcting algorithm has been developed. At 30°C, Ru(dpp)OS has a luminescence drift of $-1{,}01\cdot10^{-4}$ s^{-1} whilst, for porphyrins, it has been proved negligible at room temperature. Drift becomes more influent at higher temperature, because of luminophores thermal degradation.

A PtTFPP-PSF sensor was studied in details to determine activation energies of the involved processes: Stern Volmer constant, K'_{SV}, light emitted intensity in absence of oxygen, I_0, and sensor response time, t_1, have been determined at various temperature. Employing a suitable physical model like Arrhenius equation, free activation energies, $\Delta G^{\ddagger}$, of diffusion and non radiative decays processes have been obtained. They are 2.8(0.3) *kJ/mol* and 16.5(0.5) *kJ/mol*, respectively. ΔH relative to the solubility in the membrane has been calculated too, obtaining 13(3) *kJ/mol*.

Membrane sensitivity, K'_{SV}, and maximum detectable oxygen percentage, $\%O_2^{\max}$, has been calculated for various membranes. Most sensitive membranes are characterized by lower $\%O_2^{\max}$. In particular, for Ru(dpp)OS-PSF $\%O_2^{\max}=98$, for (PtTPP-PSF) $\%O_2^{\max}=50$ and for PdTFPP-PSF $\%O_2^{\max}=25$.

In order to extend the sensor working interval to higher oxygen percentages maintaining high sensitivity, two routes have been followed: 1) dynamic calibration; 2) construction of a "bi-label" sensor.

1) The dynamic calibration model is based on the transient intensity light profiles vs. time instead of equilibrium intensities. As theoretically demonstrated and experimentally confirmed, transient intensity during oxygen exit from the membrane has a sigmoidal shape. The parameters of this sigmoid do not vary with oxygen starting concentration, and the only variable is the inflection time, which may be employed as analytical quantity instead of equilibrium light intensity. The great advantage is that inflection point time may be determined for each $\%O_2$ value even with very sensitive membranes. Experimental verification has been performed on Ru(dpp)OS, PtTPP and PdTFPP membranes embedded in PSF. The precision of "classic" measurement, based on the light intensity measurement at equilibrium, is almost constant with increasing $\%O_2$, and equal to 3.5, 0.7 e 0.4 % for Ru(dpp)OS, PtTPP and PdTFPP, respectively. In dynamic calibration model, precision decreases with increasing $\%O_2$. The dynamic model is preferable to classical one for low oxygen concentration (less than 97%, 9.2%, e 7.2%, for membranes containing Ru(dpp)OS,

PtTPP or PdTFPP, respectively). Classical measurements have been proved more sensitive than dynamic measurements for large oxygen percentages and membranes with high K'_{SV}, while the opposite is valid for low oxygen percentages and membranes with low K'_{SV}. The oxygen percentage where the two methods have the same sensitivity is 60%, 6% e 2% for Ru(dpp)OS, PtTPP and PdTFPP respectively. Dynamic calibration model is better than classical for low oxygen concentration determination and for application fields requiring an extended working range. Emission profiles measurement, however, is more complicated than equilibrium intensity measurement, and requires a reference gas (i.e. nitrogen) limiting its applicability in the portable sensor field.

2) A sensor embedding two luminophores in the same polymeric matrix ("bi-label sensor) has been prepared. Sensor behaviour has been theoretically rationalized and experimentally verified in two cases: Ru(dpp)OS and PtTPP embedded in PSF and PtTPP and PdTFPP embedded in PVC. The two luminophores have been demonstrated to behave independently into the matrix. A working graph has been obtained in order to predict optimal membrane composition to extend the working range up to required oxygen concentration optimizing sensor sensitivity. In the considered cases, for a working range from 0 to 100% $\% O_2$, luminophores with K'_{SV} near to 0.02 (K'_{SV} (Ru(dpp)OS in PSF)= 0.014, K'_{SV}(PtTPP in PVC)=0.019) and to 0.2 (K'_{SV} (PtTPP in PSF)= 0.14, K'_{SV}(PdTFPP in PVC)=0.27) have been chosen. Luminophores optimal molar fraction realized the condition that emission intensity fraction due to PtTPP is 0.45 e 0.31 of overall emitted intensity, for PSF and PVC, respectively.

A commercial sensor prototype has been built. In order to obtain a robust sensor, whose response is not influenced by most of instrumental factors, pulsed light source have been employed to reduce photodegradation and optical fibers allowed to isolate light sources and detectors from temperature change in the analyzed mixture. A software has been developed in order to control simultaneously all the instruments (flow meters, oven, pulse generator, etc.) and to automate measurements and data elaboration. Sensors embedding PtTFPP have been tested continuously 24 hours a day for one month. If test is carried at room temperature, the luminescence decrease is close to 7.1% and measurement repeatability is very good. If the same test is carried at 90 °C, luminescence decrease is equal to 28.7% but measurement repeatability, using drift corrected calibration algorithm results very good. Finally, a portable sensor has been built for a particularly complex application: oxygen continuous monitoring in composting urban wastes, with temperature up to 80°C. Sensor precision, estimated from standard deviation, results <0.3% O_2 for every oxygen concentration. Sensor accuracy, expressed as relative error of mixtures with known oxygen concentration, is always <4%.

2. INTRODUCTION

2.1 CHEMICAL SENSORS

A chemical sensor is a device that transforms chemical information, ranging from concentration of a specific sample component to total composition analysis, into an analytically useful signal[1]. Chemical sensors comprise a recognition element, a transduction element, and a signal processor capable of continuously and reversibly reporting a chemical concentration[2]. The following characteristics of chemical sensors are generally accepted. Chemical sensors should:

- Transform chemical quantities into electrical signals,
- Respond rapidly,
- Maintain their activity over a long time period,
- Be small,
- Be cheap,
- Be *specific*, i.e. they should respond exclusively to a single analyte, or at least be *selective* to a group of analytes.

The above list could be extended with, e.g., the postulation of a low detection limit, or a high sensitivity. This means that low concentration values should be detected.

2.1.1 Chemical sensor classification

Classification of sensors is accomplished in different ways. A classification following the principles of signal transduction is prevalent[3]. The following sensor groups result:

- Optical sensors, following absorbance, reflectance, luminescence, fluorescence, refractive index, optothermal effect and light scattering
- Electrochemical sensors, including voltammetric and potentiometric devices, amperometric devices and potentiometric solid electrolyte gas sensors
- Electrical sensors including metal oxide and organic semiconductors as well as electrolytic conductivity sensors

- Mass sensitive sensors, i.e. piezoelectric devices and those based on surface acoustic waves

- Magnetic sensors (mainly for oxygen) based on paramagnetic gas properties

- Thermometric sensors based on the measurement of the heat effect of a specific chemical reaction or adsorption involving the analyte.

2.1.2 Functional units in a chemical sensor

Chemical sensors contain two basic functional units: a chemical recognition system (*receptor*) and a physicochemical transducer[1, 4]. Additional elements are considered to be necessary, in particular units for signal amplification and for signal conditioning. A typical arrangement is outlined in **Figure 1**.

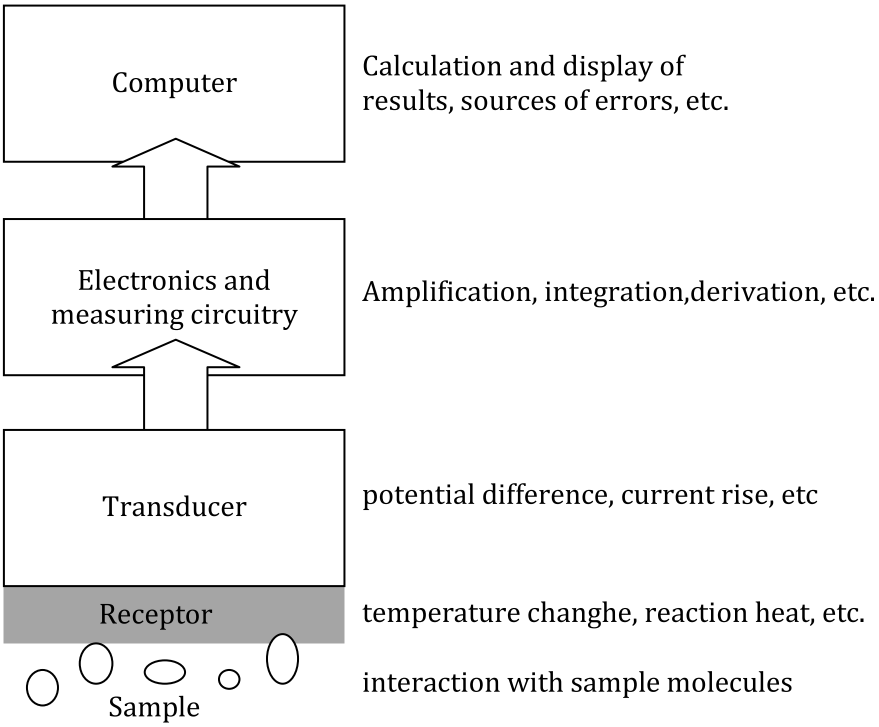

***Figure 1**. Scheme of a typical chemical sensor system*

In the majority of chemical sensors, the receptor interacts with analyte molecules. As a result, its properties are changed in such a way that the appending transducer can gain an electrical signal. The receptor function is fulfilled in many cases by a thin layer which is able to interact with analyte molecules, catalyze a reaction selectively, or participate in a chemical equilibrium together with the analyte. Receptor layers can respond selectively to particular substances or to a group of substances. The term molecular recognition is used to describe this behaviour. The transducer transforms the analyte concentration value into an electric quantity: voltage, current or resistance.

2.1.3 Analytical parameters of chemical sensors

Chemical sensor performance can be characterized by using various static and dynamic parameters[5]:

- *Sensitivity*: variation of the measurement signal per analyte concentration unit, i.e. the slope of the calibration graph.
- *Detection limit*: the lowest analyte quantity that can be distinguished from the absence of that substance (a blank value) within a stated confidence limit.
- *Quantification limit*: the smallest analyte concentration that can be determined with acceptable precision (repeatability) and accuracy under the stated conditions.
- *Dynamic range*: the concentration range between the detection limit and the upper limiting concentration.
- *Selectivity*: an expression of whether a sensor responds selectively to a group of analytes or even specifically to a single analyte. Quantitative expressions of selectivity exist for different types of sensors.
- *Linearity*: the relative deviation of an experimentally determined calibration graph from an ideal straight line. Usually values for linearity are specified for a definite concentration range.
- *Resolution*: the lowest concentration difference which can be distinguished when the composition is varied continuously. This parameter is important chiefly for detectors in flowing streams.
- *Response time*: the time for a sensor to respond from zero concentration to a step change in concentration. Usually specified as the time to rise to a definite ratio of the final value. Thus, e.g. the value of t_{99} represents the time necessary to reach 99 percent of the full-scale output. The elapsed time until 63 percent of the final value represents the time constant.
- *Hysteresis*: the maximum difference in output when the value is approached with (a) an increasing and (b) a decreasing analyte concentration range. It is given as a percentage of full-scale output.

- *Stability*: the ability of the sensor to maintain its performance for a certain period of time. As a measure of stability, drift values are used, e.g. the signal variation for zero concentration.
- *Life cycle*: the length of time over which the sensor will operate. The maximum storage time (shelf life) must be distinguished from the maximum operating life. The latter can be specified either for continuous operation or for repeated on-off cycles.

2.2 OXYGEN SENSORS

Oxygen is involved in many chemical and biochemical reactions and its determination is important in many fields like environmental and industrial monitoring, biotechnology,[6] food industry[7] and medicine.[8] For this reason oxygen has to be monitored at various concentration levels: from trace analysis[9] in the control of hydrogen electrolytes for fuel cells[10] or in wine ageing,[11] to higher concentrations as in bio-mass transformation[12] or in green chemistry reactions.[13] Several sensors have been developed for oxygen concentration determination.

2.2.1 Clark amperometric sensor

The most common oxygen amperometric sensor has been developed in 1956 by Clark who placed a working and a counter electrode behind a gas-permeable membrane holding an internal electrolyte solution. This concept has since been widely accepted and this type of oxygen sensor is frequently called a Clark electrode[14,15]. It consists (**Figure 2**) of a working electrode, a platinum disc cathode(1) inserted in a cylindrical insulator (5), and a silver ring anode (2) placed around the insulator. Clark electrode is immersed in a KCl solution (4). The working electrode is located behind a thin polymeric membrane, usually a ~20 μm polyethylene or polytetrafluoroethylene film (4), separated from the sample by only a thin layer of electrolyte solution (~10 μm) in order to achieve a fast response. When sensor is inserted in sample solution, oxygen diffuse into the polymeric membrane and KCl solution, reaching the platinum cathode where it is reduced according to reactions:

$$O_2 + 4H^+ + 4e^- \leftrightarrows 2\mathrm{H_2O} \quad (1)$$

or

$$O_2 + 2\mathrm{H_2O} + 4e^- \leftrightarrows 4\mathrm{OH^-} \quad (2)$$

depending on *pH* of electrolyte solution. On the silver anode oxidation occurs:

$$Ag_{(s)} + Cl^- \leftrightarrows AgCl_{(s)} + e^- \qquad (3)$$

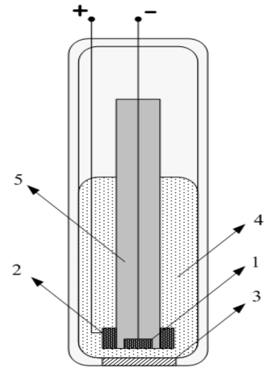

***Figure 2**. Clark electrode: 1)platinum disc cathode; 2)silver ring anode; 3)oxygen permeable polymeric membrane; 4)KCl electrolyte solution; 5)insulator cylinder*

The flux of the analyte to the electrode surface and therefore the current can be derived from the diffusion coefficient and the concentration gradient using Fick's law of diffusion. It is usually possible to employ the so-called Nernst approximation where the concentration (C) is taken to linearly decrease from a certain distance (δ) where the concentration corresponds to the bulk of the sample (C_∞) to a concentration of zero on the electrode surface itself, as illustrated in **Figure 3**.

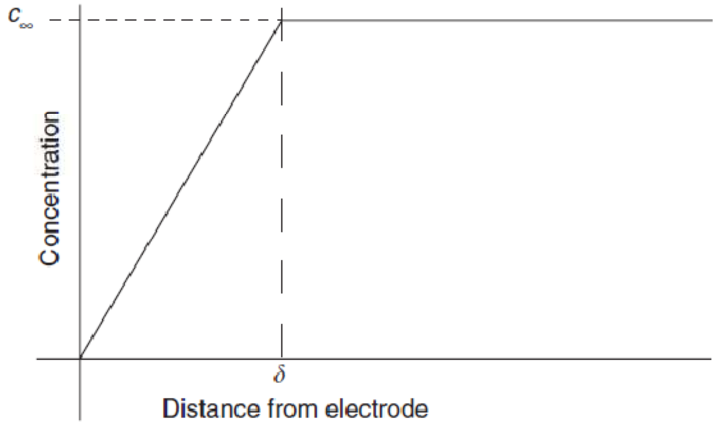

***Figure 3**. Concentration profile at electrode surface according to the Nernst approximation. c_∞ is the concentration in the bulk of the sample and δ the distance from the electrode to which the concentrations depleted*

The current is then given by the following combination of Fick's law of diffusion and the Faraday equation:

$$i = nFD\frac{C_\infty}{\delta} \qquad (4)$$

where i is the measured current, n the number of electrons exchanged in the redox reaction, F the Faraday constant, and D the analyte diffusion coefficient. From this the current is linearly dependent on the concentration in the bulk of the solution. Main advantage of Clark-type electrodes are the linear response over almost four orders of magnitude and the response time, expressed as the time required to reach 90% of the final change in current (t_{90}), usually equal to 15–20 s; however, it is necessary to wait for 1-2 minutes to obtain a stable reading. Clark sensor is quite expensive due to high maintenance costs, because membrane and electrolyte have to be replaced quite often. Moreover it cannot be employed for oxygen determination in dry gases, because of the fast evaporation of electrolyte solution through the membrane, and it requires oxygen consumption, making Clark sensor unsuitable for many applications.

2.2.2 Zirconia potentiometric sensor

Potentiometric solid state sensor are mainly employed for high temperature analysis, like in automotive exhaust or industrial emissions. They use ceramic materials as electrolytes: most common one is YSZ, Yttria (Y_2O_3) Stabilized Zirconia (ZrO_2),[15, 16] in wich O^{2-} transport is granted by oxide ion vacancy due to yttria doping. A scheme of a YSZ sensor is shown in **Figure 4**. In its most common form, the sensor consists of a thimble shaped non-porous ZrO_2 ceramic with porous inner and outer metallic (typically Pt) electrodes. The inner electrode is exposed to the reference gas (air) and the outer electrode is in contact with the measurement gas mixture (e.g. exhaust gas). The outer electrode is covered with a porous coating (e.g. spinel) preventing sensor from erosion and helping in the `equilibration' of the gas in proximity of the electrode. Oxygen molecules, adsorbed by the porous electrodes, dissociate in atomic oxygen. Oxygen atoms diffuse through the electrodes thickness and reach the triple phase boundary (TPB) between electrode, solid electrolyte and gas. There, electron transfer reaction takes place producing O^{2-}.

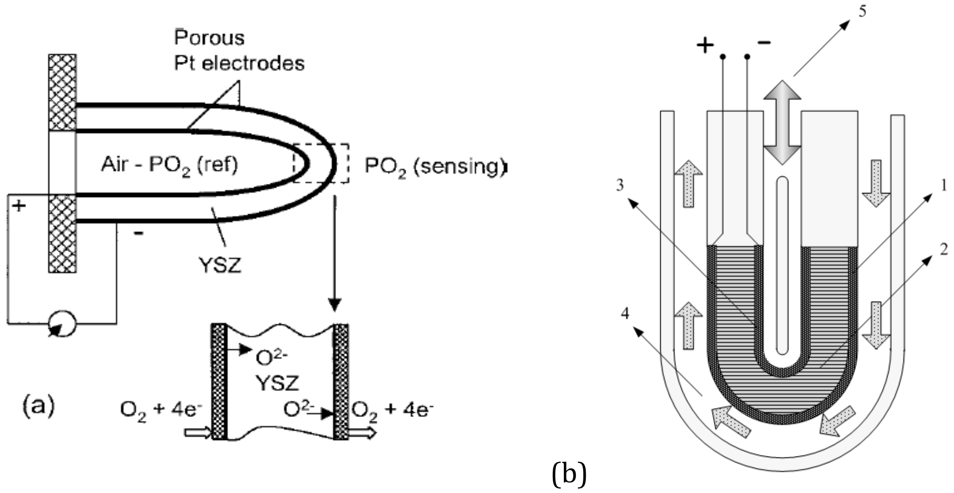

(b)

Figure 4. *a) YSZ sensor scheme and electrochemical reaction b) sensor components 1) porous platinum cathode 2) ZrO2/Y2O3 solid electrolyte 3) porous platinum anode 4) sampled gas mixture 5) reference gas mixture*

An emf, *ΔE,* develops between the sensor electrodes when the oxygen partial pressure in the measurement gas, P_{O_2}, differs from the concentration in the air, $P_{O_2,ref}$, which is used as the reference gas. According to Nernst equation we may write:

$$\Delta E = \left(\frac{RT}{4F}\right)\ln\left(\frac{P_{O_2,ref}}{P_{O_2}}\right) \tag{5}$$

where *T* is the working temperature, *R* is the ideal gas constant and *F* is the Faraday constant. YSZ sensor give reproducible and accurate measures even at ppm range, but its cost is high and it operates at high temperatures (700–900°C). Several attempts have been made to lower the operating temperature[17,18] but none of these sensors can work under 300°C. Moreover, sensors can be damaged by a reducing atmosphere, because of the partial reduction of titania and zirconia.[19]

2.2.3 Magnetic sensor

Molecular oxygen is paramegnetic. If it is placed in a sample holder and immersed in a strong and non uniform magnetic field, it is attracted by the stronger field, imparting a rotation detectable with a torsion balance or an optical system. Magnetic sensor are very accurate and suffer no interference, but they are very expensive and hardly miniaturizable.[15, 20]

2.3 OPTICAL OXYGEN SENSORS

The field of optical chemical sensors has been a growing research area over the last three decades. A lot of books and review articles has been published by experts in the field who have highlighted the advantages of optical sensing over other transduction methods.[21,22] Optical oxygen sensors are known since 1968[23] but have become more and more attractive in last two decades[24] owing to synthesis and development of new materials and for the possibility to confine them inside very thin, versatile polymeric membranes. In particular, optical systems are attractive because they don't consume oxygen, are stable and less poisonable[25] than other devices such as amperometric ones. Optical sensor functioning is based on the luminescence quenching of suitable luminophores in the presence of oxygen. According to the Stern-Volmer (SV) model, film sensitivity is influenced by the luminophore life-time. Luminophores are commonly embedded in polymeric organic[26-28] inorganic[29] or hybrid[30] matrices. More exotics matrices, like proteins,[31] are also employed. Commonly employed luminophores are Ruthenium phenanthrolines[32] or metalloporphyrins.[24,33-35]

2.3.1 Dynamic quenching: Stern-Volmer model

Luminescence dynamic quenching is a bimolecular process leading to a non radiative decay of an excited luminophore without any chemical reaction. It consists in an energy transfer from the luminophore to a quencher (oxygen, in our case) causing a reduction in overall emitted light intensity. Stern-Volmer model assumes the following kinetic scheme

$$M + h\nu \xrightarrow{k_{abs}} M^* \tag{6}$$

$$M^* \xrightarrow{k_f^0} M + h\nu' \qquad v_f^0 = k_f^0 \cdot [M^*] \tag{7}$$

$$M^* \xrightarrow{\sum k_i} M + heat \qquad v_i = \sum k_i \cdot [M^*] \tag{8}$$

$$M^* + Q \xrightarrow{k_q} M + Q^* \qquad v_q = k_q \cdot [M^*] \cdot [Q] \tag{9}$$

In this scheme, M and M^* are the luminophore in the fundamental and excited state, respectively; *hv* and *hv*' are the photon energies absorbed and emitted, respectively; k_{abs}, k_f^0, k_i and k_q are kinetic constants relative to excitation, radiative and non radiative decay and quenching processes. Dynamic quenching therefore provides a decay process competitive with radiative and non radiative ones. Applying the steady state theory to M^* we may define luminescence quantum yield, Φ_f, as

$$\Phi_f = \frac{k_f^0}{k_f^0 + \sum k_i + k_q[O_2]} \tag{10}$$

If $[O_2]=0$ Equation 10 becomes

$$\Phi_f^0 = \frac{k_f^0}{k_f^0 + \sum k_i} \tag{11}$$

The ratio between Equation 10 and 11 is:

$$\frac{\Phi_f^0}{\Phi_f} = 1 + \frac{1}{k_f^0 + \sum k_i} \cdot k_q[O_2] \tag{12}$$

Remembering that lifetime in absence of oxygen is expressed by Equation 13:

$$\tau_0 = \frac{1}{k_f^0 + \sum k_i} \tag{13}$$

we may obtain Stern-Volmer equation (Equation 14) where the Stern-Volmer constant is defined as $K_{SV} = \tau_0 k_q$

$$\frac{\Phi_f^0}{\Phi_f} = 1 + \tau_0 k_q [O_2] = 1 + K_{SV}[O_2] \tag{14}$$

If polymeric matrix can be assumed as homogeneous and there is only one luminophore, we may obtain simpler formulations of the Stern-Volmer equation:

$$\frac{I_0}{I} = 1 + K_{SV}[O_2] \tag{15}$$

$$\frac{\tau_0}{\tau} = 1 + K_{SV}[O_2] \tag{16}$$

where I and τ are the luminescence intensity and excited-state lifetime of the luminophore, respectively. I_0 and τ_0 denote the absence of oxygen. Consequently it is possible to determine oxygen concentration from the luminophore lifetime or from the emission intensity measurement, in a simpler way compared to the florescence quantum yield evaluation.

The oxygen amount may be determined by measuring either the emission intensity[36,37] or the lifetime of the luminophore. Lifetimes may be determined from the decay curve[38] or by phase-modulation measurements.[39] Lifetime measurements are more accurate; they are not influenced by signal drift but require more complicated instrumentation and measurements. On the other hand, light intensity measurement is simpler and may be useful to build cheaper oxygen sensors.

Oxygen concentration in Equations 15 and 16 can be expressed as function of its partial pressure, p_{O_2}, and its solubility in the polymeric matrix, σ_{O_2}, according to Henry's law:

$$[O_2] = \sigma_{O_2} \cdot p_{O_2} \tag{17}$$

Inserting Equation 17 in Equations 15 and 16 we obtain

$$\frac{I_0}{I} = \frac{\tau_0}{\tau} = 1 + K_{SV}\sigma_{O_2} p_{O_2} \tag{18}$$

It is useful to express oxygen concentration as percentage, $\%O_2$, as in Equation 19

$$p_{O_2} = \frac{p_{tot} \cdot \% O_2}{100} \tag{19}$$

where p_{tot} is the total pressure. Stern-Volmer equation becomes:

$$\frac{I_0}{I} = \frac{\tau_0}{\tau} = 1 + K_{SV} \cdot \sigma_{O_2} \cdot \frac{p_{tot}}{100} \cdot \%O_2 \tag{20}$$

Defining $K'_{SV} = K_{SV} \cdot \sigma_{O_2} \cdot \frac{p_{tot}}{100}$ we obtain the most common form of Stern Volmer equation:

$$\frac{I_0}{I} = \frac{\tau_0}{\tau} = 1 + K'_{SV} \cdot \%O_2 \tag{21}$$

When luminophores are embedded in polymeric matrixes, quenching reaction is diffusion controlled and quenching kinetic constant, k_q, result proportional to oxygen diffusion kinetic constant,

$$k_q = \alpha k_d \tag{22}$$

where α is the probability of the quenching reaction to occur. k_d may be expressed according to Smoluchowski equation

$$k_d = \frac{4\pi N \sigma D}{1000} \tag{23}$$

where N is the Avogadro number, σ is the collision radius, approximated to mean complex radius, D is $D_M + D_{O_2}$, where D_M and D_{O_2} are the diffusion coefficients of luminophore and oxygen, respectively, approximated to D_{O_2}. Stern-Volmer equation becomes

$$\frac{I^0}{I} = \frac{\tau_0}{\tau} = 1 + \alpha \cdot \frac{4\pi \cdot N \cdot \sigma \cdot p_{tot}}{10^5} \cdot \tau_0 \cdot D_{O_2} \cdot \sigma_{O_2} \cdot \%O_2 = 1 + K'_{SV} \cdot \%O_2 \tag{24}$$

We may explicit K'_{SV} constant:

$$K'_{SV} = \alpha \cdot \frac{4\pi \cdot N \cdot \sigma \cdot p_{tot}}{10^5} \cdot \tau_0 \cdot D_{O_2} \cdot \sigma_{O_2} \tag{25}$$

We can tune K'_{SV} by changing luminophore (and therefore τ_0), or polymeric matrix, influencing D_{O_2} and σ_{O_2}.

$$K'_{SV} \propto \tau_0 \cdot D_{O_2} \cdot \sigma_{O_2} \tag{26}$$

2.4 ELLIPSOMETRY.

Ellipsometry[40,41] is a very sensitive measurement technique that uses polarized light to characterize thin films, surfaces, and material microstructure. It derives its sensitivity from the determination of the relative phase change in a beam of reflected polarized light. This results in a better sensitivity with respect to intensity reflectance measurements. Also, ellipsometry is more accurate than intensity reflectance because the absolute intensity of the reflected light does not have to be measured, thus no special reference samples need to be maintained.

Ellipsometry measures the change in polarization state of light reflected from (or transmitted through) the surface of a sample. Fundamentally, ellipsometry refers only to the measurement of the polarization state of a light beam. However, ellipsometric measurements are usually performed in order to describe an "optical system" that modifies the polarization state of a light beam. For thin film sample analysis, the "optical system" is the thin layer sample itself. The measured values are expressed as psi (Ψ) and delta (Δ). These values are related to the ratio of Fresnel reflection coefficients r_p and r_s for p- and s polarized light, respectively.

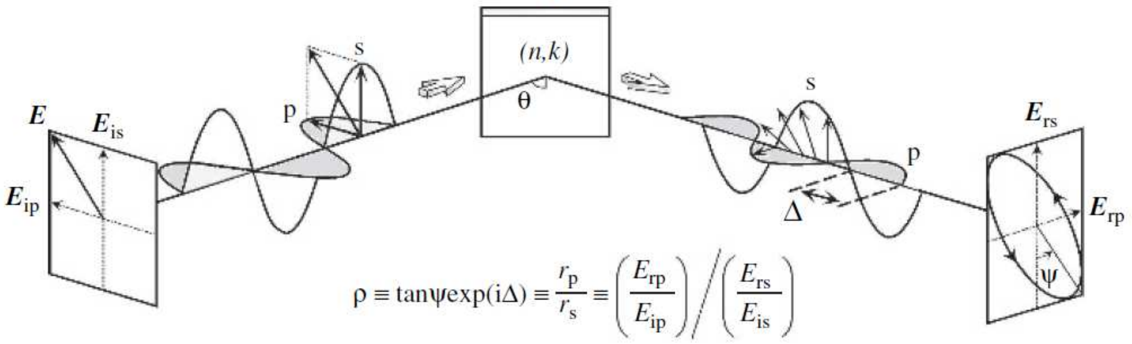

Figure 5. *Ellipsometry: instrumental scheme and fundamental parameters*

As ellipsometry measures the ratio of two values it can be highly accurate and very reproducible. Because the ratio is a complex number, it also contains "phase" information (Δ), which makes the measurement very sensitive.

Ellipsometry is commonly used to characterize both thin films and bulk materials. The most common application is measurement of thin film thickness and its optical constants. For many samples, ellipsometry is sensitive to film thickness on a sub-monolayer level. It has also proven to be the primary technique for determining optical constants in the UV, visible, and IR wavelength ranges. Ellipsometry is very flexible and is sensitive to many microstructural material properties. It may be used to determine:

- Optical constants (n,k)
- Thin film thickness (single or multiple layers)
- Doping concentration
- Surface and interfacial roughness
- Alloy ratio
- Crystallinity
- Optical anisotropy
- Depth profile of material properties

Spectroscopic ellipsometry is an extremely powerful measurement technique. It has many advantages over similar optical characterization tools (e.g. reflectometry, single-wavelength ellipsometry): it is non-destructive, fast and does not require preparation of the sample.

Ellipsometry works best for film characterization when the film thickness is not too much smaller or larger than the wavelength of the light used for the measurement. It is relatively difficult to use a probe of 500 nm wavelength to characterize a 0.5 nm or 10000 nm thick film, whereas films from about 5 nm to 1000 nm are much simpler to characterize with this wavelength. In general, an infrared ellipsometer is better for thick films (100 nm – 50 microns), while visible and ultra-violet wavelengths are better for thinner films (1Å – 1 microns).

Also, roughness features on the sample surface or at film interfaces should be less than ~ 10% of the probe beam wavelength for the ellipsometric analysis to be valid. Larger features may cause non-specular scattering of the incident beam and depolarization of the reflected beam. Again, the preferred wavelength range depends on the application. Mirror-like surfaces are typically measured with ultraviolet and visible ellipsometry; however, industrial-rolled aluminum surfaces have been measured with the longer wavelengths of an IR ellipsometer. Finally, the uniformity of a film within the measured spot is a critical factor. Good measurements are obtained with film thickness varying less than 10% in the sample surface spot width. In other words the two film surfaces have to be parallel within that approximation.

All optical experiments follow the same general procedure as outlined in this section. Optical experiments never directly measure the sample parameters of interest (thicknesses, optical constants, etc.); rather they measure some quantity that is a function of the parameters of interest. They are therefore obtained by comparing the results of simulations coming from the physical model adopted (containing the relevant parameters) to the experimental data. This procedure may be divided into the following four steps, illustrated in **Figure 6**.

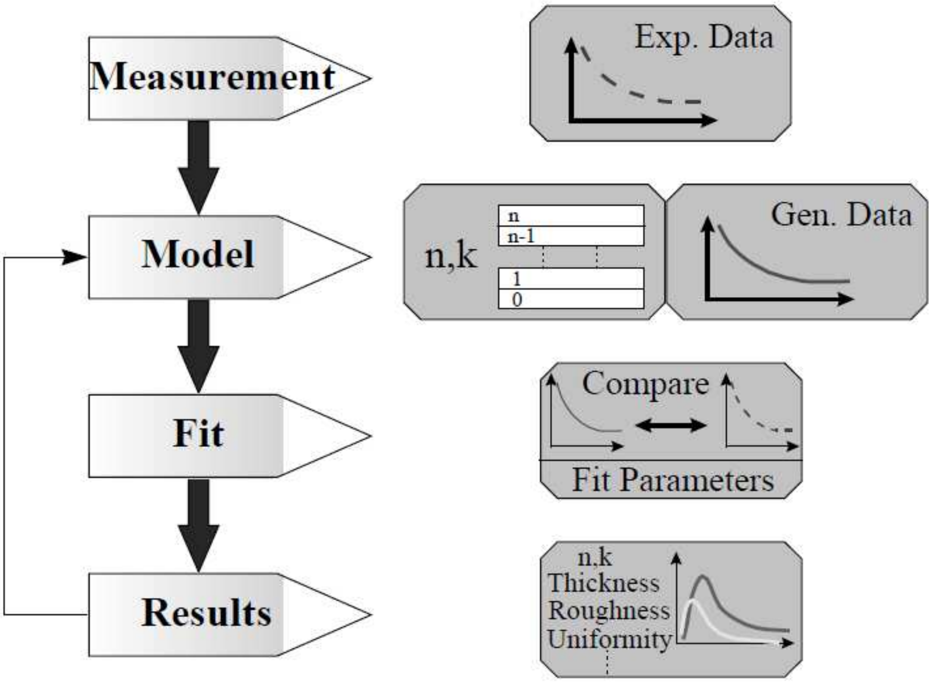

***Figure 6**. Basic procedure used in ellipsometry measurements to determine material properties from experimental data*

3. REAGENTS, INSTRUMENTATION AND METHODS

3.1 REAGENTS

Platinum (II) chloride, 5,10,15,20-tetraphenyl-porphyrin, benzonitrile, ruthenium (III) chloride trihydrate (99.98%), 4,7-diphenyl-l,l0-phenanthroline (dpp). Sodium octylsulphate (Na-OS), sodium chloride (NaCl), ethylene glycol, Tetrahydrofuran (THF), chloroform ($CHCl_3$) *anhydrous* ≥99%, polisulfone (PSF), MN:16.000, MW:35000, poly(vinyl chloride) high molecular weight (PVC), 5,10,15,20-Tetrakis(pentafluorophenyl)-21*H*,23*H*-porphyrin palladium(II) (PdTFPP) and palladium(II) (PdTFPP), 2,3,7,8,12,13,17,18-Octaethyl-21*H*,23*H*-porphine Palladium(II) (PdOEP) were obtained from Aldrich Products. 5,10,15,20-Tetrakis(pentafluorophenyl)-21*H*,23*H*-porphine Platinum(II) (PtTFPP) was obrained from Frnotier Scientific. Ultrapure water was obtained with a Millipore Plus System (Milan, Italy, resistivity 18.2 MΩ cm^{-1}). Ru(dpp)OS and PtTPP were synthesized according to references [42] and [43], respectively.

3.2 INSTRUMENTS

A Perkin-Elmer lambda 25 UV-Vis spectrophotometer was used to determine the absorbance spectra of the luminophores incorporated in the membranes. Measurements on membranes were done by inserting a membrane holder in a slit perpendicular to the incident beam. Emission spectra were recorded with a Andor Newton CCD cooled by a Peltier cooler at -70°C chamber coupled to a Shamrock 3031-B grating. Measurements were recorded using a gain of 4x, 128 electron multiplier 128x, slit 10 µm and averaging 100 acquisitions. Background and calibration using a Ar/Hg lamp occurred once a day. Thicknesses measurements were done with a spectroscopic ellipsometer mod. Alpha-SE™ (J.A. Woollam Co. Inc.).

3.3 LUMINOPHORES SINTHESYS AND CHARACTERIZATION

3.3.1 Sinthesys of Ru(dpp)OS[42]

Ruthenium trichloride trihydrate (225.9 mg) was dissolved in a mixture of 5 mL of ethylene glycol and 0.5 mL of water at 120 °C. Then, 862.6 mg of dpp were added. The mixture was heated to 165 °C under reflux for 45 min. After cooling, the solution was dissolved in 50 mL of acetone, filtered, and diluted with 50 ml of acetone. A total of 100 mL of a 10 mM aqueous solution of Na- OS was added to the filtrate. Finally, 100 mL of 1 M sodium chloride solution was added. The orange precipitate was filtered and washed four times with distilled water. Further purification was accomplished by recrystallization from acetone. The dye was obtained as an orange powder in 75% yield.

3.3.2 Sinthesys of PtTPP[43]

5,10,15,20-Tetraphenyl porphyrin (0.75 mmol) and platinum (II) chloride were dissolved in 20 ml of refluxing benzonitrile under nitrogen. After 24 hours the solvent was evaporated under vacuum and the product was purified by recrystallization from chloroform. The dye was obtained as a red powder in 85% yield

3.4 LUMINOPHORES ABSORPTION AND EMISSION SPECTRA

Ruthenium phenanthrolines and metal-porphyrins[44] are commonly used for optical oxygen sensing because of their long lifetimes and strong absorption in the blue-violet region of the spectrum, which is compatible with common high-brightness LEDs. Each luminophore has both advantages and disadvantages: phenanthrolines show great luminescence quantum yield and may be easily embedded in very different matrices[45-49] Porphyrins show generally great sensitivity because of their longer life-time.[50] Luminophores having a lot of CH bonds are more labile and usually undergo photo-bleaching effects,[51] consequently, highly fluorinated compounds are usually preferable[52,53].

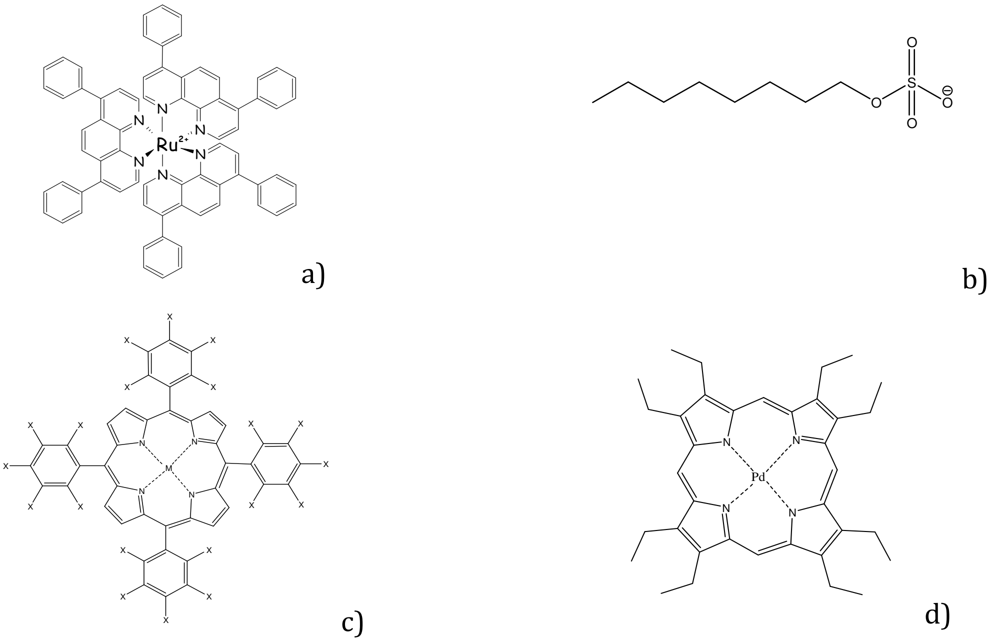

a)

b)

c)

d)

Figure 7. *a)Ru(dpp)$_3^{2+}$, b) octylsulphate (OS) c)PtTPP (M=Pt, X=H), PtTFPP (M=Pt, X=F), PdTFPP (M=Pd, X=F), d)PdOEP*

The luminophores employed in this thesis, shown in **Figure 7** are: ruthenium tris-(4,7-diphenyl-1,10-phenanthroline) bis(octylsulphate) (Ru(dpp)OS), 5,10,15,20-Tetrakisphenyl-21*H*,23*H*-porphine platinum(II) (PtTPP), platinum 5,10,15,20-Tetrakis(pentafluorophenyl)-21*H*,23*H*-porphine platinum(II) (PtTFPP), 5,10,15,20-Tetrakis(pentafluorophenyl)-21*H*,23*H*-porphine palladium(II) (PdTFPP), 2,3,7,8,12,13,17,18-Octaethyl-21*H*,23*H*-porphine palladium(II) (PdOEP).

Absorption and emission spectra of these luminophores have been already studied.[54,55] The Ru(dpp)OS embedded in a polymeric matrix shows (see **Figure 8**a) an absorption band at 451 nm with a half-height width of 109 nm in polysulfone (PSF), due to a metal-ligand charge transfer (MLCT) from a *d* orbital of the metal center to a antibonding ligand orbital ($t_{2g}(Ru) \rightarrow \pi^*(dpp)$). The emission peak at 608 nm can be attributed to the transition from the triplet excited state (^{3}MLCT) to the fundamental state. [54]

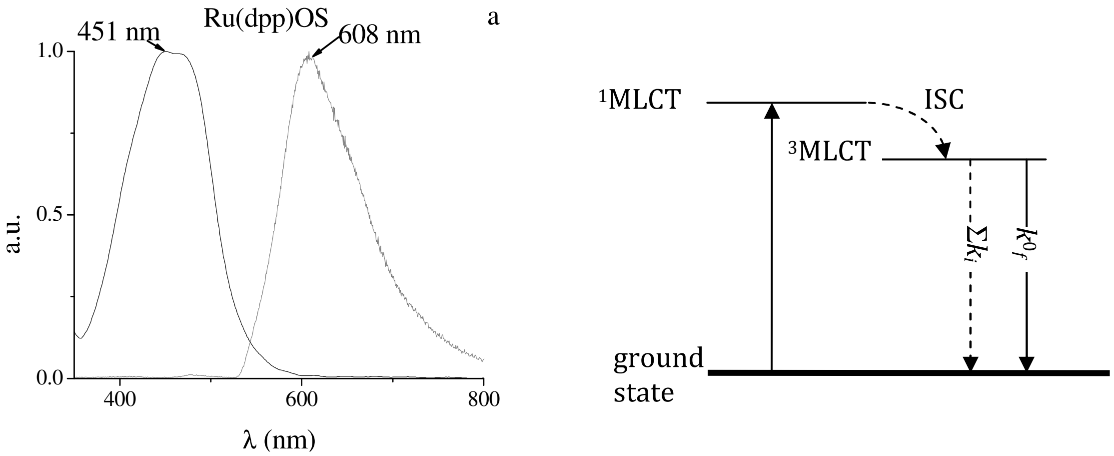

Figure 8. a)normalized absorption (black) and emission (grey) spectra of Ru(dpp)OS embedded in a PSF matrix b) Jablonski diagram for Ru(dpp)OS, showing ground state and excited states involved in transition in ***Figure 8*** *(a). ISC stay for inter system crossing*

In **Figure 8**b the Jablonski diagram for Ru(dpp)OS is shown. The luminophore in its ground state get excited to a singlet excited state ^{1}MLCT. Intersystem crossing (ISC) allows the transition to a triplet excited state ^{3}MLCT. The ^{3}MLCT is the excited state involved in radiative decay, non radiative decays and quenching reaction discussed in Equations 7, 8 and 9.

Porphyrin absorbance spectra can be explained by Gouterman's theory[55]. According to this theory, the absorption bands in porphyrin systems arise from transitions between two HOMOs and two LUMOs; the metal center and the substituents on the ring affect the relative energies of these transitions. The HOMOs were calculated to be an a_{1u} and an a_{2u} orbital, while the LUMOs were calculated to be a degenerate set of e_g orbitals. Transitions among these orbitals give rise to two excited states, both of ${}^1E_u$ character. Orbital mixing splits these two states in energy, creating a higher energy ${}^1E_u$ state with greater oscillator strength, giving rise to the Soret band (or B band, at about 400 nm) , and a lower energy ${}^1E_u$ state with less oscillator strength, giving rise to the Q-bands between 500 and 550 nm. Two vibronic Q bands may be distinguished: Q [0,0] represent the transition to the fundamental vibrational state of ${}^1e_g$, while Q [1,0] represent the transition to the first vibrational excited state of ${}^1e_g$.

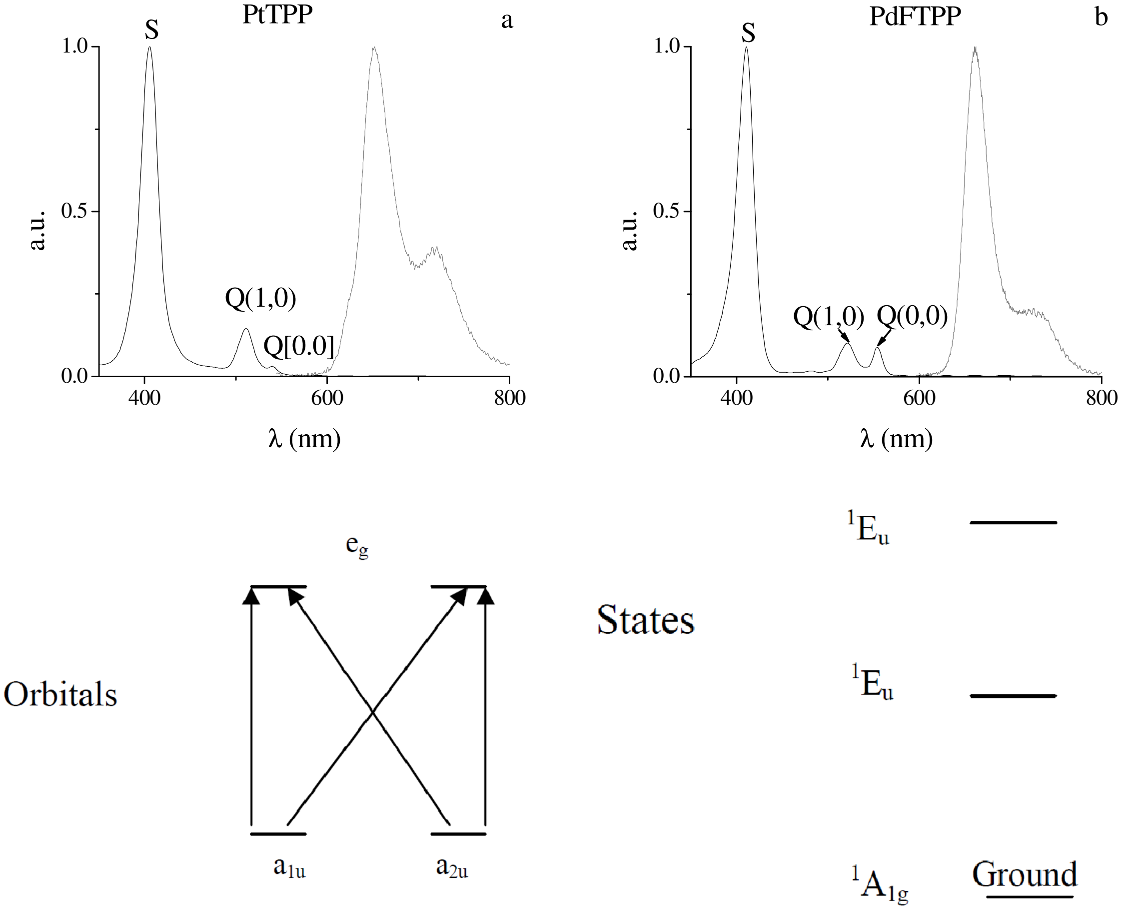

Figure 9. *a) PtTPP normalized absorption (black) and emission (grey) spectra. Absorption peaks: 405 nm (S band), 511 nm (Q[1,0] band) and 540 nm (Q[1,0] band); emission peaks 652 nm and 719 nm. b) PdTFPP normalized absorption (black) and emission (grey) spectra. Absorption peaks: 410 nm (S band), 521 nm (Q[1,0] band) and 554 nm (Q[1,0] band); emission peaks 661 nm and 719 nm c) Orbital diagrams showing possible transitions for porphyrins. Note that the HOMOs are shown to be degenerate, because porphyrins adopted are symmetrically substituted. Vertical lines represent O transition, diagonal ones represent S transition b) State diagrams showing possible excited states for porphyrins. Lower 1Eu orbital is involved in Q transition, higher one in S transition*

The absorption spectra of two metal porphyrin complexes, PtTPP and PdTFPP, embedded in PSF are shown in **Figure 9.** They exhibit the typical multiple band aspect: the main Soret's band, the Q(1,0) and Q(0,0) bands are visible.[53] PtTPP has an increase of 6 nm of the half-height width. The fluorinated MP has the largest $\varepsilon_{Q(1,0)} / \varepsilon_{Q(0,0)}$ ratio because of the effects of the substituents in the metal porphyrins on the π-π* transitions[56,57]. The $\nu_{[B-Q(0.0)]}$ split for PtTPP is 6148 cm^{-1}. The $\nu_{[B-Q(0.0)]}$ split for PdTFPP is 6310 cm^{-1}. Both porphyrins have a very similar emission profiles showing two bands: the most intense at about 650 nm, the other at about 720 nm. They are assigned to the triplet state of the Q bands.[58] The normalized emission profiles in the presence and in the absence of O$_2$ are coincident as expected by theory.

Table 1. *Lifetimes in absence of oxygen, absorption and emission wavelengths for Ru(dpp)OS, PtTPP, PtTFPP, PdTFPP and PdOEP in solution.*

complex	τ_0 (μs)	λ^{em}(nm)	λ^{ab}(nm)
Ru(dpp)OS[59]	6	608	452

complex		λ^{em}(nm)	$\lambda^{ab}_{B(0,0)}$ (nm)	$\lambda^{ab}_{Q(1,0)}$ (nm)	$\lambda^{ab}_{Q(0,0)}$ (nm)
PtTPP[53]	50	652	401	509	539
PtTFPP[60]	70	648	390	510	535
PdTFPP[61]	850	661	410	521	554
PdOEP[62,63]	990	670	392	512	546

3.5 POLYMERIC MATRIX CHOICE

The ideal polymeric matrix for oxygen sensor has the highest oxygen permeability, is impervious to interfering species and provides a suitable chemical and mechanical stability and minimizes luminophore leaching. Matrixes have also an influence over the sensor response sensibility (K'_{SV} in proportional to matrix permeability) and to the linearity of the Stern-Volmer plot.[64] Various thermoplastic soluble polymers provide the required features. Among them, polysulfone (PSF), whose fundamental unit is reported in **Figure 10**, is very promising, because of its high mechanical and chemical stability, in particular in oxidant environments. PSF has a high thermal stability up to 165°C, which made it a promising material for commercial sensor. Its glass temperature transition is 185°C. PSF is compatible to standard thermal sterilization procedures, making it suitable for biological or alimentary industrial applications, where sterilization is mandatory. Moreover, PSF-based sensors exhibit linear Stern-Volmer plots, short response time and high sensitivity.[28]

PVC-based sensors have been tested too. They exhibit linear Stern-Volmer plots and short response time but their sensitivity is about one tenth of the PSF-based ones

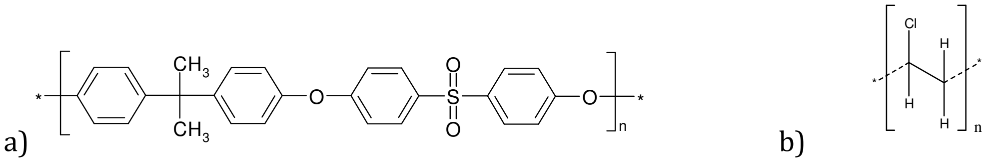

***Figure 10.** a) Polysulfone (PSF) b) Polyvinyl chloride (PVC)*

3.5.1 Membrane preparation: dip-coating

The substrates were previously washed with water and soap, rinsed with water, with isopropanol and then dried under nitrogen flow. The membranes were obtained from a solution of the metal complex and polymer in 10 g of dry solvent. The dip-coating was carried under nitrogen athmosphere The optimized conditions[65] for the dip-coating deposition are reported in **Table1**.

After chloroform had evaporated, membranes were dried at room temperature for 1 h and the film deposited on the back substrate side is removed with acetone. The membrane thickness was determined by ellipsometric measurement.

***Table1.** Dip coated membrane preparation parameters*

Label	*Ru(dpp)OS*	*Porphyrins*	*Ru(dpp)OS*	*Porphyrins*
Concentration (μ mol g^{-1} (PSF))	20	10	20	10
Polymer	PSF	PSF	PVC	PVC
Solvent	$CHCl_3$	$CHCl_3$	THF	THF
Polymer concentration (g mL^{-1} (solvent))	0.2	0.2	0.1	0.1
Immersion velocity (cm min^{-1})	12	12	12	12
Extraction velocity (cm min^{-1})	2.5	1.5	1.5	1.0

3.5.2 Membrane preparation: spin coating

The substrates were previously washed with water and soap, rinsed with water, with isopropanol and then dried under nitrogen flow. The membranes were obtained from a solution of the metal complex and polymer in 10 g of dry solvent. The optimized conditions for the spin-coating deposition are reported in **Table 2**.

After chloroform had evaporated, membranes were dried at room temperature for 1 h. The membrane thickness was determined by ellipsometric measurement.

Table 2. *Spin coated membrane preparation parameters*

Label	***Ru(dpp)OS***	***Porphyrins***
Concentration (μ mol g^{-1} (PSF))	20	10
Polymer	PSF	PSF
Solvent	$CHCl_3$	$CHCl_3$
Polymer concentration (g mL^{-1} (solvent))	0.067	0.067
spin rate (Hz)	35	35
Support	Glass	Glass

3.6 MEMBRANE CHARACTERIZATION

Various sets of membranes have been deposited on microscope glass substrates. The membrane thickness has been determined via ellipsometry. Membranes may be represented with a three layer model:

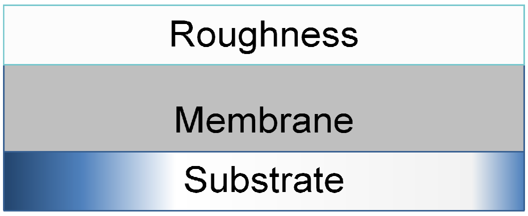

1. Substrate: glass substrate (previously characterized)
2. Polymeric membrane: data are collected in the range 400-1000 nm, but fit are performed only on the data between 550 and 900 nm, where there is no light absorption by the luminophore. Under the verified condition of transparency the Cauchy model was used to modeling the system:

$$n(\lambda)=A+\frac{B}{\lambda^{2}}+\frac{C}{\lambda^{4}} \qquad\qquad k(\lambda)=0 \qquad (27)$$

Thickness non uniformity has to be accounted for as it is often larger than 10% of the total membrane thickness.

3. Superficial roughness: considered as a mixing layer containing 50% air and 50% polymer

The match between fitted and experimental data, reported in Figure 2, is very good in the analysis range whilst there is a lack of fitting in the light absorbing zone, as expected.

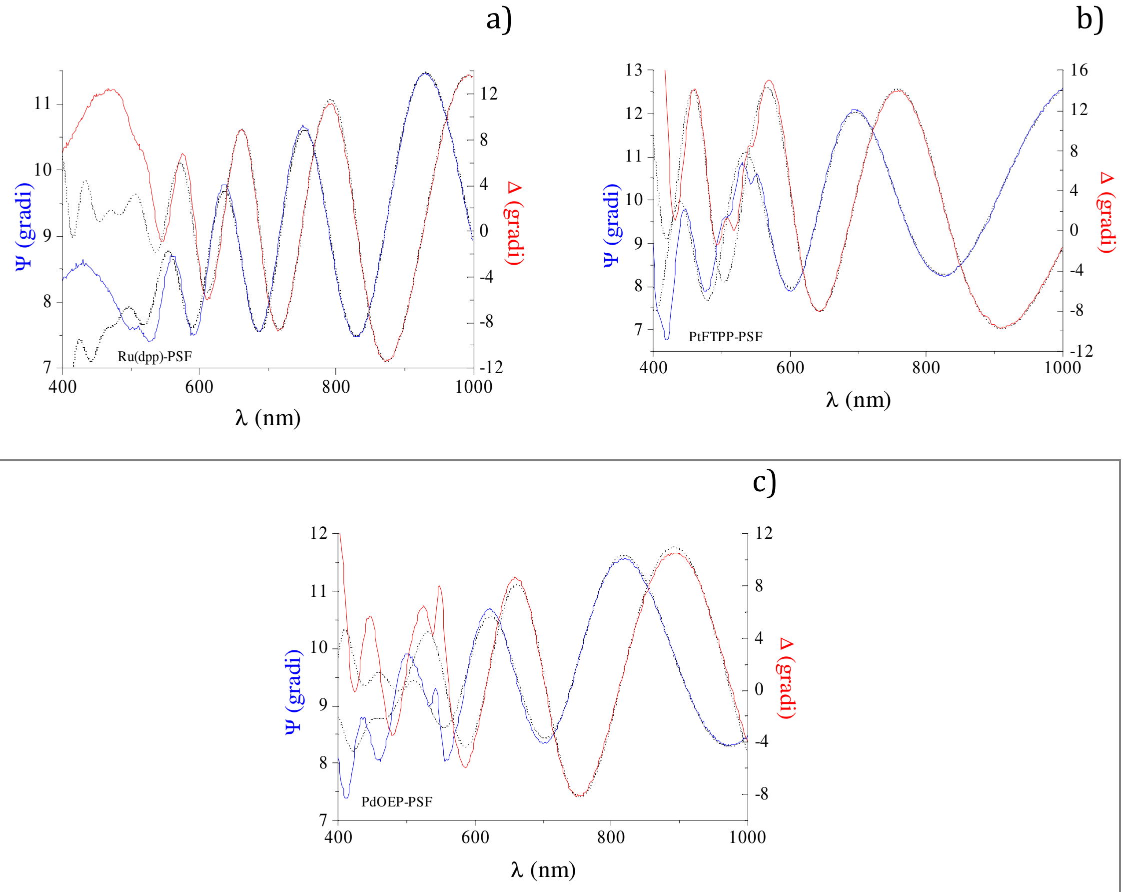

Figure 11. *Ellipsometric analysis: experimental (continuous lines) and simulated (dotted lines) data for the set A membranes a)Ru(dpp)OS-PSF, b)PtTFPP-PSF, c)PdOEP-PSF*

Ellipsometric analysis results are averages of four repeated measurements on each membrane. Mean thickness, $\overline{L}$, for all the membranes deposited are reported in **Table 3**.

Table 3. *Membrane thickness for all the membranes deposited*

Thickness (µm)	***A****(spin coat)*	***B****(dip coat)*	***C****(dip coat)*
Ru(dpp)OS-PSF	1.335 (0.067)	1.75(0.30)	2.37(0.41)
PtTPP-PSF		2.53(0.30)	2.28(0.38)
PtTPP-PVC			2.63(0.35
PtTFPP-PSF	756(0.019)		
PdTFPP-PSF		2.80(0.14)	
PdTFPP-PVC			2.71(0.28)
PdOEP-PSF	843(0.080)		

3.7 INSTRUMENTAL SETUP

The optical oxygen sensor core consists, as evidenced above, in a metal-organic complex embedded in a polymeric matrix. As shown in **Figure 12**, a LED light source irradiates the membrane. Light emitted, filtered by a suitable optical filter to cut residual LED light, is collected by a photodiode.

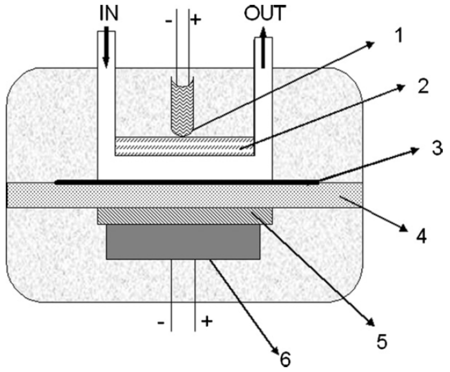

Figure 12. *Schematic representation of the oxygen optical sensor: (1) excitation LED; (2) blue photographic filter;(3) sensitive membrane deposited on glass support; (4)glass optical window; (5) orange photographic filter; (6)photodiode*

In the oxygen sensor built for this thesis, the excitation source is a Bivar, LED5UV40030 high-brightness violet LED (angle 30°, spectral output peaks at 406 nm) or a high-brightness blue LED (Nichia, NSPE590, angle 15°) whose spectral output peaks at 464 nm, or a blue violet laser diode (SHARP, GH04P21A2GE 105mW, max emission 405 nm, half intensity width 2 nm). If a laser source is employed, source heating is prevented by pulsing the laser emission and by sampling emissions at the end of the pulse period, when the signal reached a steady-state condition. The pulse time width and the rest time were 3 ms and 0.5

s long, respectively. The sampling time was made in the last 10% of the pulse width. Responses were average of 1000 pulses.

Light emitted from the membrane passed through a Kodak n°21 Wratten gelatin long-wave-pass filter (cutoff 580 nm,) and focused onto a Hammamatsu S1223 photodiode detector (Hamamatsu, Middlesex, U.K.). The signal output was directed to a LeCroy Wave Surfer® 44xs, 450 MHz, oscilloscope (Geneva, Switzerland). Life-times were determined from pulsed irradiation realized with a *Thurby Thandar Instruments* TGP110 pulse generator. Gas mixtures were prepared by mixing suitable amounts of nitrogen and oxygen. Oxygen and nitrogen were flown via Alicat Scientific mass flow controllers (code MC-100-SCC-D, calibrated for O_2 and N_2) into the sensor cell and mixed via a homemade mixer. Calibration of mass flow controllers was controlled with a *PBI Dansensor* O_2 analyzer (Milan, Italy) measuring the oxygen percentage after mixing.

3.7.1 Stern Volmer calibration

In **Figure 13**a is reported light intensity emitted from a PtTFPP-PSF membrane versus time, while it is in equilibrium with various oxygen/nitrogen mixtures. As expected, the membrane maximum intensity is reached in absence of oxygen, whilst it decreases with increasing oxygen concentration. Each step competes to an oxygen concentration, set by the mass flow controllers. For sensor calibrations, oxygen concentration range from 0% to 20% and measurement are repeated at least three times. Data are sampled when intensity has reached a steady value. In **Figure 13**b is shown Stern-Volmer plot relative to data in Figure 13a. Linear regression slope is K'_{SV} . It must be noted that data relative to different calibrations are superimposed, indicating that the sensor gives repeatable measurements.

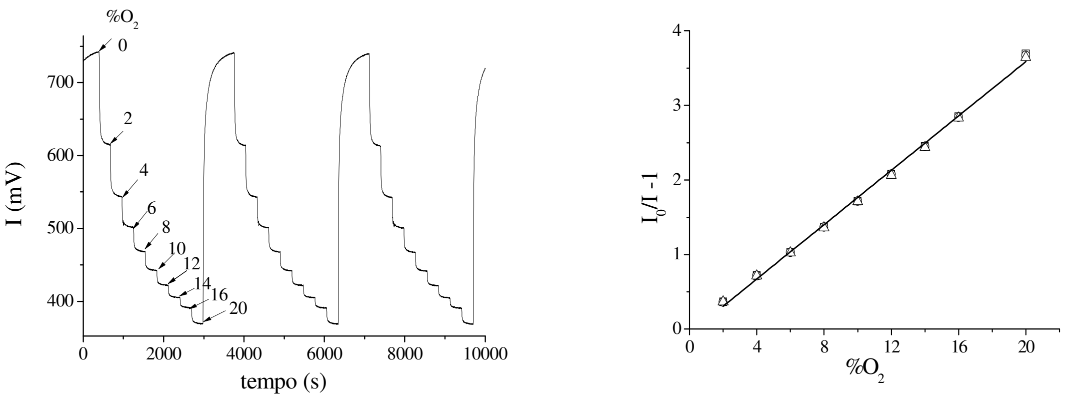

Figure 13. *a)Light emission profiles for set B PtTFPP-PSF membrane during a Stern-Volmer calibration. Each step refers to a %O_2, shown in figure. Tree calibrations, recorded at 90°C, are reported. b) Stern-Volmer plot of data in Figure (a)* $K'_{SV}=0.182(0.003)$

4 THEORETICAL AND EXPERIMENTAL SECTION

4.1 INFLUENCE OF THE REAL BACKGROUND SIGNAL ON THE LINEARITY OF THE STERN-VOLMER CALIBRATION

One of the aspects not yet completely understood of oxygen sensor behaviour is the non-linearity of the SV calibration experimentally encountered in many cases.[66-68] Some authors explained this behaviour with a multisite emitting model, either 2 and 3 sites models[69] or with log Gaussian models.[70] Moreover, non-uniform decays were treated with various fitting procedures[64,71] but they cannot correctly distinguish a single Gaussian lifetimes distribution and a sum of two exponentials or a bimodal Gaussian distribution and a sum of at least three exponentials.[64,72,73] Thus, a description based on discrete lifetime components should only be regarded as truly representing discrete molecular states if supported by supplementary data. A simpler model for describing the non-exponential luminescence decay was developed by Draxler et. al.,[64] who considered the interaction of the luminophore with the non-uniform environment provided by the hosting polymer. Also in this case, however, some deviations from linearity remained unexplained.

In this chapter an explanation of this behaviour is proposed,[74] at least for some experimental cases, on the basis of a more complete rationalization of the nature of the optical response. The role of the background correction in the curvature of the SV and also in the discrepancy often encountered between calibrations with I and τ[75] will be demonstrated. Moreover, it will be demonstrated that the common practice to make a simple background correction by testing the membrane without the lumunophore is a mistake because this choice does not account for some processes like self absorption of the label, and the presence of unquenchable emitted light. These events may produce unexpected experimental inconsistencies leading to the cited inequality between the light intensity and with the life-time ratios, $\frac{I_0}{I} \neq \frac{\tau_0}{\tau}$. Theoretical considerations will furnish the mathematical models to explain experimental data obtained with three test polysulfone-based membranes.

4.1.1 *Experimental section*

4.1.1.1 *Preparation of Oxygen-Sensitive Membranes.*

The polysulfone membranes investigated are set B membranes and were prepared by dip-coating onto a glass support (10x30x1 mm) under nitrogen atmosphere as detailed in Chapter 3.5.1. Membrane thickness is reported in **Table 3**, Chapter 3.6

4.1.1.2 Instrumentation

The oxygen sensor employed is described in Chapter 3.7

4.1.2 Theoretical section

4.1.2.1 Nature of the experimental light emission in an optical sensor

The SV equation works with the light intensity, I, coming from the kinetic scheme presented in Chapter 2.3.1:

$$M + h\nu \xrightarrow{k_{abs}} M^* \tag{6}$$

$$M^* \xrightarrow{k_f^0} M + h\nu' \tag{7}$$

$$M^* \xrightarrow{\sum k_i} M + heat \tag{8}$$

$$M^* + Q \xrightarrow{k_q} M + Q^* \tag{9}$$

The question is: does the detector read the emitted light required by the mechanism above? The general answer is, no. The recorded light depends also on the membrane nature and on the instrumental setup. The experimental emitted light read by the photodiode at the ith experiment may be therefore defined as

$$I_i^{ex} = a_i \cdot \left(I + I^{NQ}\right) + I_i^B - I^{Abs} \tag{28}$$

in the presence of oxygen and

$$I_{0,i}^{ex} = a_i \cdot \left(I_0 + I^{NQ}\right) + I_i^B - I^{Abs} \tag{29}$$

in the absence of oxygen with $0 < a < 1$ depending on the system geometry. I_i^{NQ} is the non-quenchable light coming from the luminophore; I_i^B is the background light emission and I_i^{Abs} is the light absorbed by the luminophore inside the membrane. I_i^B, in turn, is composed by two contributions: one is the photodiode background current, I_i^{PTD}, and the other is the non filterable light coming from the light source, I_i^{NF}.

$$I_i^B = I_i^{NF} + I_i^{PTD} \tag{30}$$

The constant a_i may be eliminated by normalizing the light intensity and obtaining the corrected SV equation.

$$\frac{I_{0,i}^{ex} - I_i^B + I^{Abs} - a_i \cdot I^{NQ}}{I_i^{ex} - I_i^B + I^{Abs} - a_i \cdot I^{NQ}} = \frac{I_0}{I} = 1 + K_{SV}^{'} \cdot \%O_2 \tag{31}$$

By rearranging Equation 31 we obtain a new form of the SV equation that accounts for the real background of the membrane:

$$I_i^{ex} = \frac{1}{K_{SV}^{'}} \cdot \frac{\Delta I_i^{ex}}{\%_{O_2}} + I_i^S + I_i^B = \frac{1}{K_{SV}^{'}} \cdot \frac{\Delta I_i^{ex}}{\%_{O_2}} + I_i^T \tag{32}$$

where $\Delta I_i^{ex} = I_{0,i}^{ex} - I_i^{ex} = a_i \cdot (I_0 - I) = a_i \cdot \Delta I$, $I_i^S = a_i \cdot I^{NQ} - I^{Abs}$ and $I_i^T = I_i^S + I_i^B$. If a_i is constant I^S and I^B do not depend on "i" and we may plot $I_i^{ex} - I^B$ vs. $\frac{\Delta I_i^{ex}}{\%_{O_2}}$ so that $\frac{1}{K_{SV}^{'}}$ and I^S may be obtained as slope and intercept, respectively. Equation 32 is a new form of the SV equation. It has the advantage to obtain the $K_{SV}^{'}$ and the effective background with a simple un-weighed regression method. On the contrary, the "classical" SV requires the knowledge of the background and a weighed regression. It is important to notice that if the experimental data are linear according to Equation 32 then there is no need of multisite hypotheses or other correction procedures. The correctness of the SV kinetic model is confirmed. To our knowledge, all authors neglect the I^S contribution and plot $\frac{I_0^{ex} - I^B}{I^{ex} - I^B}$ vs. $\%O_2$. The error made by neglecting I^S may be defined as

$$\%x_s = 100 \cdot I^S / \left(I_0^{ex} - I^B\right) \tag{33}$$

Consequently from Equation 31 we obtain

$$\frac{I_0}{I} = \frac{I_0^{ex} - I^B}{I^{ex} - I^B} = \frac{1 + K_{SV}^{'} \cdot \%O_2}{1 + x_S \cdot K_{SV}^{'} \cdot \%O_2} \tag{34}$$

Figure 14 reports Equation 34 with nine x_S values for $K_{SV}^{'} = 0.14$ (PtTPP membrane).

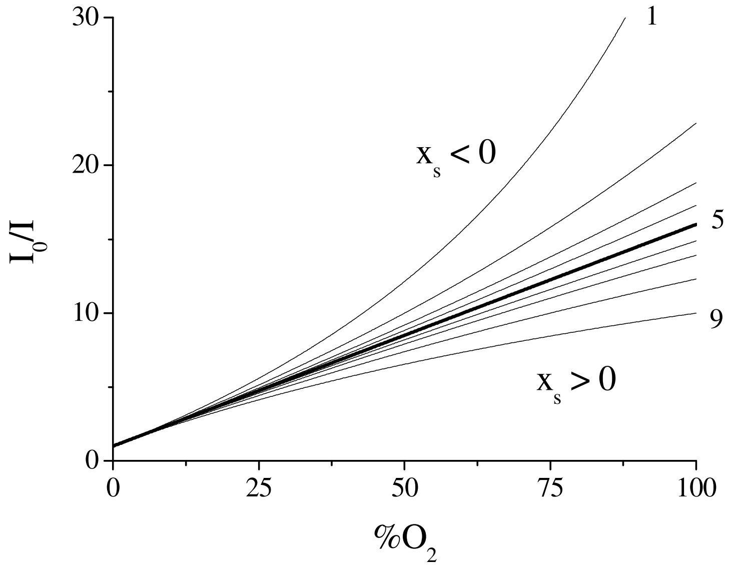

Figure 14. *Plot of Equation 34 with $K_{SV}^{'} = 0.14$ (PtTPP membrane) with $\%x_S$ = -4, -2, -1, -0.5, 0.0, 0.5, 1, 2, 4 (curves 1 to 9, respectively)*

For $x_S < 0$ and $x_S > 0$ Equation 34 produces positive (curves 1-4) and negative (curves 6-9) deviations from linearity, respectively. These deviations are more accentuated for larger $K_{SV}^{'}$ and $\%O_2$ values. Curve 5 is linear as $x_S = 0$. These results demonstrate that if the I^S value is not considered when really present, the SV is not linear. In particular, with the chosen $K_{SV}^{'}$ an error $\%x_S$ of ± 0.5% is sufficient to observe curved calibrations that is, a curvature is significant for $\left| x_S \cdot K_{SV}^{'} \right| > 7 \cdot 10^{-4}$.

4.1.2.2 Statistical aspects of the fitting procedures for Equation 32

As $\frac{\Delta I_i^{ex}}{\%O_2}$ is not a deterministic variable, the standard approach to the regression procedure is not valid as ΔI_i^{ex} is not error free. Anyway, from the errors propagation theory we may demonstrate that the variance of the ordinates, $s^2_{I_i^{ex}-I^B}$, is larger than that of abscissas, $s^2_{\left(\frac{\Delta I_i^{ex}}{\%O_2}\right)}$, for $\%O_2 > 1$ so that we may consider the least squares regression a good approximation for $\%O_2 > 1$. A safer approach, especially for sensors dedicated to low concentrations ($\%O_2 < 1$), may be obtained with the robust non-parametric regression.[76]

4.1.2.3 *Statistical aspects of the fitting procedures for Equation 31*

The SV model corrected for I^S is a composed measurement accounting for $\frac{I_0^{ex} - I^B - I^S}{I^{ex} - I^B - I^S} - 1$, and its error, $s_{R_I} = s_{\left(\frac{I_0^{ex} - I^B - I^S}{I^{ex} - I^B - I^S} - 1\right)}$, must be estimated from the errors propagation assuming $s = s_{I_0} = s_I = s_{I^B} = s_{I^S}$.

$$s_{R_I} = \frac{\sqrt{2} \cdot s}{I - I^B - I^S} \cdot \sqrt{1 + \left(\frac{I_0 - I^B - I^S}{I - I^B - I^S}\right)^2} = \frac{\sqrt{2} \cdot s}{I_0 - I^B - I^S} \cdot \left(1 + K_{SV}^{'} \cdot \%O_2\right) \cdot \sqrt{1 + \left(K_{SV}^{'} \cdot \%O_2\right)^2} \quad (35)$$

This equation clearly indicates that more precise measurements are obtained with low $K_{SV}^{'} \cdot \%O_2$ values. When the calibration sensitivity is sufficiently low ($K_{SV}^{'} \cdot \%O_2 < 1$) precision becomes independent of $\%O_2$ and the regression may be not weighed. For a given membrane (that is for a given $K_{SV}^{'}$) Equation 35 indicates that the s_{R_I} increases with $\%O_2$, so that the regression must be weighed with.[77]

$$w_i = \frac{1}{s^2_{R_I}} \quad (36)$$

The model becomes:

$$R_I = P_{1w} + P_{2w} \cdot \%O_2 \quad (37)$$

where P_{1w} and P_{2w} are intercept and slope of the weighed model,[78] respectively. The SV model is correct only if the P_{1w} value is statistically equal to zero.

4.1.2.4 *Working interval of the classic SV equation*

As the response, *I*, is not linear with $\%O_2$, the sensitivity, $dI/d\%O_2$, decreases with $\%O_2$ so that at large $\%O_2$, measurements are less accurate, consequently, at what $\%O_2$ variation, $\Delta\%O_2$, produces a significant ΔI^{ex} value? The condition for which ΔI^{ex} is no more significant may be obtained with a T-test:

$$\frac{\Delta I^{ex}}{s_{y/x} \cdot \sqrt{2/n}} = t_{\alpha,n-2} \tag{38}$$

where $s^2_{y/x}$ is the estimate of the regression variance relative to Equation 32 with n data and $t_{\alpha,n-2}$ is the t-Student with $\alpha = 0.5$ and *n*-2 degrees of freedom. In this equation we used $s_{y/x}$ as estimate of σ_I. The ΔI^{ex} value may be computed from the derivative of the SV equation:

$$\Delta I^{ex} = \frac{I_0 \cdot K'_{SV} \cdot \Delta\%O_2}{\left(1 + K'_{SV} \cdot \%O_2\right)^2} \tag{39}$$

If $\Delta\%O_2$ is the required resolution value, R, combining Equations (38) and (39) we obtain the maximum $\%O_2$ for that resolution.

$$\%O_2^{\max} = \frac{1}{K'_{SV}} \cdot \left(g \cdot \sqrt{K'_{SV} \cdot R} - 1\right) + R \tag{40}$$

with $g = \sqrt{\dfrac{I_0}{t_{\alpha,n-2} \cdot \sqrt{2/n} \cdot s_{y/x}}}$. The plot $\%O_2^{\max}$ vs. K'_{SV}, parametric in *R*, is reported in **Figure 15**.

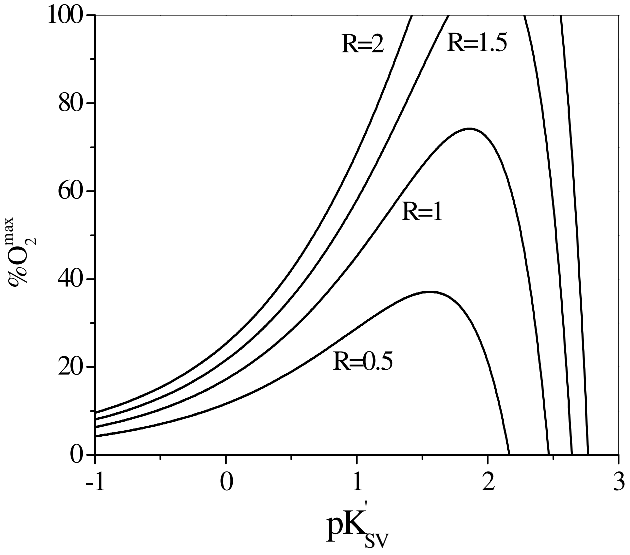

Figure 15. *$\%O_2^{max}$ vs. pK'_{SV}. Upper oxygen concentration limit, $\%O_2^{max}$, detectable with the SV for a resolution, $R = \Delta\%O_2 = 0.5, 1.0, 1.5$ and 2.0, with g = 17.3 (see Equation (40))*

All the membranes have very similar *"g"* values, *g* = 17.3 (1.3). For pK'_{SV} = -0.3, 0.9 and 1.75, close to those of our membranes (PdTFPP, PtTPP and Ru(dpp)OS embedded in PSF), the $\%O_2^{max}$ is 19.0, 60.7 and 100, respectively, when the required resolution is *R*=2%. For better resolutions these values decrease (see data relative to *R*=0.5%, for instance).

4.1.2.5 Considerations on the life-time based SV

It is suitable to point out that the SV in terms of lifetime, τ, may be also obtained by correcting the exponential fitting with τ_i^S :

$$\frac{\tau_{0,i}^{ex} - \tau_i^S}{\tau_i^{ex} - \tau_i^S} = \frac{\tau_0}{\tau} = 1 + K'_{SV} \cdot \%_{O_2} \tag{41}$$

This originates the equivalent form to Equation 32:

$$\tau_i^{ex} = \frac{\Delta \tau_i^{ex}}{K'_{SV} \cdot \%_{O_2}} + \tau_i^S \tag{42}$$

In this equation, anyway, the correction term τ_i^S cannot be interpreted as lifetimes are not additive and this makes Equation (42) highly improbable. It is possible to obtain a life-time-based sensible model by considering the emission areas during the time decay after the switch off of the exciting light pulse. That emission profile may be interpreted as the sum of many mono-exponential decays hypothetically due to non quenchable sites (I^{NQ}), to background decay ($I^F - I^{ABS}$) depending on the electrical circuit time constant, τ_{circ}. This is represented by the following equation

$$I(t) = I \cdot e^{-k \cdot t} + \sum_i I_i \cdot e^{-k_i \cdot t} + I^{PTD} \tag{43}$$

The emission area may be obtained by integrating Equation (43):

$$A^{ex} = \int_0^\infty \left(I(t) - I^{PTD}\right) \cdot dt = \int_0^\infty I \cdot e^{-k \cdot t} \cdot dt + \int_0^\infty \sum_i I_i \cdot e^{-k_i \cdot t} \cdot dt \tag{44}$$

and then, for a generic $\%O_2$

$$A^{ex} = I \cdot \tau + \sum_i I_i \cdot \tau_i = I \cdot \tau + I^{NQ} \cdot \tau_0 + \left(I^F - I^{ABS}\right) \cdot \tau_{circ} = I \cdot \tau + A^F \tag{45}$$

In the absence of O_2

$$A_0^{ex} = I_0 \cdot \tau_0 + A^F \tag{46}$$

From Stern Volmer equation (Equation 21) discussed in Chapter 2.3.1

$$\frac{I_0}{I} = \frac{\tau_0}{\tau} = 1 + K_{SV}^{'} \cdot \%O_2 \tag{21}$$

we obtain:

$$\frac{A_0^{ex} - A^F}{A^{ex} - A^F} = \frac{I_0 \cdot \tau_0}{I \cdot \tau} = \left(1 + K_{SV,I}^{'} \cdot \%O_2\right) \cdot \left(1 + K_{SV,\tau}^{'} \cdot \%O_2\right) \tag{47}$$

and after few rearrangements we obtain:

$$A^{ex} = \frac{A_0^{ex} - A^F}{\left(1 + K_{SV,I}^{'} \cdot \%O_2\right) \cdot \left(1 + K_{SV,\tau}^{'} \cdot \%O_2\right)} + A^F \tag{48}$$

This is equivalent to Equation (32). It is possible to obtain $K_{SV,\tau}^{'}$ and A^F as fitting parameters and, by combining Equation (47) with Equation 32 we formulate the "true" SV equation in terms of life-time.

$$\frac{\tau_0}{\tau} = \frac{A_0^{ex} - A^F}{A^{ex} - A^F} \cdot \frac{I^{ex} - I^B - I^S}{I_0^{ex} - I^B - I^S} = 1 + K_{SV,\tau}^{'} \cdot \%O_2 \tag{49}$$

The term "true" indicates that, in this form, the SV furnishes the correct $\frac{\tau_0}{\tau}$ ratio. Many authors observed the discrepancy between the SV in terms of I and τ [59,79] while others observed no discrepancies at all.[80] In this section we indicated possible causes and in the next one these hypotheses will be experimentally demonstrated.

4.1.3 Experimental data

4.1.3.1 Role of the background for the correct interpretation of the SV equation

The usual oxygen calibration with the SV approach would lead to the plots of **Figure 16**a. Clear curvatures are evidenced for the two MP complexes. **Figure 16**b reports the experimental $I_i^{ex} - I^B$ vs. $\Delta I_i^{ex} / \%O_2$ of three sensors, according to Equation 32. All membranes have linear behaviour according to the corrected SV model. As reported in the theory section, both robust and parametric regression models furnish statistically equivalent estimates of I^S and $K_{SV}^{'}$ as demonstrated by slopes and intercept values reported in **Table 4**.

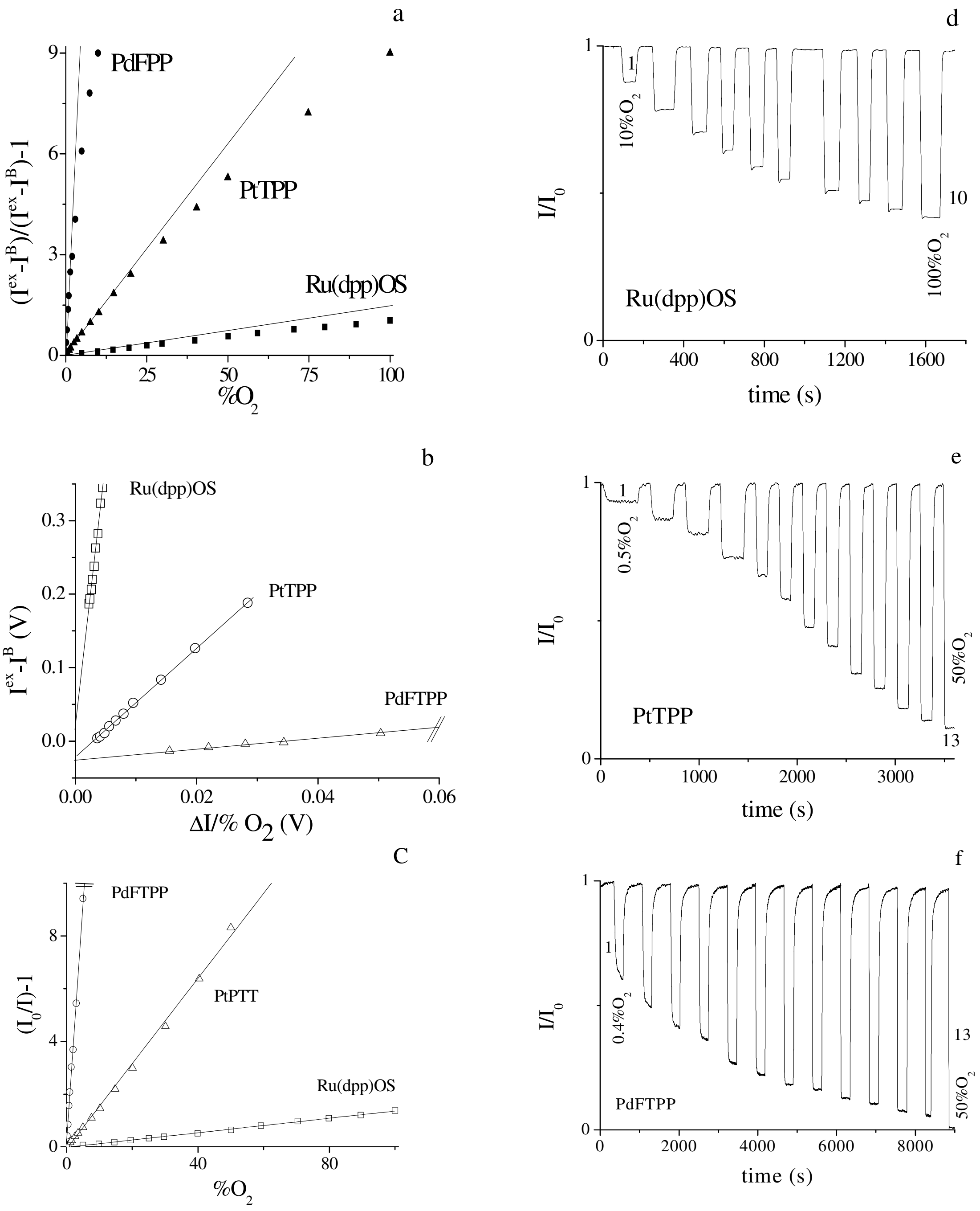

Figure 16. *(a) Usual representation of the SV plot with background subtraction. The straight lines represent the linear fitting of the first few data points for each membrane. (b) Experimental data plotted according to Equation 32 for Ru(dpp)OS (□), PtTPP (Δ) and PdTFPP(○) (parametric regression). The intercept represents an estimate of* I^S*. Regression parameters are in* ***Table 4****. (c) Experimental data plotted according to the SV model corrected with* I^S *(weighed parametric regression). Regression parameters are in* ***Table 5****.(d-f) Normalized emission profiles* $\%O_2$ *–100* $\%N_2$ *vs. time (profiles were corrected for background). (d) Ru(dpp)OS membrane;* $\%O_2$ *= 10, 20, 30, 40, 50, 60, 70, 80, 90, 100 (BLUE-LED). (e) PtTPP membrane:* $\%O_2$ *= 0.5, 1, 1.5, 2.5, 3.5, 5, 7.5, 10, 15, 20, 30, 40, 50* $\%O_2$ *(UV-LED). (f) PdTFPP membrane:* $\%O_2$ *= 0.4, 0.6, 0.8, 1, 1.5, 2, 2.5, 3, 4, 5.0, 7.5, 10, 50 (UV-LED)*

Table 4. *Parametric and non-parametric regressions relative to the three membranes reported in Figure 16b.*

Membrane	***Regression***	$I_0^{ex} - I^B$ ***(V)***	I^S ***(V)***	s_{I^S} ***(V)***	$1/K'_{SV}$	$s_{1/K'_{SV}}$	K'_{SV}	$\%x_s$	R^2
Ru(dpp)OS	Parametric	0.131	0.017	0.005	72.5	1.2	0.0138		0.9961
	Robust		0.014		73.0		0.0137	10.7	0.9991
PtTPP	Parametric	0.443	-0.0226	0.0095	7.47	0.07	0.134		0.9992
	Robust		-0.0223		7.47		0.134	-5.0	0.9992
PdTFPP	Parametric	0.480	-0.026	0.0012	0.536	0.006	1.87		0.9995
	Robust		-0.029		0.554		1.81	-5.9	0.9998

Table 5. *Parametric and weighed-parametric regressions (* $R_I = P_{1w} + P_{2w} \cdot \%O_2$*) relative to the three membranes reported in Figure 16c*

Label	***Regression***	P_{1w}	s_{P_1}	P_{2w}	$s_{K'_{SV}}$	R^2
Ru(dpp)OS	Parametric	0.013	0.019	0.0138	0.0003	0.997
	Weighed-parametric	0.0004	0.003	0.0137	0.0004	0.999
PtTPP	Parametric	-0.264	0.18	0.1437	0.0033	0.996
	Weighed-parametric	0.0087	0.025	0.1332	0.0024	0.997
PdFTPP	Parametric	0.012	0.02	1.77	0.025	0.995
	Weighed-parametric	0.001	0.020	1.82	0.012	0.999

A t-test made on the intercept indicates that I^S is statistically unequal to zero for all the considered membranes. PtTPP and PdTFPP membranes have $\%x_S = -5.0$ and $\%x_S = -5.9$ respectively. These negative values may be justified by the absorption spectra described in **Figure 9**. $\%x_S$ of PdTFPP is more negative than $\%x_S$ of PtTPP as expected by the $\varepsilon_{Q(0.0)}^{PdFTPP} / \varepsilon_{Q(0.0)}^{PtTPP} \cong 8$ ratio (PdTFPP absorbs more than PtTPP). On the contrary, the Ru(dpp)OS membrane has $\%x_S = +10.7$ which is much higher than blank. We interpreted this result with the presence of caged emitting sites not reachable by oxygen and therefore unquenchable. Both differences are significant and they change the SV calibration profile from linear to curved, as demonstrated in the theory section. The $\left|x_S \cdot K_{SV}^{'}\right|$ value of Ru(dpp)OS is 1.5·10^{-3} so that its calibration appears almost linear whilst the other two membranes have $\left|x_S \cdot K_{SV}^{'}\right|$ values largely greater than 7·10^{-4} (6.5·10^{-3} and 1.1·10^{-1} for PtTPP and PdTFPP, respectively) and justify the curvature experimentally found in **Figure 16**a.

The SV corrected for the I^S term according to Equation (31) is represented in **Figure 16**c. **Table 5** reports the regression parameters obtained with both parametric and weighed parametric regressions. The weight, $w_i = \frac{1}{s_{R_I}^2}$, was obtained with various $\%O_2$ and by means of s_{R_I} and according to Equation (). An F-test on the regression variance indicated outlier data. The Ru(dpp)OS has only one outlier for $\%O_2 = 100$, PtTPP exhibits outliers for $\%O_2 > 50$ and PdTFPP has outliers for $\%O_2 > 20$. From the knowledge of the $K_{SV}^{'}$ value we may determine the limits of application of the SV calibration. From **Figure 14**, and with a resolution of 2% the limit $\%O_2$ values for the studied membranes are 100, 60.7, 19.0 % for Ru(dpp)OS, PtTPP and PdTFPP, respectively. The existence of a $\%O_2$ theoretical maximum value justifies the presence of outliers which are due to the lack of light intensity reading accuracy in the indicated concentration intervals. The determination coefficient very close to the unity ($R^2 \geq 0.999$) confirms the linear model. From **Table 5** it is evident that only the regression parameters obtained with the weighed model are comparable to those in **Table 4**, consequently, w_i cannot be neglected. The case of the PtTPP membrane is a clear example. In fact, the classic regression approach furnishes a $K_{SV}^{'}$ value much larger than the expected one and an intercept much lower than 0 (-0.264) indicating a procedural error. For PdTFPP the error produces effects on the slope. For the Ru(dpp)OS membrane, the low calibration sensitivity renders the results similar for the two regression modes adopted.

4.1.3.2 SV linearity and consistency between I_0/I and τ_0/τ calibrations

In this section we will demonstrate that the inconsistency between the I_0/I and τ_0/τ calibration reported by various authors,[59,79] in many cases is only apparent. The use of unique light source and filters for all membranes was adopted to compare the different sensors. We chose the UV laser LED ($\lambda_{max} = 395\,nm$) because its high power allows 1) to accurately measure life-times; 2) to excite also the Ru(dpp)OS. A drawback of the UV laser LED is anyhow evidenced in **Figure 17**a, where the normalized emission profiles, for the PtTPP membrane, produced with the UV laser LED are compared to those obtained with the UV LED.

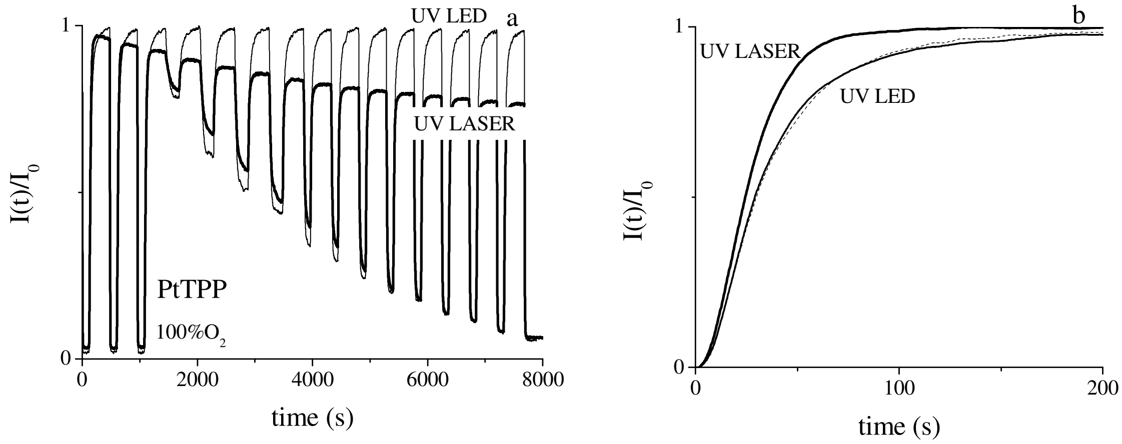

Figure 17. (a). Normalized emission profiles coming from the UV and UV laser LED sources by increasing the $\%O_2$ value, alternated to pure N_2. (b) Particulars of the first step of (a), transition from $\%O_2$ =100 to 0 (100 % N_2). Experimental conditions: PtTPP membrane; T =25°C; P=1Atm; $\%O_2$ after the 3rd step = 0.5, 1, 1.5, 2.5, 3.5, 5, 7.5, 10, 15, 20, 30, 40, 50

Each step refers to increasing $\%O_2$ values alternated to pure N_2. The UV laser LED looses 23.4 % of the signal in 2.2 hours compared to the 0.9 % of the UV LED. The calibration sensitivity increases from 0.133 (UV LED) to 0.189 (UV laser LED). Analogous behaviour was obtained for the other two membranes. Although membranes are thermostated, the experimental system cannot discharge the heat produced by the laser leading to the observed behaviour. This is confirmed by **Figure 17**b in which the emission profile obtained with the laser source is steeper as a result of an increase of the oxygen diffusion coefficient caused by the temperature increase. The two curves relative to the UV LED refer to experiments performed before and after the laser one. Their substantial identity indicates that the laser does not modify the membrane structure. The temperature effect problem may be resolved by pulsing the laser emission and by sampling emissions at the end of the pulse period, when the signal reached a steady-state condition.

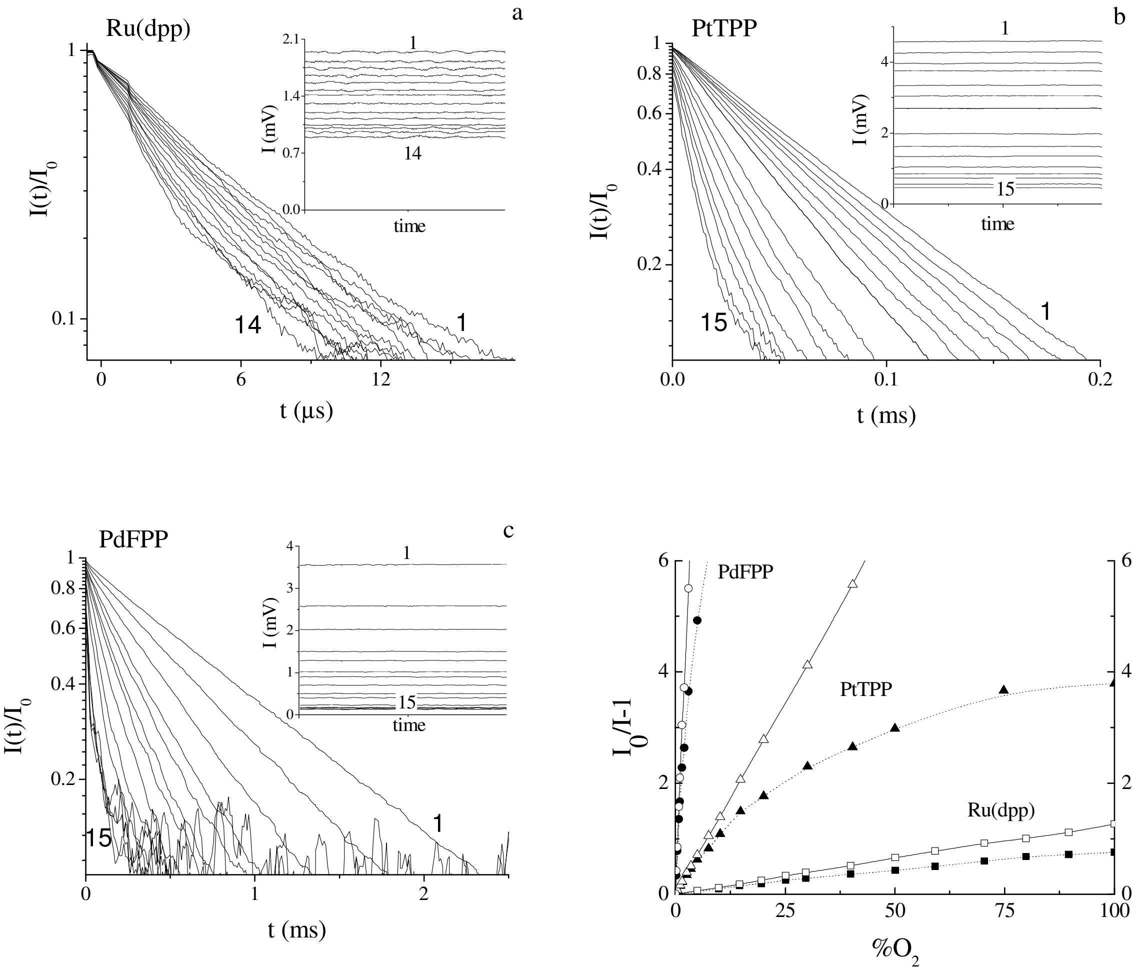

Figura 18. *Normalized decay profiles in logarithmic scale as a function of time for various $\%O_2$ values for Ru(dpp)OS (a), PtTPP (b) and PdTFPP (c). Inset: signal in the last 10% of the pulse width for various $\%O_2$ values. (d) SV calibration plots in terms of I (uncorrected for I^S, empty symbols) and (from mono-exponential fitting, black symbols). $\%O_2$ values as in* ***Figure 16***

The results are reported in **Figura 18** a-c showing the normalized decay profiles in logarithmic scale as a function of time for various $\%O_2$. In this plane all the decays at low $\%O_2$ values are linear demonstrating a mono-exponential behaviour. The curve fitting with a mono-exponential model in the absence of oxygen allows to estimate the life-time, τ_0, of the luminophores in the PSF matrix: 5.5, 83.3 and 1010 μs for Ru(dpp)OS, PtTPP and PdTFPP, respectively. The inset of the figure reports the sampled signal. All the data are resumed in **Figura 18** (d) where both SV calibrations in terms of I (uncorrected for I^S, empty symbols) and τ (obtained from the mono-exponential fitting, black symbols) are plotted.

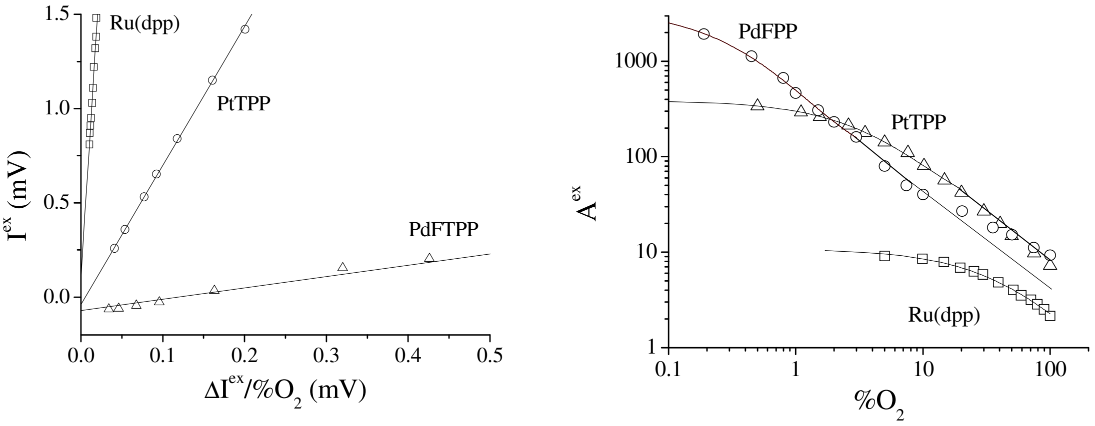

***Figure 19**. a) Regressions of the experimental data according to Equation (37) to obtain the I^S value. b) Regressions of the experimental data according to Equation (49) to obtain the A^F value*

***Table 6.** Regression parameters relative to **Figure 19** (a,b)*

method	***Label***	***F-test n/n$_{tot}$***	$K'_{SV,I}$	$s_{K'_{SV,I}}$	I^S (mV)	s_{I^S} (mV)	R^2	I_0 (mV)	$\%x_s$
I	Ru(dpp) OS	12/13	0.014	0.001	0.178	0.090	0.997	2.05	10.5
	PtTPP	12/15	0.136	0.004	-0.039	0.009	0.999	4.59	-0.86
	PdTFPP	11/15	1.79	0.06	-0.071	0.009	0.998	3.56	-2.05
method	***Label***	***F-test n/n$_{tot}$***	$K'_{SV,\tau}$	$s_{K'_{SV,\tau}}$	A^F $(mV\cdot\mu s)$	s_{A^F} $(mV\cdot\mu s)$	R^2	A_0 $(mV\cdot\mu s)$	$\%A^F$
A	Ru(dpp) OS	12/13	0.0135	0.0009	0.36	0.30	0.994	11	3.4
	PtTPP	12/15	0.140	0.003	11.7	2.0	0.999	389	3.0
	PdTFPP	10/15	1.79	0.03	32.6	23.2	0.999	3523	1.0

In the condition adopted the two calibration modes are not coincident. The same result is obtained also with a two-exponential fitting.

Let us apply the theoretical consideration above reported. **Figure 19**a,b report the calibrations in terms of *I* and emission area, A^{ex}, according to Equation 32 and Equation (48), respectively (regression parameters are reported in **Table 6**). The $\%x_s$ values experimentally obtained agree with those obtained with different light sources. In particular, the 10.5 value for the Ru(dpp)OS is obtained also with the BLUE LED demonstrating that a unquenchable contribution is present. The values for the other membranes are negative but their absolute value is in both cases lower. This is consistent with the fact that with the laser source the I^B / I_0 ratio is lower with respect to the UV LED source. Both regressions on *I* and *A* point out I^S and A^F contributions and allow to estimate the K'_{SV} value as regression parameter. The found K'_{SV} values with *I* and *A*, reported in **Table 6**, are statistically equivalent and are equivalent to those reported in **Table 5** demonstrating the correctness of the experimental choice: the pulse allows the membrane to maintain the temperature set up. Known I^S e A^F, it is now possible to obtain the new SV calibrations according to Equation (37) and (49). The results are reported in **Figure 20**. It is evident that both calibrations in terms of I and τ are now linear and quite close one another. The results are reported in **Table 7**. Data obtained with *I* are more accurate than those obtained with *A*.

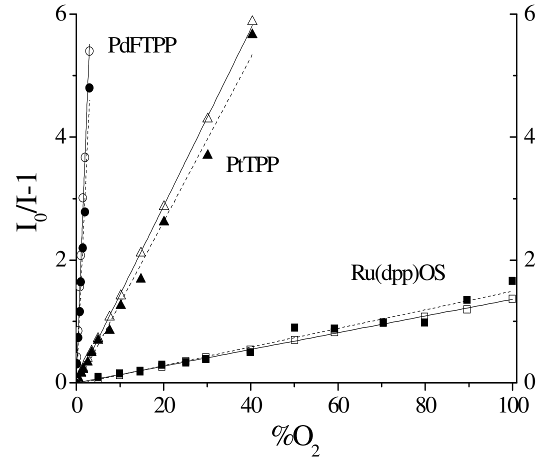

Figure 20. *SV calibration plots in terms of I and τ according to eq. (37) (black symbols) and (49) (empty symbols). $\% O_2$ values as in Figure 16*

Table 7. *Weighed parametric regressions relative to calibrations in* ***Figure 20***

membrane	SV	P_{1w}	$s_{P_{1w}}$	K'_{SV}	$s_{K'_{SV}}$	R^2
Ru(dpp)OS	I	0.0001	0.0061	0.0136	0.0004	0.9991
	τ	-0.021	0.044	0.015	0.002	0.96
PtTPP	I	-0.004	0.011	0.144	0.001	0.9997
	τ	-0.046	0.058	0.134	0.004	0.991
PdTFPP	I	0.07	0.11	1.799	0.049	0.996
	τ	-0.022	0.087	1.68	0.09	0.990

4.2 DRIFT CORRECTION

4.2.1 *Experimental Section*

4.2.1.1 Sensing membrane preparation

The PSF membranes investigated were set A membranes, prepared by spin-coating onto a glass support (10x10x1 mm), as detailed in **Table 3** in Chapter 3.6

4.2.1.2 Instrumentation

The oxygen sensor employed is described in chapter 3.7

4.2.2 *Theoretical section*

Luminescence emission intensity diminishes as a consequence of luminophore degradation producing a signal drift. This drift has to be compensated: intensity values, $I(t)$, collected at various moments must be referred to time t_0 corrected intensity $I(t_0)$, when $I_0(t_0)$ has been collected. Intensity drift ID may be defined as:

$$ID = \frac{1}{I(t_0) - I^B} \cdot \frac{I^{ex}(t) - I^{ex}(t_0)}{t - t_0} = \frac{1}{I^{ex} - I^B} \cdot \frac{\Delta I}{\Delta t} \tag{50}$$

$I^{EX} - I^B$, where I^B is the background light emission, is a normalizing term, necessary to remove non-SV, drift-insensitive contributions. Drift may be determined measuring $I_0(t)$ and inserting it in Equation 50.

$$ID = \frac{1}{I_0^{ex}(t_0) - I^B} \cdot \frac{I_0^{ex}(t) - I_0^{ex}(t_0)}{t - t_0} = \frac{1}{I_0^{ex}(t_0) - I^B} \cdot \frac{\Delta I_0}{\Delta t} \tag{51}$$

where $I_0(t)$ is the light intensity at time t for $\%O_2=0$.

According to Equation 51 the Stern-Volmer background corrected equation (Equation 31), referring to $I(t_0)$ instead of $I(t)$, becomes:

$$\frac{I_0^{ex}(t_0) - I^T}{I(t_0) - I^T} = 1 + K_{SV} \cdot \%O_2 \tag{52}$$

From Equation 50 the correlation between $I(t_0)$ and $I(t)$ may be achieved:

$$I(t_0) = \frac{I^{ex}(t) + ID \cdot \Delta t \cdot I^{B}}{1 + ID \cdot \Delta t} \tag{53}$$

and defining $d(t) = \dfrac{1}{1 + ID \cdot \Delta t}$:

$$I(t_0) = [I^{ex}(t) - I^{B}] \cdot d(t) + I^{B} \tag{54}$$

Inserting Equation 54 in Equation 52 the modified Stern Volmer Equation is obtained:

$$\frac{I_0^{ex}(t_0) - I^{S}}{[I^{ex}(t) - I^{B}] \cdot d(t) + I^{B} - I^{S}} = 1 + K_{SV} \cdot \%O_2 \tag{55}$$

It can be rearranged as follow:

$$I^{ex}(t) \cdot d(t) = \frac{1}{K_{SV}^{'}} \cdot \frac{I_0^{ex}(t_0) - I^{ex}(t) \cdot d(t)}{\%O_2} + I^{B} \cdot [d(t) - 1] \cdot \left(1 + \frac{1}{K_{SV}^{'} \cdot \%O_2}\right) + I^{T} \tag{56}$$

Equation 56 may be used to determine K'_{SV} and I^{T} for drift affected data. If the drift may be ignored, $DI=0$ and $d(t)=1$, Equation 56 becomes equivalent to Equation 32 reported in Chapter 4.1.

$$I_i^{ex} = \frac{1}{K_{SV}^{'}} \cdot \frac{\Delta I_i^{ex}}{\%_{O_2}} + I_i^{S} + I_i^{B} = \frac{1}{K_{SV}^{'}} \cdot \frac{\Delta I_i^{ex}}{\%_{O_2}} + I_i^{T} \tag{32}$$

4.2.3 Experimental section

We can notice a drift in normalized luminescence intensity profiles (**Figure 21**), more significant for Ru(dpp)OS membranes. It is mainly due, at room temperature, to photodegradation of the luminophore.

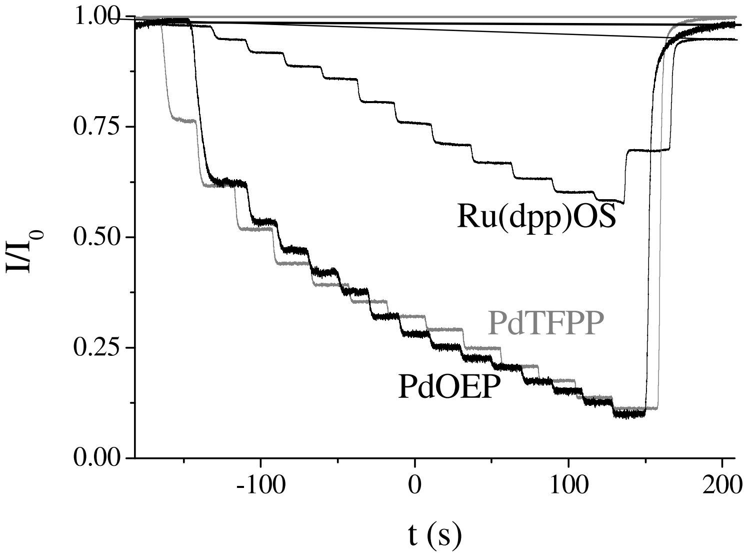

Figure 21. *Normalized luminescence intensity profiles for three membranes embedding Ru(dpp)OS (black thin line), PtTFPP(grey line) and PdOEP (black thick line), by increasing %O$_2$, reported in* ***Table 8****. Straight lines represent calculated drift for the tree membranes*

Table 8. *Oxygen percentages relative to* ***Figure 21***

%O$_2$ Ru(dpp)OS	*%O$_2$ PtTFPP*	*%O$_2$ PdOEP*
0	0	0
5	2	1
10	4	1.5
15	6	2
20	8	2.5
30	10	3
40	12	4
50	14	5
60	16	6
70	20	7
80	25	8
90	30	10
	40	12
	50	15
		20

Results are reported in **Table 9**. Room temperature drift is relevant for Ru(dpp)OS only, so that drift correction for porphyrin based membranes has been neglected.

Table 9. *Drift and calibration parameters*

Membrane	***ID (s^{-1})***	***I^T (mV)***	***K'_{SV}***
Ru(dpp)OS -PSF	**$-1{,}01\cdot10^{-4}$**	0,017	0,005
PtTFPP-PSF	$-8{,}25\cdot10^{-7}$	0,020	0,155
PdOEP-PSF	$-2{,}87\cdot10^{-6}$	0,022	0,621

In **Figure 22** drift-corrected Stern-Volmer plots for membranes embedding Ru(dpp)OS, PtTFPP and PdOEP are plotted. Regression parameters are reported in **Table 9**.

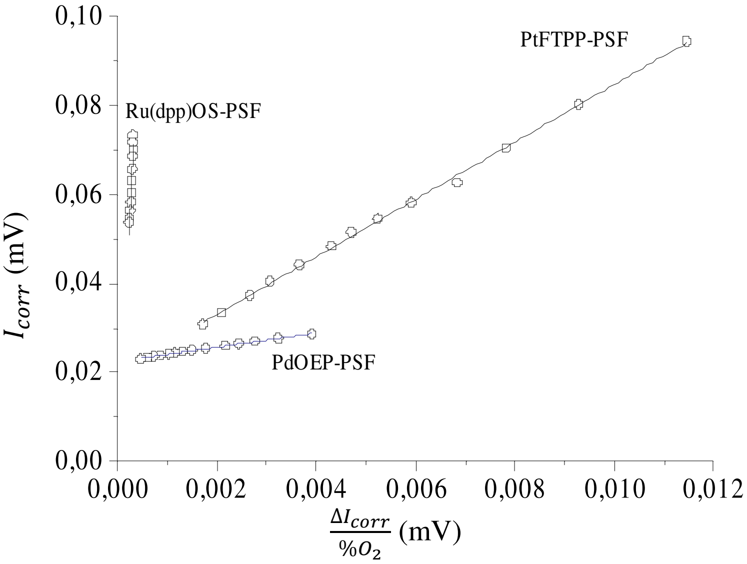

Figure 22. *Corrected Stern-Volmer calibration plots for membranes embedding Ru(dpp)OS, PtTFPP and PdOEP. Ru(dpp)OS plot has been corrected to compensate drift using Equation 56.* $I_{corr} = I(t)d(t)$ $\Delta I_{corr} = I_0(t_0) - I(t)d(t)$

4.3 ARRHENIUS ACTIVATION ENERGIES CALCULATION

Stern-Volmer constant K'_{SV} has strong temperature dependence: it can modify the three parameters in Equation 26 contributing to K'_{SV}: τ_0, D_{O_2} and σ_{O_2}.

$$K'_{SV} \propto \tau_0 \cdot D_{O_2} \cdot \sigma_{O_2} \qquad (26)$$

When %O$_2$=0 we can write temperature dependence of τ_0 expressed according to Ahrrenius formulation

$$\frac{1}{\tau_0} = k_f^0 + A_{nr}e^{-\Delta E_{nr}/RT} \qquad (57)$$

A_{nr} and ΔE_{nr} are a pre exponential factor and the non radiative processes activation energy, respectively. In the presence of a quencher, Equation 57 becomes:

$$\frac{1}{\tau} = k_f^0 + A_{nr}e^{-\Delta E_{nr}/RT} + A_q^0 e^{-\Delta E_q/RT} \qquad (58)$$

A_q and ΔE_q are a pre exponential factor and the quenching process activation energy, respectively.

An analogous equation may be obtained for oxygen diffusion coefficient D_{O_2}

$$D_{O_2}(T) = A_D e^{-\Delta \mathrm{E_D}/RT} \qquad (59)$$

A_D and ΔE_D are a pre exponential factor and the diffusion process activation energy, respectively.

Oxygen solubility into the polymeric membrane is related to its partition coefficient,[81,82] and its temperature dependence can be written as follows:

$$\sigma_{O_2}(T) = A_s e^{-\Delta H_\mathrm{S}/RT} \qquad (60)$$

A_S and ΔH_S are a pre exponential factor and the enthalpy, respectively.

4.3.1 SV calibrations at various temperatures

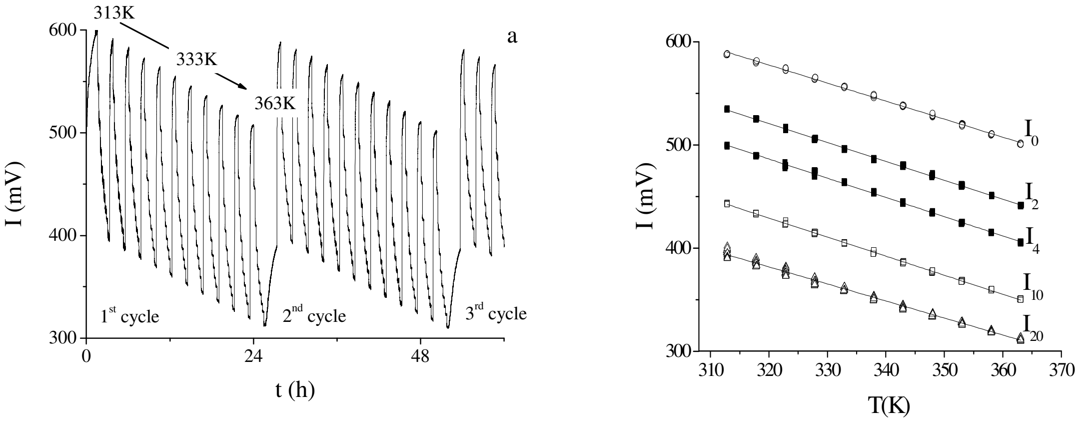

Figure 23. *a) Emission profiles at various temperatures: 40, 45, 50, 55, 60, 65, 70, 75, 80, 85, 90°C for a PtTFPP/PSF membrane. b) Light emitted versus temperature for various oxygen concentration: 0, 2, 4, 10 an 20%. Data ob rained from* ***Figure 23****a*

In **Figure 23**a emission profiles at various temperatures for a PtTFPP/PSF membrane is shown. Temperature has been varied from 40°C to 90°C. Plotting intensity values in equilibrium at various oxygen concentrations (0, 2, 4, 10, 20 %O_2) versus a decreasing in overall emission may be noted. It is due to an increasing in non radiative processes speed. ΔE_{nr} may be obtained fitting I_0 versus T with Equation 61, derived from Stern-Volmer equation taking into account that $\tau_0 = \frac{1}{k_f^0 + k_{nr}}$:

$$I_0 \propto \tau_0 = \frac{1}{k_f^0 + A_{nr} \cdot e^{-\Delta E_{nr}/RT}} \tag{61}$$

ΔE_{nr} obtained is equal to 16.5(0.5) KJ/mol, comparable with the value 14.1 KJ/mol obtained from M. Gouterman e S. Gouin[83] in a fluoroacrylic polymer with the same luminophore.

4.3.2 K'_{sv} variation with temperature.

The experimentally found increase in K'_{SV} with temperature (see **Figure 25**) can be better discussed analyzing the behaviour of τ_0, D_m and σ_{O_2}.

4.3.2.1 *Luminophore lifetime in absence of oxygen* τ_0:

Porphyrin lifetime correlation with temperature can be obtained as the inverse of Equation 57:

$$\tau_0(T) = \frac{1}{k_r + A_{nr} e^{-\Delta E_{nr}/RT}} \tag{62}$$

4.3.2.2 *Oxygen diffusion coefficient* D_{O_2}

In **Figure 24**a luminescence profiles for the various temperature are reported, imposing *t*=0 when gas flux is switched from 20% oxygen to pure nitrogen and oxygen starts diffusing out of the membrane. Diffusion speeds up with temperature, so that profiles recorded at higher temperatures lie above lower temperatures ones. Such profiles can be interpolated with the bi-exponential fitting in Equation 63.

$$I/I_0(t) = a_1 + a_2 \cdot e^{-t/t_1} + a_3 \cdot e^{-t/t_2} \tag{63}$$

Insertion in **Figure 24**a report regression parameters t_1 and t_2 versus *T*. They can be related[84] to D_{O_2} with Equation 64:

$$D_{O_2} \propto 1/t_1 \propto e^{-\Delta E_D/RT} \tag{64}$$

Equation 64 may be rearranged obtaining

$$\ln(t_1) = c + \frac{\Delta E_D}{R} \cdot \frac{1}{T} \tag{65}$$

Fitting parameters are obtained from the linear fit of $\ln(t_1)$ versus $1/T$ plot in **Figure 24**b: *c*=6.82(0.01) and ΔE_D = 2.8 KJ/mol, comparable with the value 1.8 KJ/mol obtained from M. Gouterman e S. Gouin[83] in a fluoroacrylic polymer and 5.0 kJ/mol obtained from X. Lu and M. A. Winnik [85] in a silicone matrix.

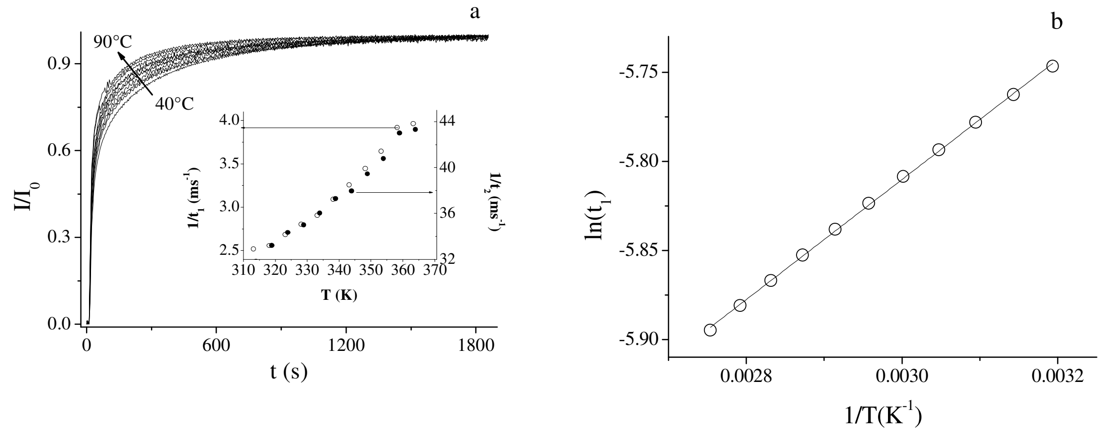

Figure 24. *a) Light emission profiles relative to oxygen diffusion out of the membrane for various temperatures between 40°C and 90°C. Insert graph: fitting parameters of Equation 63 t_1 and t_2 versus T.b) logaritmic plot of data in* ***Figure 24****a insert, fitted with Equation 65 c=6.82(0.01), ΔE_D =2.8(0.1) KJ/mol*

4.3.3 K'_{SV} temperature dependence

Taking into account Equations 59, 60 and 64 and Equation 26 reported below, we may write:

$$K'_{SV} \propto \tau_0 \cdot D_{O_2} \cdot s_{O_2} \tag{26}$$

$$K_{SV} \propto \tau_0 \cdot D_{O_2} \cdot \sigma_{O_2} \propto \frac{e^{-(\Delta E_D + \Delta H_S)/RT}}{1 + a \cdot e^{-\Delta E_{nr}/RT}} \tag{66}$$

In **Figure 25**a are reported the SV plots relative to the various calibrations in **Figure 23**. In **Figure 25**b K'_{SV} obtained are plotted versus T. Inserting previously obtained parameters ΔE_{nr} and ΔE_D in Equation 66 gives us an estimated value for ΔH_S of 13(3)kJ/mol.

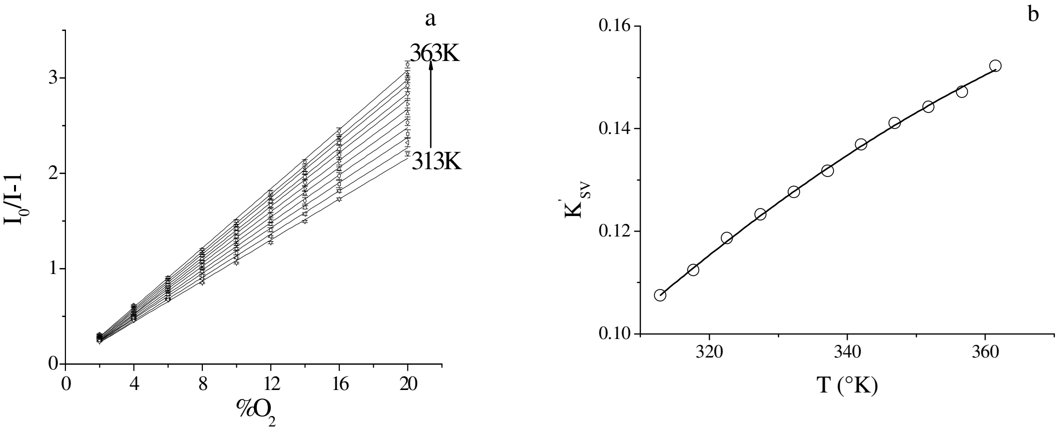

Figure 25. *a) SV calibration plots on* ***Figure 23*** *data, recorded at various temperatures. b)* K'_{SV} *obtained in* ***Figure 25****a versus temperature. Interpolation model as in Equation 66*

4.4 CALIBRATION MODELS UNDER DYNAMIC CONDITIONS

The usual Stern-Volmer calibration is based on static measurement of luminescence but the aim of this chapter is to demonstrate that many useful information may be obtained under dynamic conditions recording the light emission profile on passing from a generic oxygen mixture to nitrogen. In particular, the usual SV calibration model (Model (I)),[84] based on the light intensity ratio, I_0/I, will be compared in terms of sensitivity, precision and working interval to other two Models[86]. One based on the light emission profile and on its inflection point (Model (II)); the other based on a suitable integral of the light emission profile (Model (III)). The three Models will be used to monitor three polysulfone-based sensitive membranes employing Ru(dpp)OS, PtTPP and PdTFPP.[59,87] Digital simulation will help to understand the nature of the physical constants defined in the model equations, enlightening the meaning of the chosen approaches.

4.4.1 Experimental Section

4.4.1.1 Sensing membrane preparation

The PSF membranes investigated were set C ones (see **Table 3** in Chapter 3.6), prepared by dip-coating onto a glass support (10x30x1 mm) under nitrogen atmosphere, as detailed in Chapter 3.5.1

4.4.1.2 Instrumentation

The oxygen sensor employed is described in Chapter 3.7

4.4.2 Calibration Model (II): inflection point position of emission profiles.

The SV calibration Model (I) may be represented as

$$R_I = \frac{I_0}{I} - 1 = P_1 + P_2 \cdot \%O_2 \qquad (67)$$

In this Model the regression parameters P_1 and P_2 represent the 0 and the K'_{SV} values respectively. The SV equation is a general tool to monitor the molecular oxygen by using fluorescence quenching but its precision depends on the nature of the sensing membrane, that is, on the lifetime of the luminescent label together with the nature of the host polymer (permeability). The equation describing the oxygen diffusion inside the polymeric membrane is the usual second Fick's law. Here it is written in terms of oxygen percentage in a mixture, $\%O_2(x,t)$, located at the spatial coordinate *x* along the membrane thickness, and at temporal coordinate *t*:

$$\frac{\partial \%O_2(x,t)}{\partial t} = D_{O_2} \cdot \frac{\partial^2 \%O_2(x,t)}{\partial x^2} \tag{68}$$

(D_{O_2} is the oxygen diffusion coefficient into the membrane). When oxygen comes out of the membrane, this differential equation has the following analytical solution:[39,88]

$$\%O_2(x,t) = \%O_2 \cdot \left[\frac{4}{\pi}\sum_{n=1}^{\infty}\frac{1}{n}e^{-k_n \cdot t} \cdot \sin\left(\frac{n \cdot \pi \cdot x}{2 \cdot L}\right)\right] \tag{69}$$

$\%O_2$ represents the initial oxygen composition at equilibrium at 1 Atm. It is homogeneous along the membrane of thickness, *L*. The constant k_n is defined as:

$$k_n = \frac{n^2 \cdot \pi^2}{4} \cdot \frac{D_{O_2}}{L^2} \tag{70}$$

In each infinitesimal membrane layer, *dx,* the luminescence quenching by $\%O_2(x,t)$ is $\partial I(x,t)$ so that, by means of the SV equation with $\partial I_0 = I_0 \cdot dx / L$ the following equation may be obtained:

$$\frac{\partial I_0}{\partial I(x,t)} = 1 + K'_{SV} \cdot \%O_2(x,t) \tag{71}$$

In integral form:

$$I(t) = \frac{I_0}{L} \cdot \int_0^L \frac{dx}{1 + K'_{SV} \cdot \%O_2(x,t)} \tag{72}$$

By assuming n=1 and $\sin\left(\frac{\pi\cdot x}{2\cdot L}\right)=h$ in Equation *69*, and $k_1=k_t$, the integral *72*, after some handling, may be approximated to

$$I(t)\approx\frac{I_0}{L}\cdot\int_0^L\frac{dx}{1+K'_{SV}\cdot\%O_2\cdot\frac{4\cdot h}{\pi}\cdot e^{-k_t\cdot t}}=\frac{I_0}{1+e^{-k_t\cdot t+\ln\left(K'_{SV}\cdot\%O_2\cdot\frac{4\cdot h}{\pi}\right)}} \tag{73}$$

This equation represents a sigmoid which may be linearised as

$$\ln\left(\frac{I_0}{I(t)}-1\right)=-k_t\cdot t+\gamma_{flex}=-k_\gamma\cdot\gamma+\gamma_{flex} \tag{74}$$

with k_γ and $\gamma_{flex}=k_t\cdot t_{flex}$ slope and intercept, respectively. These two parameters are defined by approximated equations obtainable from Equation *73*:

$$k_\gamma\cong\frac{\pi^2}{4}\cong 2.47 \tag{75}$$

$$\gamma_{flex}\cong\ln\left(\frac{4\cdot h}{\pi}\right)+\ln\left(K'_{SV}\cdot\%O_2\right) \tag{76}$$

The γ_{flex} parameter is the dimensionless time position of the sigmoid inflection point. The parameters in the right part of Equation *74* are dimensionless through D_{O_2}/L^2. The simple approximated Equation *73* will be now verified by simulation.

Figure 26a reports the $I(t)$ profiles numerically obtained with various K'_{SV} and switching from pure oxygen to pure nitrogen.[84] In **Figure 26**b the profiles of **Figure 26**a in logarithmic form are drawn (continuous line) together with their fittings (dotted lines) obtained with Equation *74* vs. the dimensionless time, γ (the Model was applied in the $0.2<\gamma<2$ interval). All regressions have determination coefficient equal to unity demonstrating the correctness of the linear model that is the correctness of the approximations to obtain Equation *73* in the chosen interval.

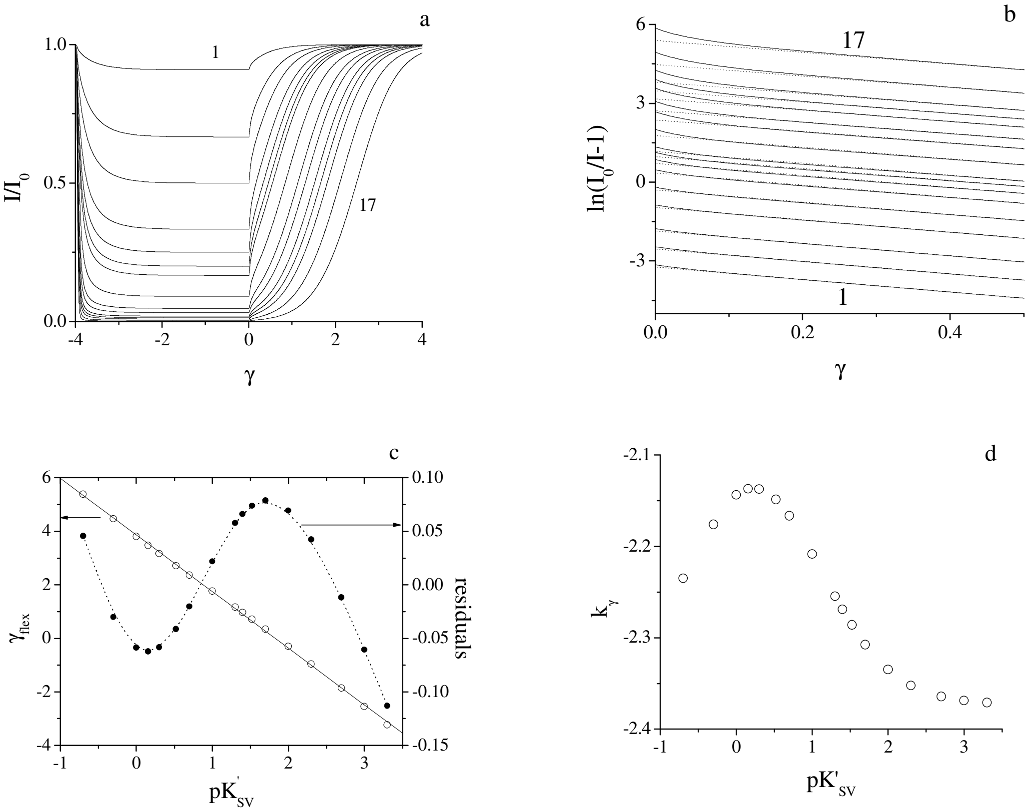

Figure 26. *a) simulated dimensionless emission intensity of an optical oxygen sensor on passing from pure nitrogen to pure oxygen and back, for 15* K'_{SV} *values; b)* $\ln(I_0/I-1)$ *vs.* γ *(continuous line) and linear fitting regression according to Equation* 73*; c)* γ_{flex} *and residuals vs.* pK'_{SV} *(linear fit parameters of Equation* 77*); d)* k_γ *vs.* pK'_{SV}*.*

It is evident that the initial part of the simulated curves is not well fitted at large K'_{SV} values. It is important to observe that all slopes are very similar indicating that i) they are independent of K'_{SV} and that, ii) all the emissions shapes are equal (they are only shifted). For this reason γ_{flex} clearly depends on K'_{SV}. Its dependence is linear in the plot γ_{flex} vs. pK'_{SV} (**Figure 26**c, open circles) and Equation *77* represents the regression equation.

$$\gamma_{flex} = 3.863(0.022) - 2.116(0.013) \cdot pK'_{SV} \quad \left(\mathrm{R}^2 = 0.9994\right) \tag{77}$$

This equation is equivalent to Equation 76 for $\%O_2 = 100$. The generalized form for all oxygen mixtures is the following where decimal logarithms are converted to natural.

$$\gamma_{flex} = -0.369 + 0.919 \cdot \ln\left(K'_{SV} \cdot \%O_2\right) \tag{78}$$

The Model (II) may consequently be written as

$$\gamma_{flex} = P_1 + P_2 \cdot \ln\left(\%O_2\right) \tag{79}$$

where $P_1 = -0.369 + P_2 \cdot \ln\left(K'_{SV}\right)$ and P_2 = 0.919. Contrarily to Model (I), the calibration sensitivity is independent of the membrane nature as P_2 is constant. In **Figure 26**c the residuals are also reported (black circles). Their values are low although not stochastic.

As written above the slopes, k_γ, in **Figure 26**b are essentially equal. **Figure 26**d shows the variation of k_γ with pK'_{SV}. Its variation is between 2.17 and 2.37 with an average of $\bar{k}_\gamma = 2.25(0.09)$. This value is close to that predicted by Equation *75* (2.467). Under this limit $\bar{k}_\gamma$ may be considered as independent from the used luminophore and the membrane nature and structure.

4.4.3 Calibration Model (III): emission areas.

Figure 26a describes the simulated emission profiles associated to various K'_{SV} values. **Figure 27**a represents the simulated emission profiles at constant K'_{SV} value ($K'_{SV} = 0.15$) and for various $\%O_2$. The area, *A*, above the profiles for $\gamma \geq 0$ (the shaded area of curve 1 was drawn as an example) is related to the oxygen amount inside the membrane. In particular, considering the transition from oxygen mixtures to pure nitrogen we may write

$$A = \int_0^\infty \frac{\left(I_0 - I\right)}{I_0} \cdot d\gamma \tag{80}$$

In **Figure 27**b circles indicate the areas of all the simulated curves as a function of the $\%O_2$ in the mixture. As for Model (II), the equation of the physical model associated to the observable “area”, *A*, has been derived to fit the data in **Figure 27**b. Following equation can be obtained from Equations *80* and *74*:

$$A=\int_0^\infty \frac{\left(I_0-I\right)}{I_0}\cdot d\gamma=\int_0^\infty \left(\frac{e^{-k_\gamma\cdot\gamma+\gamma_{flex}}}{1+e^{-k_\gamma\cdot\gamma+\gamma_{flex}}}\right)\cdot d\gamma \tag{81}$$

Solution of this integral is

$$A=\frac{1}{k_\gamma}\cdot\ln\left(1+e^{\gamma_{flex}}\right) \tag{82}$$

From Equation 78 it can be obtained

$$A=\frac{1}{k_\gamma}\cdot\ln\left(1+0.69\cdot\left(K'_{SV}\cdot\%O_2\right)^{0.92}\right) \tag{83}$$

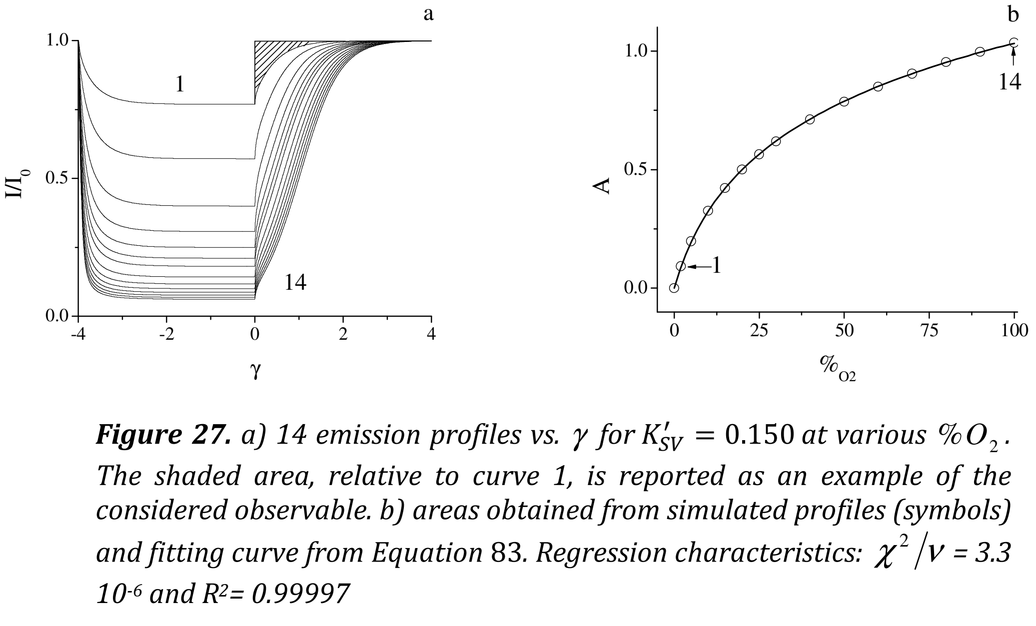

Figure 27. *a) 14 emission profiles vs. γ for $K'_{SV}=0.150$ at various $\%O_2$. The shaded area, relative to curve 1, is reported as an example of the considered observable. b) areas obtained from simulated profiles (symbols) and fitting curve from Equation* 83*. Regression characteristics: χ^2/ν = 3.3 10^{-6} and R^2= 0.99997*

The correctness of this Model may be verified by fitting the areas obtained from simulated profiles with Equation *83* using k_γ and K'_{SV} as regression parameters, $\%O_2$ being the independent variable. We obtain $k_\gamma=2.19$ and $K'_{SV}=0.158$. The fitting is very good as demonstrated the continuous line in **Figure 27**b characterized by χ^2/ν = 3.3 10^{-6} and R^2= 0.99997. The found k_γ value is identical to the theoretical one obtainable from **Figure 26**d with $K'_{SV} = 0.15$. The K'_{SV} value is 5% larger than the theoretical one. The Model (III) Equation *83* may be finally expressed as

$$A = P_1 \cdot \ln\left(1 + P_2 \cdot \%O_2{}^{0.92}\right) \tag{84}$$

In this equation $P_1 = \dfrac{1}{k_\gamma}$ and $P_2 = 0.69 \cdot \left(K'_{SV}\right)^{0.92}$ are the regression parameters for fitting the experimental data.

4.4.4 Comparison among calibration sensitivities of the three Models

The aim of this paragraph is to compare the three Models in terms of calibration sensitivities, S_i. Sensitivity is the first derivative of the Model equations with respect to $\%O_2$.

Model (I): $$S_{RI} = \left|\frac{d(R_I)}{d\%O_2}\right| = K'_{SV} \tag{85}$$

Model (II): $$S_\gamma = \left|\frac{d\gamma_{flex}}{d\%O_2}\right| = \frac{0.919}{\%O_2} \tag{86}$$

Model (III): $$S_A = \left|\frac{dA}{d\%O_2}\right| = \frac{0.63 \cdot \left(K'_{SV}\right)^{0.92} \cdot \%O_2{}^{-0.08}}{\bar{k}_\gamma \cdot \left(1 + 0.69 \cdot \left(K'_{SV} \cdot \%O_2\right)^{0.92}\right)} \tag{87}$$

The sensitivity of Model (I) depends on the membrane characteristics. In particular, high sensitivity is associated to high K'_{SV} value. On the contrary, in Model (II), S_γ is independent of membrane and luminophore nature. Moreover, it is inversely proportional to the oxygen concentration. In Model (III) S_A depends on both K'_{SV} and $\%O_2$. When $K'_{SV} \cdot \%O_2$ is sufficiently large, S_A depends only on $\%O_2$:

$$S_A \cong \frac{0.919}{\bar{k}_\gamma \cdot \%O_2} \tag{88}$$

This fact implies that for large $\%O_2$ the calibration plot is independent of the used membrane and luminophore, as for Model (II). At low $\%O_2$

$$S_A \cong \frac{0.63\cdot\left(K'_{SV}\right)^{0.92}\cdot\%O_2^{\,-0.08}}{\bar{k}_\gamma} \tag{89}$$

In this case sensitivity strongly depends on the membrane nature (K'_{SV}). The three sensitivities may be compared as follows.

a) $S_{R_I} > S_\gamma$ is true for $K'_{SV}\cdot\%O_2 > 0.919$ that is for $pK'_{SV} < \log\left(\frac{\%O_2}{0.919}\right)$

b) $S_\gamma > S_A$ is always true

c) $S_{R_I} > S_A$ is true for $K'_{SV}\cdot\%O_2 > 1.2\cdot10^{-7}$ (that is experimentally always true)

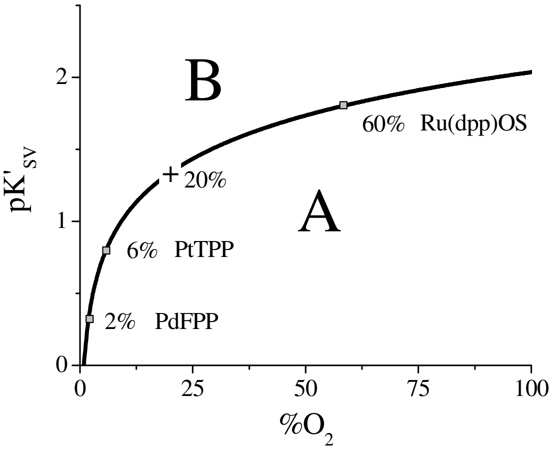

Figure 28. *Comparison among the sentivities, S, of the three Models. Zone A:* $S_{R_I} > S_\gamma > S_A$ *; Zone B:* $S_\gamma > S_{R_I} > S_A$*. The three membranes are individuated by theirs* pK'_{SV} *individuating three %O2 (squares) so that Model (I) is more sensitive with Ru(dpp)OSOS for* $\%O_2 > 60$*, with PtTPP for %O2 > 6, and with PdTFPP for %O2 > 2. The plus symbol indicates* $\%O_2 = 20$ *(air) where* $pK'_{SV} = 1.34$

In c) the inequality is always true as $1.2\cdot10^{-7}$ implies to work with $\%O_2$ lower than $1.2\cdot10^{-5}$ for $K'_{SV} = 0.01$. The three comparisons may be visualized by plotting

$pK'_{SV} = \log\left(\frac{\%O_2}{0.919}\right)$ vs. $\%O_2$ (**Figure 28**). This function, representing $S_{R_I} = S_\gamma$, cuts the plane into zone A and B characterized by the following inequalities:

Zone A: $S_{R_I} > S_\gamma > S_A$

Zone B: $S_\gamma > S_{R_I} > S_A$

Model (I) is more sensitive in zone A and Model (II) more sensitive in zone B. The three membranes used in this paper are represented in **Figure 28** with their pK'_{SV} values, namely $pK'_{SV} \cong 1.8$ for Ru(dpp)OS, $pK'_{SV} \cong 0.8$ for PtTPP and $pK'_{SV} \cong 0.3$ for PdTFPP (grey squares). The $\%O_2$ at which one method becomes more sensitive than the other is represented by the quoted $\%O_2$. In other words, sensitivity of Model (I) is always greater than the other two for $\%O_2 > 60$ for Ru(dpp)OS, for $\%O_2 > 6$ for PtTPP, and for $\%O_2 > 2$ for PdTFPP. Consequently, having to work close to $\%O_2 = 20$, it is better to use Model (II) with membranes having $pK'_{SV} > 1.34$ (Ru(dpp)OS for instance), whilst for membranes with $pK'_{SV} < 1.34$ Model (I) is preferable (porphyrins, for instance).

4.4.5 Comparison among precisions of the three Models

In this paragraph we will compute the $\%O_2$ measurement precision, $s_{\%O_2}$, of the three Models. Precision depends on the chosen Model and on the precision of the experimental R_I, γ_{flex} and A parameters.

4.4.5.1 Precision of Model (I).

In Model (I), R_I is a composed measurement ($\frac{I_0}{I} - 1$), and its error, $s_{R_I} = s_{\frac{I_0}{I}-1}$, may be estimated from the errors propagation assuming $s = s_{I_0} = s_I$.

$$s_{R_I} = \frac{s}{I} \cdot \sqrt{1 + \left(\frac{I_0}{I}\right)^2} = \frac{s}{I_0} \cdot \left(1 + K'_{SV} \cdot \%O_2\right) \cdot \sqrt{1 + \left(1 + K'_{SV} \cdot \%O_2\right)^2} \qquad (90)$$

This equation indicates that more precise measurements are obtained with low $K'_{SV} \cdot \%O_2$. For a given membrane (that is for a given K'_{SV}) Equation *90* indicates that the standard deviation of R$_I$ increases with the $\%O_2$ value, so that the regression must be weighed with[78]

$$w_i = 1 / s_{R_I}^2 \tag{91}$$

The Model becomes:

$$R_I = P_{1w} + P_{2w} \cdot \%O_2 \tag{92}$$

where P_{1w} and P_{2w} are intercept and slope of the weighed model, respectively. The precision is defined by: [78]

$$s_{\hat{x}_0} = \frac{s_{y/x,w}}{P_{2w}} \cdot \left(\frac{1}{m \cdot w_{\hat{x}_0}} + \frac{1}{\sum w_i} + \frac{(\hat{x}_0 - \overline{x}_w)^2}{\sum w_i \cdot (x_i - \overline{x}_w)^2} \right)^{1/2} \tag{93}$$

Where $\hat{x}_0$ is the discriminated $\%O_2$ value; $\overline{x}_w$ is the mean value weighed on all the used $\%O_2$ levels; x_i is the $\%O_2$ level of the i^{th} measurement; $s_{y/x,w}$ is the standard deviation of the regression accounting for the weighed dispersion of the data; $s_{\hat{x}_0} = s_{\%O_2}$ is the precision; m is the R_I measurement repetition number.

4.4.5.2 Precision of Models (II) and (III).

The estimate of the $s_{\gamma_{flex}}$ relative to the Model (II) must be obtained from the experimental profile fitting procedure of the γ_{flex} parameter. The estimate of the s_A relative to the Model (III) may be obtained only by repeating the measurement at the same $\%O_2$ value.

4.4.6 Experimental check of the Models

4.4.6.1 Experimental emission profiles.

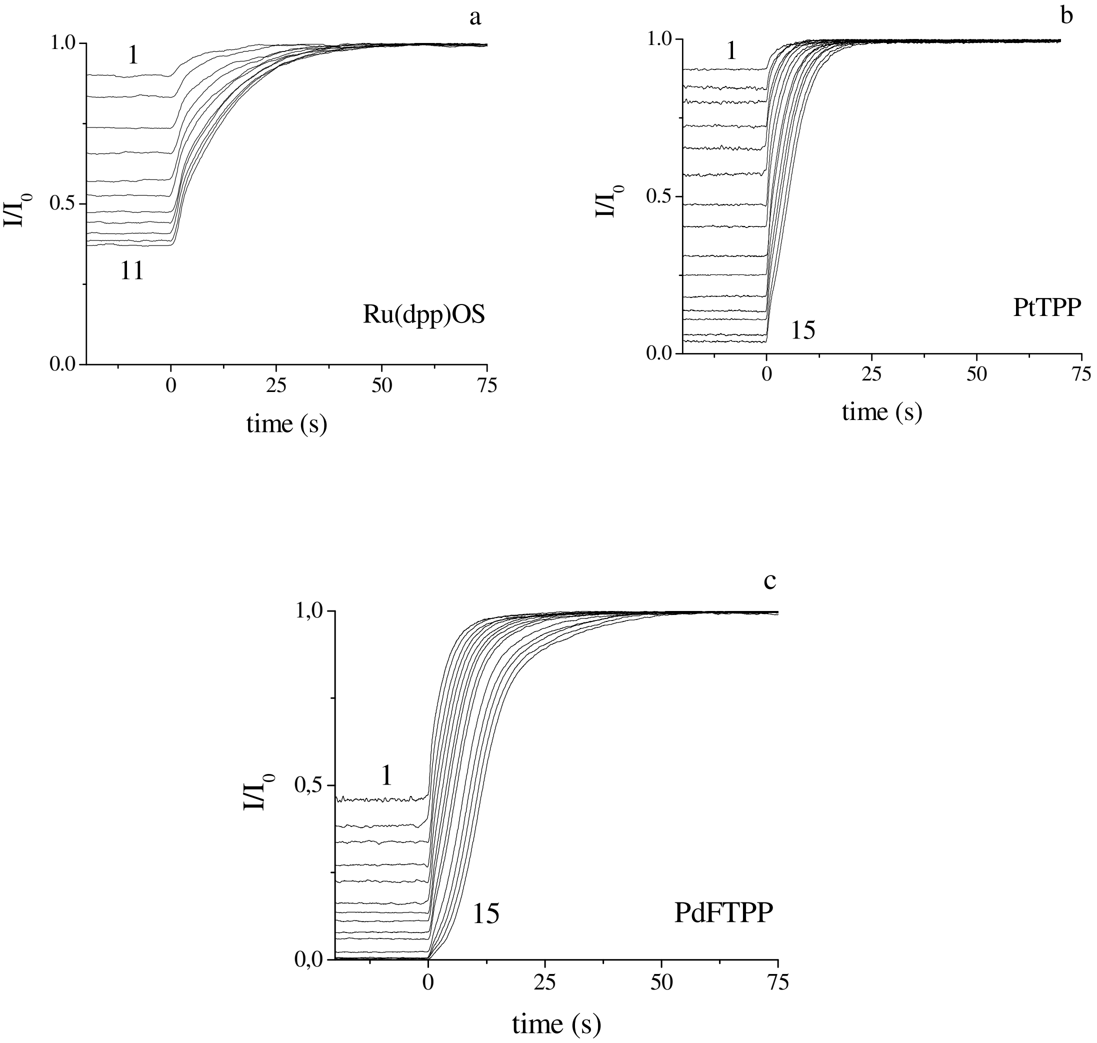

Figure 29. *Experimental, normalized emission profiles vs.* $\%O_2$ *for Ru(dpp)OSOS (a), PtTPP (b) and PdTFPP (c), respectively. Data were corrected for* I^B*. For the Ru(dpp)OSOS membrane;* $\%O_2$ *= 5.6,10.4, 19.5, 27.8, 40.3, 48.7, 59.5, 70.7, 80.3, 90.5, 98.4. For the PtTPP membrane:* $\%O_2$ *= 0.7, 1.2, 1.6, 2.5, 3.5, 5.1, 7.4, 9.9, 14.8, 20.0, 30.8, 40.0, 49.7, 74.7, 100.0. For the PdTFPP membrane:* $\%O_2$ *= 0.7, 0.9, 1.1, 1.5, 2.0, 3.0, 4.0, 5.0, 7.4, 9.9, 20.2, 34.8, 50.1, 76.0, 100.0.*

Figure 29 reports the experimental profiles obtained with the three membranes by varying the $\%O_2$ amount. All profiles were corrected for the background intensity, I^T, and normalized. The three used luminophores are characterized by quite different life-time so that the relevant membranes have different values of K'_{SV} and the three Models are compared in a wide K'_{SV} range. Ru(dpp)OS ($K'_{SV} = 0.0176$) and PtTPP ($K'_{SV} = 0.146$) - based membranes quench the 62.9 % (curve 11 in **Figure 29**a) and the 96.1 % (curve 15 in **Figure 29**b) of emitted light, respectively, when saturated with $\%O_2 = 100$. PdTFPP exhibits much higher sensitivity ($K'_{SV} = 1.77$). Light emission is completely quenched with $\%O_2 \geq 20$ (**Figure 29**c) and $\%O_2 = 0.7$ lowers light emission of 54.1 %.

4.4.6.2 *Experimental application of Model (I).*

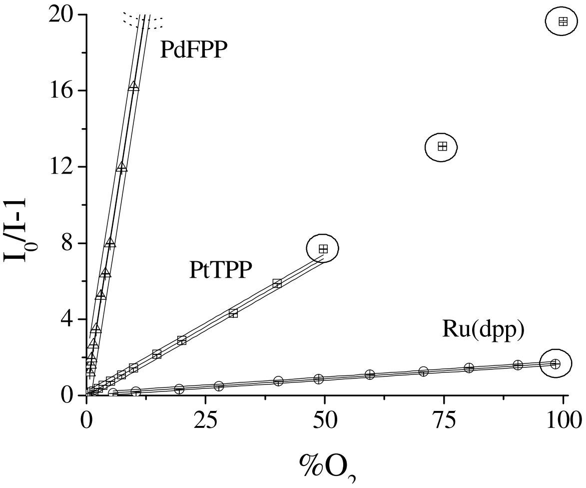

Figure 30. Weighed parametric regressions with prediction bands for Ru(dpp)OSOS (○), PtTPP (□) and PdTFPP (Δ) membranes. Statistical data are in **Table 10**. Circled data are outlayers.

Table 10. *Statistical data of the weighed parametric regressions of the three membranes*

label	***Regression model***	P_{1w}	$s_{P_{1w}}$	P_{2w}	$s_{P_{2w}}$	***F-test*** [a]	***R***^{2}
Ru(dpp)OS	$R_I = P_{1w} + P_{2w} \cdot \%_{O_2}$	0.0004	0.0004	0.0176	0.0001	10/11	0.9990
PtTPP		0.0001	0.001	0.146	0.001	12/15	0.9994
PdTFPP		0.063	0.073	1.768	0.014	11/15	0.9995

[a] The F-test column reports the non-outlayer data used for regression.

In **Figure 30** the usual SV calibration mode is reported (Model(I)). All data in plot were corrected for IB, and normalized before applying the weighed fitting. As in previous chapters , a F-test on the regression variance ($s_{y/x}$) determined outliers (circled data in **Figure 30**). Ru(dpp)OS exhibits only one outlier for $\%O_2 = 98$. PtTPP exhibits outliers data for $\%O_2 > 50$. PdTFPP exhibits outliers for $\%O_2 > 25$ (data outside the plot area). Other authors obtained wider intervals by using more sophisticated instrumentation.[89] The weigh (w) associated to the various $\%O_2$ values must be computed with the errors propagation law, knowing s_{R_I} and assuming $s = s_{I_0} = s_I = s_{I^B}$.

$$s_{R_I} = \frac{\sqrt{2} \cdot s}{I - I^B} \cdot \sqrt{1 + \left(\frac{I_0 - I^B}{I - I^B} \right)^2} \tag{94}$$

The weighed regression parameters are reported in **Table 10**. On the basis of the outlayers data the working intervals are $\%O_2 = 98$, 50 and 25 for Ru(dpp)OS, PtTPP and PdTFPP, respectively.

4.4.6.3 Experimental application of Model (II).

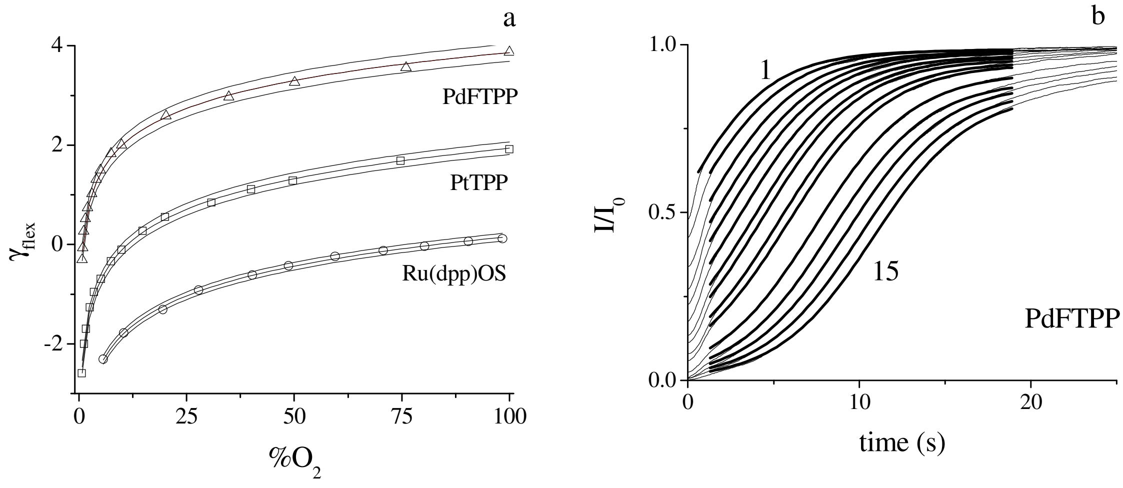

***Figure 31.** a) Parametric regressions with prediction bands obtained with Model (II) for Ru(dpp)OSOS (○), PtTPP (□) and PdTFPP (Δ). Regression parameters are reported in Table 2. b) Fitted profiles (bold line) overlapped to the experimental data of PdTFPP.*

Table 11. *Regression parameters of Model (II)*

label	Regression model	P_1	s_{P_1}	P_2	s_{P_2}	R²
Ru(dpp)OSOS	$A = P_1 \cdot \ln\left(1 + P_2 \cdot \%O_2^{\,0.92}\right)$	5.88	0.31	0.038	0.003	0.999
PtTPP		2.63	0.08	0.136	0.009	0.999
PdTFPP		2.99	0.05	1.459	0.071	0.999

Figure 31a represents γ_{flex} vs. $\%O_2$. The γ_{flex} values are obtained from the experimental emission profile curve fitting of the three membranes through Equation *79*. Prediction bands are also reported. The great advantage of this Model with respect to Model (I) is that all data points lays inside the prediction bands so that it is very stable in the whole 0 – 100 $\%O_2$ range. It is independent of the luminophore nature as calibration is independent of K'_{SV}. The P_{2w} values reported in **Table 11** are similar so that they are independent of the nature of the membrane, as expected. Moreover, they are close to the theoretical value, 0.919. The difference is due both to experimental errors and to the linear approximation adopted in the theoretical model. The estimate of K'_{SV} may be obtained from the already discussed $P_{1w} \approx -0.369 + P_{2w} \cdot \ln(K'_{SV})$. K'_{SV} =0.018, 0.135 and 1.85 for Ru(dpp)OS, PtTPP and PdTFPP, respectively has been obtained. These values are very close to that obtained with Model (I) so that it may be concluded that the physical nature of the parameters P_{1w} and P_{2w} has been correctly interpreted. **Figure 31**a indicates that curve shapes are equal and they are only shifted owing to the different pK'_{SV} values, therefore,

$$\Delta P_{1w} \approx -2.116 \cdot \Delta pK'_{SV} \qquad (95)$$

As the curve shape is independent of the luminophore and polymer nature, the most suitable sensing membrane will be prepared for the chosen application. **Figure 31**b reports the curve fitting of the PdTFPP membrane as an example. The regression quality is very good as indicated by the fitting parameters ($R^2 \geq 0.99998$ and $\chi^2/\nu \leq 4.36 \cdot 10^{-6}$). The first order kinetic rate constant values are 0.110(0.0013) s^{-1}, 0.397(0.017) s^{-1} and 0.351(0.010) s^{-1} for Ru(dpp)OSOS, PtTPP and PdTFPP, respectively.

4.4.6.4 Experimental application of Model (III).

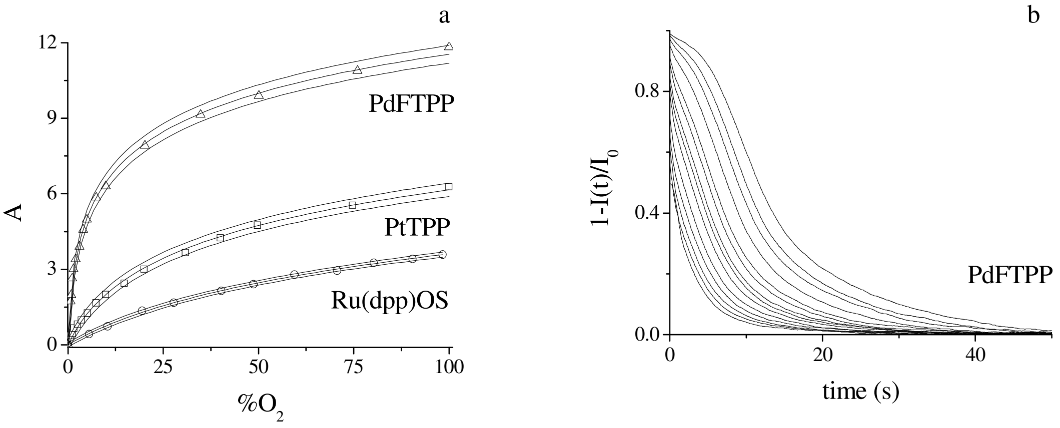

Figure 32. *a) Parametric regressions with prediction bands obtained with Model (III) for Ru(dpp)OS (○), PtTPP (□) and PdTFPP (Δ);* $A = \frac{\bar{k}_\gamma \cdot A^{ex}}{P_1}$. *Regression parameters are reported in Table 3. b) Profiles in terms of 1-I(t)/I0 relative to the experimental data of PdTFPP.*

Table 12. *Regression parameters of Model (III) (see* ***Figure 32****a).*

label	***Regression model***	P_{1w}	$s_{P_{1w}}$	P_{2w}	$s_{P_{2w}}$	***R²***
Ru(dpp)OSOS	$\gamma_{flex} = P_{1w} + P_{2w} \cdot \ln(\%O_2)$	-3.80	0.04	0.86	0.03	0.9990
PtTPP		-2.15	0.03	0.89	0.03	0.9993
PdTFPP		0.13	0.03	0.85	0.03	0.9991

Figure 32a represents A vs. $\%O_2$. The A values were obtained from the integral of the experimental emission profile of the three membranes (Equation *80* with time in seconds). Regression curves were obtained with Equation *83* and their statistical parameters are reported in Table 4. Equation *83* in dimensional form may be written $P_1 = \frac{1}{k_t}$. The obtained k_t values are 0.17(0.01), 0.38(0.01) and 0.34(0.01) for Ru(dpp)OS, PtTPP and PdTFPP, respectively, and they are comparable to those obtained with Model (II). The F-test did not evidence any outlayers so that, as in Model (II), the Model (III) has the advantage to discriminate also large $\%O_2$. The K'_{SV} values derived from P_2 are 0.04(0.01), 0.17(0.01) and 2.2(0.1) for Ru(dpp)OS, PtTPP and PdTFPP, respectively. They are of the

same order of magnitude of those computed with Model (I) and slightly larger than the reference values owing to the approximated Equation *83*. For a practical use, Model (III), expressed in Equation *83*, may be simplified as follows

$$A = P_1 \cdot \ln\left(1 + P_2 \cdot \%O_2\right) \tag{96}$$

4.4.6.5 Comparison among precisions of the experimental Models

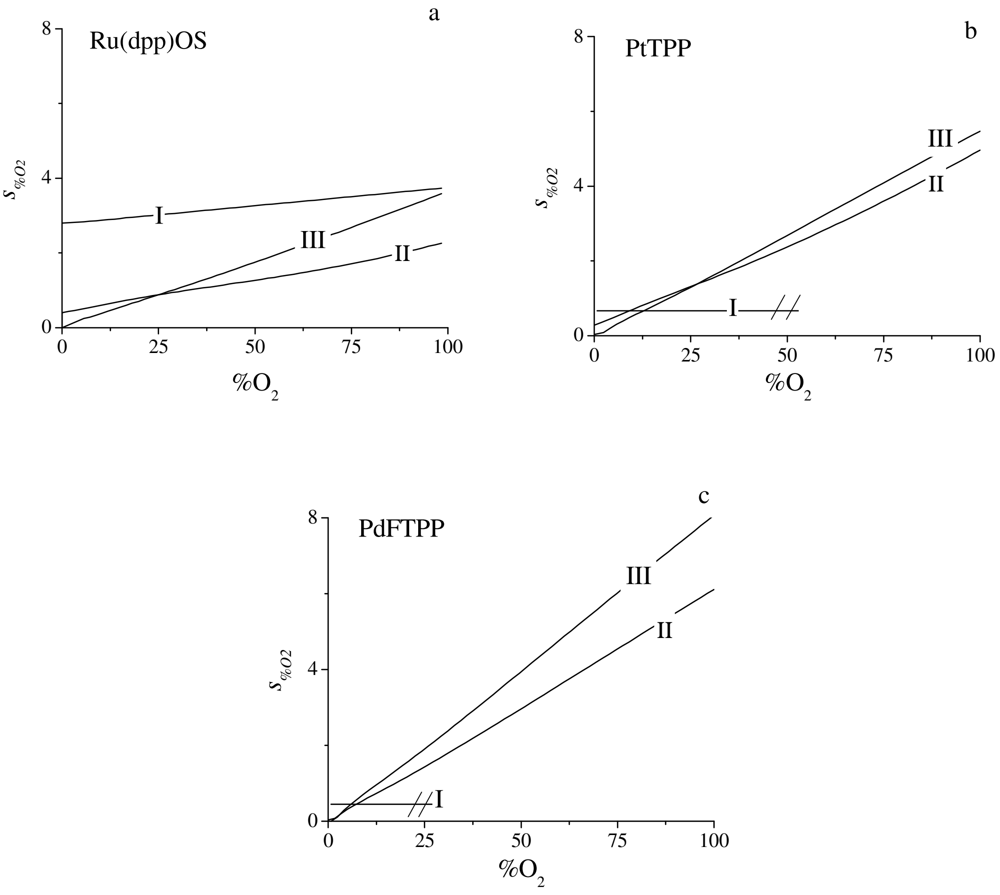

Figure 33. *Precisions, $s_{\%O_2}$, vs. $\%O_2$ obtained with calibration Models (I), (II) and (III). Membrane: a) Ru(dpp)OSOS, b) PtTPP and c) PdTFPP.*

Figure 33 reports the experimental precision $s_{\%O_2}$ vs. $\%O_2$ of the three calibration models applied to the three membranes. The precision of Model (I) is almost constant as foreseen by a linear model. The Ru(dpp)OS membrane precision shows a slight increase. Averaged experimental precision values of 3.5, 0.7 and 0.4 % were found for Ru(dpp)OS, PtTPP and PdTFPP, respectively, so that precisions improve by increasing the calibration sensitivity. A very precise membrane works in a narrower working range. The oblique segments reported in **Figure 33** indicate the upper $\% O_2$ calibration limits. Models (II) and (III) have increasing $s_{\% O_2}$ values with $\% O_2$, as expected. On the basis of the working interval, Models (II) and (III) are preferable because they span in the whole 0-100 $\% O_2$ interval. Moreover, at low oxygen concentration, they are always more precise than Model (I). On the other hand, Model (I) is more precise for very sensitive membrane such as the porphyrin-based ones at $\% O_2 \geq 10$ for PtTPP and $\% O_2 \geq 6$ for PdTFPP as foreseen by the inversion of calibration sensitivity described in **Figure 28**.

4.5 RATIONALIZATION OF THE BEHAVIOUR OF A BI-LABEL OXYGEN OPTICAL SENSOR

In this chapter the behaviour of an optical oxygen sensor prepared by embedding two luminophores in the same polymeric layer will be rationalized with the aim of widening the oxygen concentration quantification methods with optimized precision in the whole concentration range. A multi-label sensor is usually prepared to detect multiple analytes[90,91] or for monitoring physical parameters such as temperature, pressure, humidity, etc...[92] The purpose of the bi-label sensing device is to detect a single analyte, oxygen, instead. The aim is to build a "general purpose" oxygen sensor able to detect it both at low and large concentration with optimized precision.

A preliminary theoretical study will indicate the main characteristics of the sensor and will give a guide-line to prepare an optimal bi-label sensor for the required application. These will be completed with experimental tests to verify the sensor performance.

4.5.1 Experimental section

4.5.1.1 Preparation of Oxygen-Sensitive Membranes.

The embranes investigated were prepared by dip-coating onto a glass support (10x30x1 mm) under nitrogen atmosphere as detailed in Chapter 3.5.1.

4.5.1.2 Instrumentation

The oxygen sensor employed is described in chapter 3.7.

4.5.2 Theoretical Section

4.5.2.1 Nature of the light emission process for a bi-label optical sensor.

The SV equation described in Chapter 2.3.1 applies to single luminophore systems. In the case of a sensing layer containing two luminophores M_1 and M_2, in the absence of mutual interaction, from the Stern Volmer model, the following equations may be obtained:

$$\frac{I_0^{M_1}}{I^{M_1}} = 1 + K'_{M_1} \cdot \%O_2 \qquad (97)$$

$$\frac{I_0^{M_2}}{I^{M_2}} = 1 + K'_{M_2} \cdot \%O_2 \qquad (98)$$

where the superscript M_1 and M_2 refers to light intensity emitted by M_1 and M_2.

The overall emission intensity in the presence and in the absence of O_2 is represented by Equation 99 and 100, respectively:

$$I = I^{M_1} + I^{M_2} \tag{99}$$

$$I_0 = I_0^{M_1} + I_0^{M_2} \tag{100}$$

The SV equation for the bi-label system is therefore represented with

$$\frac{I_0}{I} = \frac{I_0^{M_1} + I_0^{M_2}}{I^{M_1} + I^{M_2}} \tag{101}$$

The intensity fraction due to M_1 may be written as

$$x_{M_1} = \frac{I_0^{M_1}}{I_0^{M_1} + I_0^{M_2}} \tag{102}$$

The intensity ratio $\frac{I_0}{I}$ may be obtained by inserting Equations 97, 98 and 102 into 101:

$$\frac{I_0}{I} = \frac{1}{\dfrac{x_{M_1}}{1 + K'_{M_1} \cdot \%O_2} + \dfrac{1 - x_{M_1}}{1 + K'_{M_2} \cdot \%O_2}} \tag{103}$$

Equation 103 is formally identical to the two sites model one[71] relative to a single emitter having two different lifetimes due to different chemical environment. It is anyway conceptually different as in this case there are two emitting molecules. Equation 103, parametric with x_{M_1}, is represented in **Figure 34**a vs. the $\%O_2$.

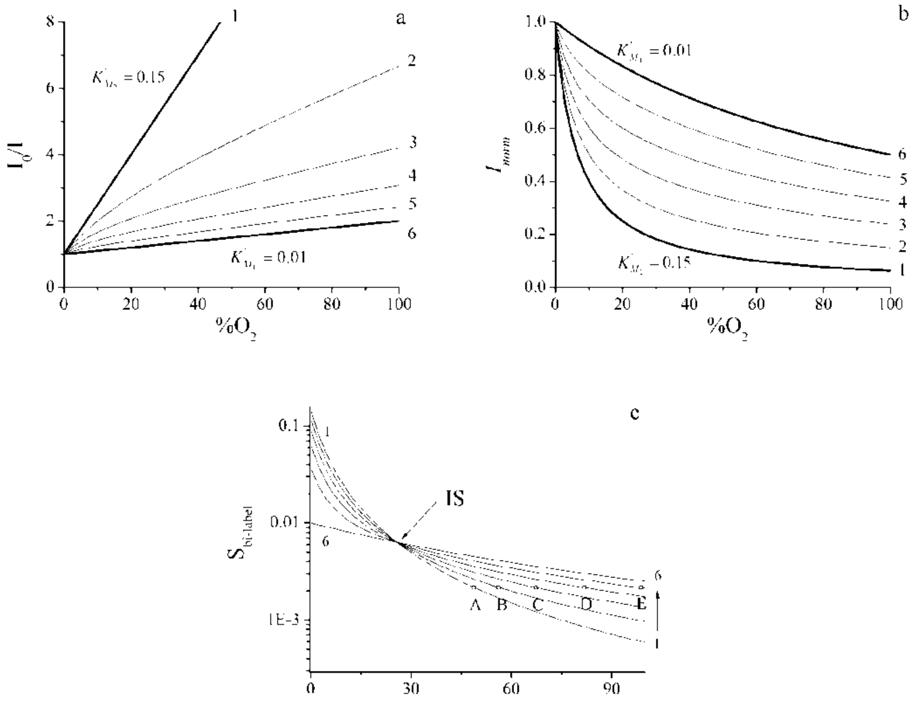

Figure 34. *a) SV calibration plot,* $\frac{I_0}{I}$ *vs.* $\%O_2$*, for bi-label membranes having various luminophores,* M_1 *and* M_2*, composition.* $K'_{M_1} = 0.01$*;* $K'_{M_2} = 0.15$*.* x_{M_1} *= 0.0, 0.2, 0.4, 0.6, 0.8, 1.0 from 1 to 6. b)* I_{norm} *vs.* $\%O_2$ *for membranes described in a). c) Sensitivity in logarithmic scale of the measurement of* I_{norm} *associated to the membrane composition. Horizontal line represents the minimum sensitivity to detect a 1% oxygen variation. Abscissas of points A-E represents the* $\%O_2^{\max}$ *value detectable by the relevant membrane. A = 48 %, B = 56 %, C = 67 %, D = 82 %, E = 98 %*

$K'_{M_1} = 0.01$ and $K'_{M_2} = 0.15$ has been chosen (typical for Ru(dpp)OS, M_1, and PtTPP M_2, in PSF) for M_1 and M_2, respectively, so that when $x_{M_1} = 0$ the layer contains only M_2, and the system has a linear behaviour with slope $K'_{M_2} = 0.15$; when $x_{M_1} = 1$ the layer contains only M_1, and the system has a linear behaviour with $K'_{M_1} = 0.01$. In all the other cases the plot is not linear. Taking into account that the effective measured parameter is *I*, and defining $I_{norm} = \frac{I}{I_0}$, the sensitivity of the bi-label system, $S_{bi-label}$, is represented by the first derivative of I_{norm} taking into account that Equation 103 is its inverse

$$S_{bi-label} = \left| d(I_{norm})/d(\%O_2) \right| = \frac{K'_{M_1} \cdot x_{M_1}}{\left(1 + K'_{M_1} \cdot \%O_2\right)^2} + \frac{K'_{M_2} \cdot x_{M_2}}{\left(1 + K'_{M_2} \cdot \%O_2\right)^2} \qquad (104)$$

The relationship between the experimental measurable, I_{norm} and the analyte concentration is reported in **Figure 34**b. **Figure 34**c shows the corresponding plot $S_{bi-label}$ vs. $\%O_2$. The figure indicates that it is possible to optimize the precision of a bi-label senor in a chosen $\%O_2$ working interval, by modulating the membrane composition. An increase of the less sensitive luminophore amount produces a lower overall sensitivity at low oxygen concentration but higher at larger concentration. The "iso-sensitivity" point, IS ($\%O_2 = 26$ in this case), discriminates these two situations. At this value sensitivity is independent of x_{M_1}. The $\%O_2$ at which the IS appears may be obtained from Equation 104

$$\%O_2^{IS} = \frac{1}{\sqrt{K'_{M_1} \cdot K'_{M_2}}} \qquad (105)$$

The IS point therefore, moves according to the luminophores nature, $K'_{M_1} \cdot K'_{M_2}$. The optimal x_{M_1} is related to the oxygen concentration working interval. In fact, assuming that $3 \cdot s_{I_{norm}}$ is the minimum signal to detect a $\Delta\%O_2$, with $s_{I_{norm}}$, standard deviation of the measurement, obtained as regression standard deviation plot in **Figure 34**b, it follows:

$$S_{bi-label} > \frac{3 \cdot s_{I_{norm}}}{\Delta\%O_2} \qquad (106)$$

The $s_{I_{norm}} = 7 \cdot 10^{-4}$ and $\Delta\%O_2 = 1$ of the reported case generated the horizontal line drawn in **Figure 34**c. The intersection points indicate the upper $\%O_2^{\max}$ value detectable, which is the detection limit obtainable with a given membrane. For instance, wishing to work up to 67 % oxygen with an accuracy of 1% (point C in **Figure 34**c), membranes 1 and 2 cannot be used. On the other hand membranes 3-6 are suitable for the analysis although characterized by differing precisions. One of the most important characteristic of a bi-label sensor is that it furnishes a good precision at large $\%O_2$ (after the IS point) keeping a quite high precision also at low $\%O_2$ (before the IS point).

4.5.2.2 Light emission correction for eddy sources in a bi-label system.

In Chapter 4.1 has been demonstrated that the real emission value must be evaluated breaking up the non-quenchable light coming from the luminophores, the real background light emission and the light absorbed by the luminophores inside the membrane. If all these contributions are included in I^T parameter it follows:

$$\frac{I_0}{I} = \frac{I_0^{ex} - I^T}{I^{ex} - I^T} \tag{107}$$

where I_0^{ex} and I^{ex} represent the experimental emission in the absence and in the presence of a generic oxygen amount, respectively. This result allowed to write the following equation for a single label system

$$I^{ex} = \frac{1}{K_{SV}^{'}} \cdot \frac{\Delta I^{ex}}{\%O_2} + I^T \tag{108}$$

where $\Delta I^{ex} = I_0^{ex} - I^{ex}$. Plotting I^{ex} vs. $\frac{\Delta I^{ex}}{\%O_2}$ so that $\frac{1}{K_{SV}^{'}}$ and I^T may be obtained as slope and intercept, respectively. By combining Equation 107 with Equation 103 and rearranging the corrected SV expression for a bi-label system may be obtained:

$$I^{ex} = \left(I_0^{ex} - I^T\right) \cdot \left(\frac{x_{M_1}}{1 + K_{M_1}^{'} \cdot \%O_2} + \frac{1 - x_{M_1}}{1 + K_{M_2}^{'} \cdot \%O_2} \right) + I^T \tag{109}$$

In order to represent in the same graph single and bi-label systems it is useful to define $x = \frac{\Delta I^{ex}}{\%O_2}$ so that Equation 109 becomes

$$I_i^{ex} = \left(I_0^{ex} - I^T\right) \cdot \left(\frac{x_{M_1}}{1 + K_{M_1}^{'} \cdot \frac{\Delta I^{ex}}{x}} + \frac{1 - x_{M_1}}{1 + K_{M_2}^{'} \cdot \frac{\Delta I^{ex}}{x}} \right) + I^T \tag{110}$$

where, $\Delta I^{ex} = I^{ex}_{0,M_1+M_2} - I^{ex}_{M_1+M_2}$. This function represents the physical model description for a bi-label system. A curve fitting procedure made either with Equation 109 or with Equation 110 needs four parameters to be determined, $I^T, x_{M_1}, K^{'}_{M_1}, K^{'}_{M_2}$. Such elevated parameter number renders the fitting procedure less robust so that parameters might lose their physical meaning. The physical meaning of Equation 110 will be discussed but, only for sake of fitting correctness, a simpler function (Equation 111) may be used to make the curve fitting with c_1 and c_2 fitting parameters.

$$\frac{I_0^{ex}}{I} - 1 = c_1 \cdot (\%O_2)^{c_2} \tag{111}$$

4.5.3 Results and discussion

4.5.3.1 Preliminary considerations on luminophores composing a bi-label system.

A regression procedure performed to obtain the four parameters $I^T, x_{M_1}, K^{'}_{M_1}, K^{'}_{M_2}$, from Equation 109 gives, actually, values can be devoid of any physical meaning. The physical value of those four parameters must be therefore obtained independently.

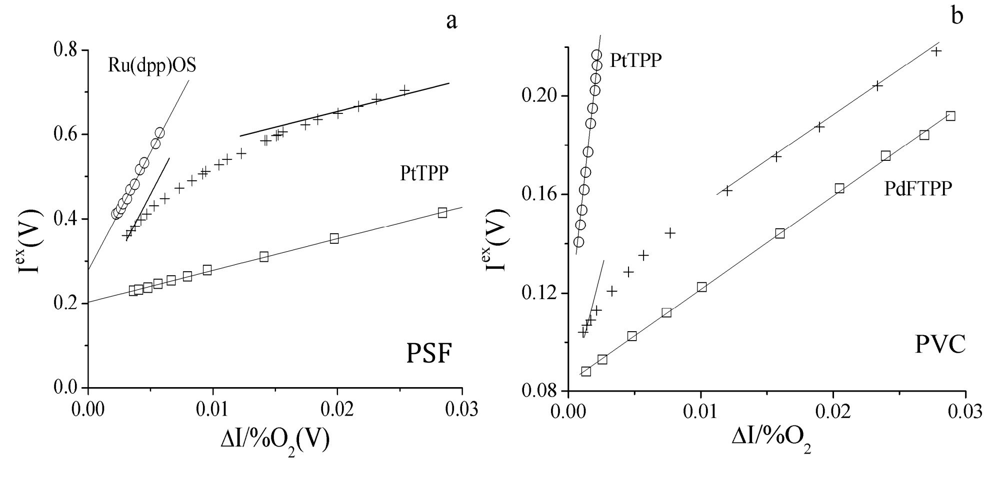

Figure 35. *I_i^{ex} vs. $x = \frac{\Delta I}{\%O_2}$ for PSF-based membrane a) containing (○) Ru(dpp)OS (□) PtTPP (+) bi-label; and for PVC-based membrane b) containing (○) PtTPP (□) PdTFPP (+) bilabel in PVC. Membranes prepared according to conditions reported in* ***Table1***

Figure 35 reports the plot I_i^{ex} vs. $x = \dfrac{\Delta I^{ex}}{\%O_2}$ for three PSF-based membranes (a) containing Ru(dpp)OS, PtTPP, and mixture of them, and three PVC-based membranes (b) containing PtTPP, PdTFPP and a mixture of them. The single-label systems show linear behaviours both in PSF- and PVC-based membranes, whilst a curvature is evident for the bi-label ones. At low $\dfrac{\Delta I^{ex}}{\%O_2}$ values the bi-label membrane behaves like that having the lowest K'_{SV} (Ru(dpp)OS and PtTPP in PSF and PVC, respectively) whilst at large $\dfrac{\Delta I^{ex}}{\%O_2}$ values it resembles that having the largest one (PtTPP and PdTFPP in PSF and PVC, respectively). This fact is easily explained thinking that at low $\%O_2$ only the most sensitive membrane operates whilst at large $\%O_2$ the most sensitive membrane is completely switched off and the less sensitive one is operating. A curve fitting procedure led to obtain the data reported in **Table 13**.

Table 13. *Regression parameters relative to the membranes used in* ***Figure 35***

Membrane	***Label***	I^T ***(V)***	s_{I^T} ***(V)***	$1/K'_{SV}$	$s_{1/K'_{SV}}$	K'_{SV}	***R²***
Ru(dpp)OS/PSF	M_1	0.2786	0.0045	55.67	1.17	0.0180	0.996
PtTPP/PSF	M_2	0.2034	0.0095	7.468	0.073	0.1339	0.9992
PtTPP/PVC	M_1	0.0986	0.0006	52.38	0.40	0.019	0.9995
PdTFPP/PVC	M_2	0.0837	0.0005	3.78	0.03	0.265	0.9996

One way to understand whether the found values have a real physical meaning is the use the relation describing the nature of K'_{SV}. From Equation 30, reported below, it follows:

$$K'_{SV} = \alpha \cdot \frac{4\pi \cdot N \cdot \sigma \cdot p_{tot}}{10^5} \cdot \tau_0 \cdot D_{O_2} \cdot \sigma_{O_2} \qquad (30)$$

$$K'_{SV} \propto \alpha \cdot r \cdot \tau^0 \cdot P \qquad (112)$$

where P is the membrane permeability, r is the distance at which the quenching occurs, α is the quenching efficiency. The life-times, τ^0, of the two luminophores may be obtained from the mono-exponential fitting of the emission decay profile (see Table 3).

Table 14. *Luminophores life-times related to the polymeric matrix.*

Polymer	M_i	Label	$\tau^0(\mu s)$	$\frac{K'_{M_2}}{K'_{M_1}} \cdot \frac{\tau^0_{M_1}}{\tau^0_{M_2}}$
PSF	M_1	Ru(dpp)OS	6.48 (0.01)	0.43
	M_2	PtTPP	78.23(0.06)	
PVC	M_1	PtTPP	72.08(0.09)	1.00
	M_2	PdTFPP	1010(1)	

If P is constant for a given polymer, it is possible to achieve information from the ratio reported in the last column of **Table 14**:

$$\frac{K'_{M_2}}{K'_{M_1}} \cdot \frac{\tau^0_{M_1}}{\tau^0_{M_2}} = \frac{\alpha_{M_2} \cdot r_{M_2}}{\alpha_{M_1} \cdot r_{M_1}} \tag{113}$$

This ratio is equal to unity for the PVC/luminophore system. This result comes from the fact that the two porphyrins have very similar geometries so that $r_{M_1} \cong r_{M_2}$ and $\alpha_{M_1} \cong \alpha_{M_2}$. Moreover, this implies that K'_{M_1} and K'_{M_2} have physical meaning. A more complicated situation is evidenced for the PSF-based membrane when luminophores with completely different structures are used. The 0.43 value of the above defined ratio may be due both to differing α and r values. Winnik found a 1.28 value for the system Ru(dpp)Cl_2 and PtTPP in poly(n-butylamino)thionylphosphazene,[93] consequently, this fact may be ascribe to the differing complex counter ions.

An alternative way to ascribe physical meaning to the parameters above mentioned is based on the assumption that the two luminophores have independent behaviours when both present in the same polymeric matrix. This may be verified with the following procedure

1. Use of $K_{M_1}^{'}$ and $K_{M_2}^{'}$ coming from single label sensors to obtain I^T and x_{M_1} from a curve fitting with Equation 109

2a. Use of an independent way for obtaining x_{M_1} (by emission spectra analysis)

2b. Use of an independent way for obtaining I^T (accordance among single-and bi-label membranes)

1. According to Equation 102 x_{Pt} is defined as the light fraction emitted in N_2 by PtTPP in the bi-label system.

$$x_{Pt} = \frac{I_0^{PtTPP}}{I_0^{PtTPP} + I_0^{M_2}} \tag{114}$$

With I_0^{PtTPP} and $I_0^{M_2}$ light intensities emitted by PtTPP and a generic M_2, respectively, both present in a bi-label sensor. From Equation 109 the following equations for the PSF- and PVC-based membranes ($K_{SV}^{'}$ constants reported in Table 13) may be obtained.

$$I^{ex} = \left(0.745 - I^T\right) \cdot \left(\frac{x_{Pt/PSF}}{1 + 0.1339 \cdot \%O_2} + \frac{1 - x_{Pt/PSF}}{1 + 0.0177 \cdot \%O_2} \right) + I^T \tag{115}$$

$$I^{ex} = \left(0.216 - I^T\right) \cdot \left(\frac{x_{Pt/PVC}}{1 + 0.017 \cdot \%O_2} + \frac{1 - x_{Pt/PVC}}{1 + 0.256 \cdot \%O_2} \right) + I^T \tag{116}$$

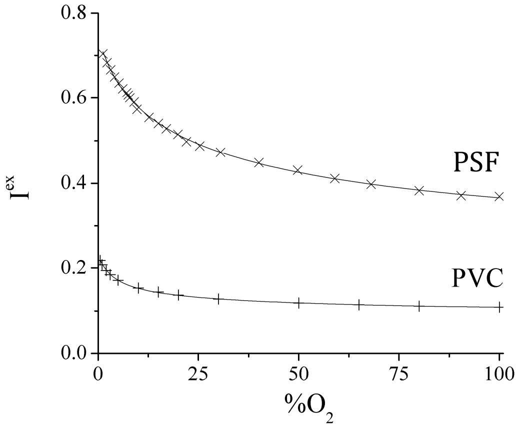

Figure 36. *I^{ex} vs. $\%O_2$ for the two bi-label sensors in PSF (×) and PVC (+).*

Table 15. *Fitting parameters relative to the experimental results reported in Fig. 3. Regression models are Equations 115 and 116.*

Bi-label: $M_1 + M_2$	***matrix***	I^T **(V)**	s_{I^T} **(V)**	x_{Pt}	$s_{x_{Pt}}$	I_0^{ex}	R^2
Ru(dpp)OS + PtTPP	PSF	0.253	0.004	0.45	0.02	0.745	0.999
PtTPP + PdTFPP	PVC	0.090	0.001	0.31	0.01	0.216	0.9995

Figure 36 *shows the experimental result in terms of I^{ex} vs. $\%O_2$ for the two bi-label sensors. The relevant fitting parameters found are reported in*

Table 15.

2a. An independent experiment to obtain the x_{Pt} value is the analysis of the emission spectra recorded for a bi-label and for the single-label systems in the same polymeric matrix.

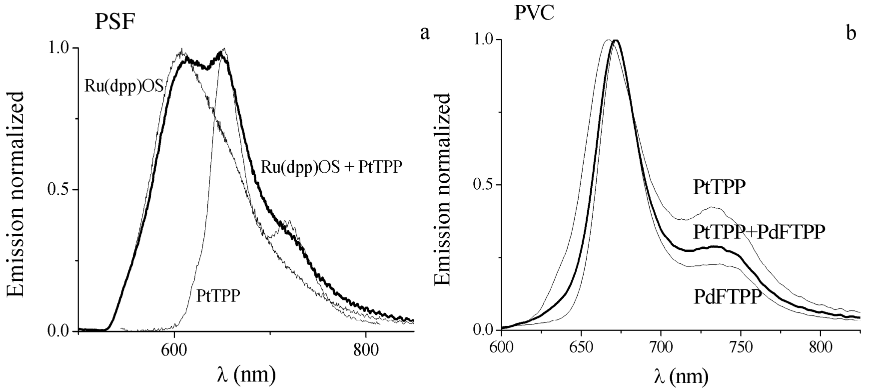

Figura 37 *Normalized emission spectra of individual luminophores and of bi-label system. a) Ru(dpp)OS + PtTPP in PSF; b) PtTPP + PdTFPP in PVC*

Figura 37a and b show emission spectra of the individual luminophores and of bi-label systems in PS and PVC matrices. The x_{M_1} value may be obtained by choosing a suitable wavelength and solving the following equation:

$$I_{M_1+M_2,\lambda_i} = \frac{x_{M_1} \cdot I_{M_1,\lambda_i} + (1 - x_{M_1}) \cdot I_{M_2,\lambda_i}}{x_{M_1} \cdot I_{M_1,\lambda_M} + (1 - x_{M_1}) \cdot I_{M_2,\lambda_M}} \tag{117}$$

where λ_M *is the normalization wavelength for the bi-label system and* λ_i *is the single label measurement wavelength.* $\lambda_M = 648\,nm$ *and* $\lambda_i = 720\,nm$ *in PSF and* $\lambda_M = 671\,nm$ *and* $\lambda_i = 735\,nm$ *in PVC. The* x_{Pt} *values obtained are 0.41(0.07) in PSF and 0.30(0.02) in PVC. Those values are statistically comparable to those reported in*

Table 15.

2b. The validation of the I^T value for the bi-label membrane may be tested by assuming the same membrane thickness and additive contributions of the two labels according to:

$$I^T_{Pt+Ru/PSF} = x_{Pt} \cdot I^T_{Pt} + x_{Ru} \cdot I^T_{Ru} = 0.45 \cdot 0.2037 + 0.55 \cdot 0.276 = 0.244\,V \qquad (118)$$

$$I^T_{Pt+Pd/PVC} = x_{Pt} \cdot I^T_{Pt} + x_{Pd} \cdot I^T_{Pd} = 0.31 \cdot 0.0986 + 0.69 \cdot 0.0837 = 0.088\,V \qquad (119)$$

The obtained values are again comparable to those reported in

Table 15 as demonstrated by a T-test ($s_{I^T_{Pt+Ru}} = 0.01\,V$).These results demonstrate that the two luminophores do not interact each other both in PSF and in PVC. In other words, Equation 109 correctly describes the bi-label model and the bi-label system may be considered as the sum of two single-label systems.

4.5.3.2 SV calibration and precision.

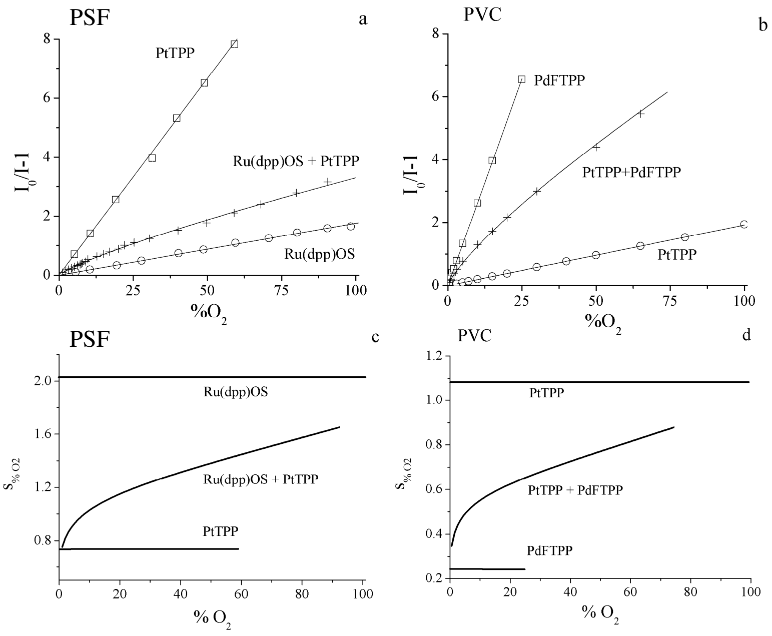

Figure 38. *SV calibrations (Iex corrected for IT) for single and bi-label systems in PS (a) and PVC (b) matrices. Regression data reported in Table 5.* $s_{\%O_2}$ *as a function of* $\%O_2$ *for single and bi-label systems in PS (c) and PVC (d) matrices.*

Table 16. *Estimate of the regression parameters c1 and c2 and their standard deviations s1 and s2, together with determination coefficient R2 for the studied membranes. Parameters c1 and c2 represent slope and intercept of the SV plot relative to the single label membranes and the parameters in Equation 111 for the bi-label membranes, respectively.*

membrane	***c₁***	s_{c_1}	***c₂***	s_{c_2}	R^2
Ru(dpp)OS/PSF	0.0004	0.003	0.0176	0.0004	0.9990
PtTPP/PSF	0.0087	0.025	0.1332	0.0024	0.997
(Ru(dpp)OS + PtTPP)/PSF	0.0769	0.0032	0.816	0.010	0.998
PtTPP/PVC	-0.002	0.003	0.0192	0.0001	0.99990
PdTFPP/PVC	0.0008	0.0070	0.2630	0.0010	0.99994
(PtTPP + PdTFPP)/PVC	0.1982	0.0062	0.7976	0.0074	0.9996

Figure 38 a, b shows membrane calibrations in the SV plane using the $\frac{I_0}{I}-1$ and $\%O_2$ variables. Data are limited to the $\%O_2$ real working interval, excluding outliers, as expected

by the theoretical considerations reported in section 4.5.2 regarding the $\%O_2^{\max}$. **Figure 38** reports also the $s_{\%O_2}$ values as a function of $\%O_2$ for single and bi-label systems in PSF (c) and PVC (d) matrices. $s_{\%O_2}$ of the single label sensor has different constant values, whilst, it ranges between the two values with non-linear shape, the for bi-label one. Clear advantage of the bi-label sensor is the extended working range with respect to the most sensitive membrane and a better precision with respect to the less sensitive one. In other words, $s_{\%O_2}$ depends on the calibration sensitivity.

5 PROGRESS TOWARD COMMERCIAL PROTOTYPE REALIZATION.

5.1 PROTOTYPE CONSTRUCTION

A key step in the progress toward a commercial sensor is the realization of a compact, robust and portable prototype. The attention has been focused on three main issues: maximizing sensor stability, removal of electronic components influence on signal variation, automation of data sampling and elaboration.

5.1.1 Pulsed light source

A pulse generator and a signal processor have been developed with the contribution of AMEL S.r.L. company. The pulsed light source has been employed, instead of a continuous one, in order to minimize the luminophore photo-degradation. Moreover, a pulsed light source prevents the membrane temperature to increase caused by heat irradiation (as seen in Chapter 4.1). A typical pulsed sensor response is shown in **Figure 39**. LED emits a 30 ms light pulse and its emission decreases with time during the first milliseconds. The applied current causes the LED to heat leading to LED emission decrease[94]. Light emitted from the sensing membrane is collected during the last 50 μs of the light pulse, when it has reached a steady value.

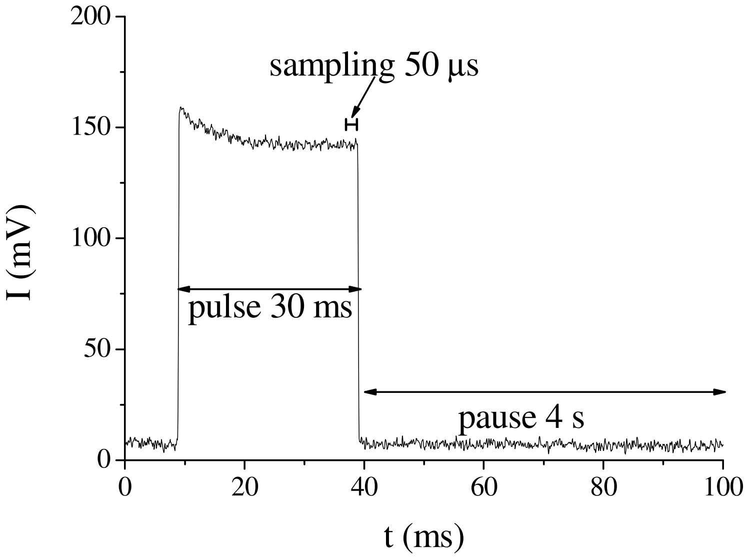

Figure 39. *Light emitted by the sensor excited with a 30 ms LED light pulse each 4 s. Data are collected in the last 50 μs of the light pulse.*

5.1.2 Optical fiber sensor

Temperature affects LED and photodiode efficiency. It leads to a complex dependence of the experimental response on temperature than the dependence illustrated in Chapter 4.3. In order to remove effect due to electronics components on sensor response, LED and photodiode have been coupled to polymeric optical fibers and a PtTFPP-PSF sensing membrane has been deposited directly on the fiber tip, employing the same experimental conditions as in Chapter 3.5.1. In this prototype, as shown in **Figure 40**, only the membrane is subject to temperature variation, whilst electronic components stay out of the oven.

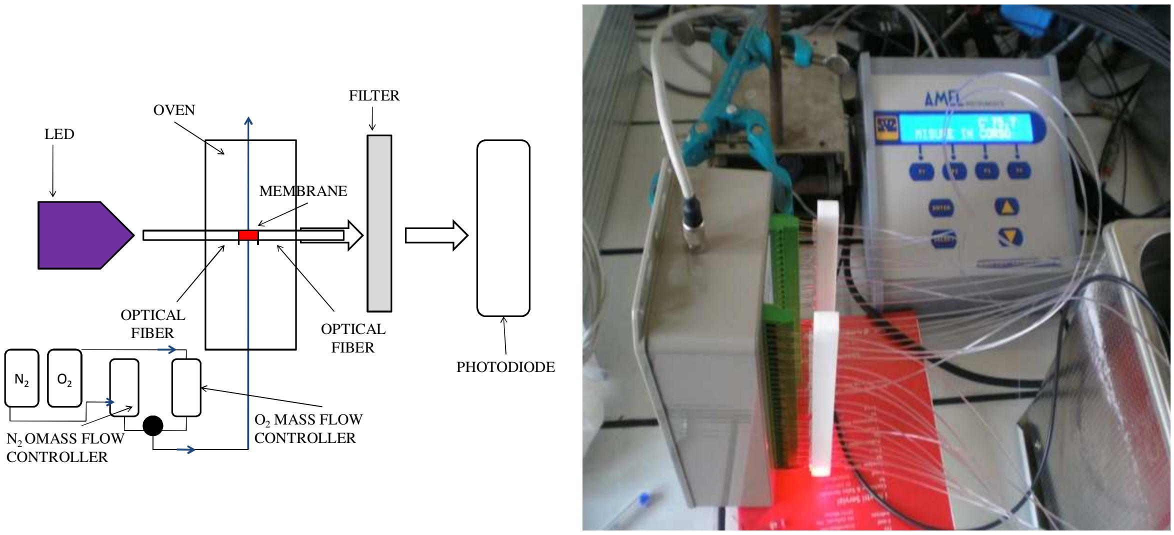

Figure 40. *Optical fiber sensor scheme (left) and photo (right).*

5.1.3 Automation of data sampling and elaboration

A Matlab control program has been developed in order to automate data sampling and elaboration.

- Sampling section:
    - controls mass flow controllers, obtaining a constant gas flow with known oxygen percentage
    - controls oven by setting temperature and waiting for temperature to reach a steady value before starting calibrations
    - digitally converts analog signal from photodiode, averaging it over the sampling time
- Data elaboration section:

- selects light intensities when membrane is at equilibrium with gas phase, obtaining the median
- fits experimental data in order to obtain I^T and K'_{SV} for single label membranes, removing outliers data

Last improvement of the sensor is an array of 32 LEDs, coupled to an optical fiber each, which enables the simultaneous oxygen detection on 32 spots, even with membrane sensitivity individually optimized.

5.2 SENSOR LYFE CYCLE

5.2.1 Membrane conditioning

In order to test sensor stability, a PtTFPP-PSF membrane has been continuously tested 24 hours a day for one month at 90°C and at room temperature with the system described above. A 11 step calibration has been performed every hour to monitor membrane behaviour. K'_{SV} and I_0 obtained during first 3 days after membrane deposition (72 calibration) are reported in

Figure 41.

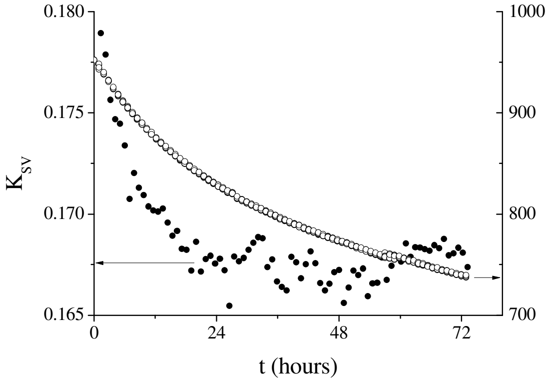

Figure 41. *K'_{SV} (black circles) and I_0 (open circles) versus time, t, during conditioning time of a PtTFPP-PSF membrane*

It must be noticed that K'_{SV} reaches a steady value after 24 hours of conditioning time. Variation is likely due to solvent evaporation from the membrane and/or polymeric chains rearrangement. I_0 drift, discussed in Chapter 4.2, is more evident during conditioning time, but light emission intensity does not reach a steady value due to degradation processes, mainly attributable to thermal degradation of PtTFPP.

5.2.2 Sensor stability and operating life

In order to determine the sensor degradation, K'_{SV} and I^T before and after test and signal decrease have been calculated (see **Table 17**). Signal decrease is expressed as ΔI_0:

$$\Delta I_0 = \frac{I_{0,before} - I_{0,after}}{I_{0,before}} * 100 \qquad (120)$$

Intensities data (background corrected) are reported in **Figure 42**. After the room temperature test, sensor shows only a little light intensity decrease (7.1%). Sensor K'_{SV} and I^T remain unchanged. After the test at 90°C ΔI_0 increases to 28.7% and I^T decreases. This is consistent with the thermal luminophore degradation, affecting both quenchable and non-quenchable luminophore fraction. K'_{SV}, however, remains unchanged even at 90°C and the sensor is fully operating.

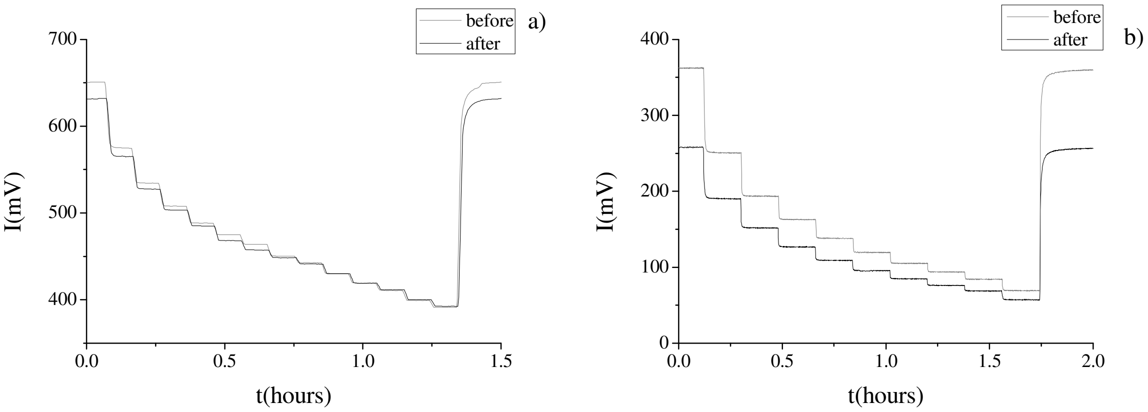

Figure 42. *a) sensor calibration before (red line) and after (black line) one month of continuous test at room temperature. Oxygen calibration concentration: 0, 2, 4, 6, 8, 10, 12, 14, 16, 20, 25, 50, 100%O2. b) sensor calibration before (red line) and after (black line) one month of continuous test at 90°C. Oxygen calibration concentration: 0, 2, 4, 6, 8, 10, 12, 14, 16, 20%O2. Calibrations parameters are reported in Table 17.*

Table 17. *Calibration parameters of data in* ***Figure 42***

Temperature	***K'_{SV} (before)***	***K'_{SV} (after)***	***I^T (before)***	***I^T (after)***	***ΔI_0***
25°C	0.139(0.014)	0.137(0.032)	386.5(4.7)	386.3(1.6)	7.1%
90°C	0.168(0.018)	0.163(0.022)	270.3(2.8)	253.5(4.9)	28.7%

5.3 SENSOR BASED ON RELATIVE INTENSITY MEASUREMENT

Absolute intensity sensors require frequent calibrations and the correction algorithm shown in Chapter 4.2 to compensate light intensity drift. An alternative route is based on relative intensity measurement, unaffected by luminescence drift. A calibration algorithm has been developed for oxygen concentration prediction from luminescence intensity. The algorithm has to take into account every chemical, physical or instrumental factor influencing the luminescence, but has to be as simple as possible. A reference mixture, i.e. air, is flown into the cell alternatively to the sampled mixture. If the time interval between reference and sample measurement is short, membrane drift, LED intensity and photodiode sensitivity variations are negligible. Knowing oxygen percentage of reference mixture, $\%\mathrm{O}_2(\mathrm{R})$, and the measured reference intensity, I_R, from Stern Volmer background corrected Equation 32

$$I_i^{ex} = \frac{1}{K_{SV}^{'}} \cdot \frac{\Delta I_i^{ex}}{\%O_2} + I_i^T \tag{32}$$

the following calibration algorithm may be obtained. It correlates measured light intensity, I_x, with the oxygen percentage in the cell, $\%O_2(x)$.

$$\%O_2(x) = \%\mathrm{O}_2(\mathrm{R}) - K(T) \cdot \frac{I_x - I_R}{I_x - I^T(T)} \tag{121}$$

where $K(T) = \frac{1}{\mathrm{K}_{\mathrm{SV}}'} + \%O_2(R)$. $K(T)$ and $I^T(T)$ have be determined from a quadratic fit of data obtained from calibrations performed at various temperature (Equations 122 and 123)

$$I_s(T) = a' + b'T + c'T^2 \tag{122}$$

$$\mathrm{K}(T) = a + bT + cT^2 \tag{123}$$

Sensor test has been performed fluxing $\%O_2$ =20 (in nitrogen) into the sensor cell as reference gas and then fluxing various oxygen/nitrogen mixtures. This test has been performed at various temperatures between 40 and 75°C and repeated 10 times at each temperature. Intensities data are reported in **Figure 43** a and b. In **Figure 43** c measured $\%O_2$ values versus time are shown. They are uncorrelated to temperature and time, verifying that the algorithm proposed is corrected and intensity drift is compensated. Sensor accuracy can be confirmed by plotting the measured $\%O_2$ versus $\%O_2$ flown into the cell by the mass flow controllers (**Figure 43**d). The slope is quite close to unity, demonstrating a good correspondence between predicted and obtained oxygen percentage.

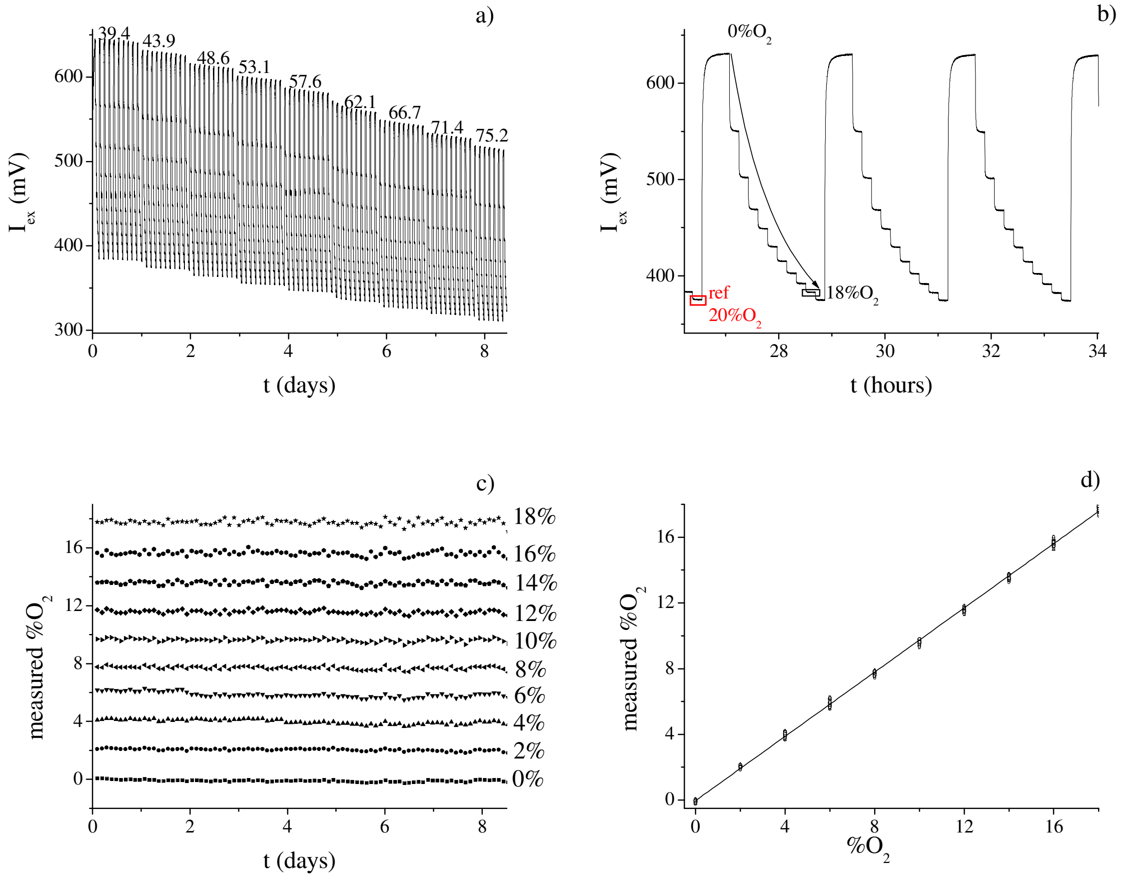

Figure 43. *a)Emitted light intensity during the sensor test at various temperatures, namely 39.4, 43.9, 48.6, 53.1, 57.6, 62.1, 66.7, 71.4 and 75.2°C b)Emitted light intensity during the sensor test at 39.4°C. Oxygen concentration flown into the cell are 0, 2, 4, 6, 8, 10, 12, 14, 16, 18* $\%O_2$*. The reference emitted light intensity (relative to a 20% Oxygen concentration) is evidenced c) Oxygen percentage measured by the sensor for the 10 oxygen concentration levels d) Oxygen percentage measured vs. oxygen percentage determined by mass flow controllers and linear regression performed on all data. Fitting intercept and slope are -0.034(0.011) and 0.9779(0.0010)*

Further confirmation on sensor accuracy comes from sensor analytical performances for every concentration level reported in **Table 18**: relative errors are lower than 4% for every concentration level. Most relative errors are positive, suggesting the presence of a systematic error. It may be due to a misjudging in K'_{SV}, because drift has not been take into account during calibrations. Sensor precision, expressed as standard deviation on the median, is always better than %O_2= 0.3.

Table 18. *Sensor analytical performances for every concentration level*

$\%O_2$	$\%O_{2,median}$	$rel\ error$
0	-0.08(0.20)	N.D.
2	2.08(0.25)	-3.98%
4	4.08(0.30)	-1.69%
6	5.83(0.30)	2.89%
8	7.73(0.26)	3.42%
10	9.64(0.26)	3.59%
12	11.57(0.26)	3.54%
14	13.59(0.23)	2.90%
16	15.64(0.21)	2.28%
18	17.76(0.20)	1.35%

6 CONCLUSIONS

In this PhD thesis a robust optical sensor useful to determine molecular oxygen was prepared. The study was done by testing various luminophore/polymeric matrix couples , starting from tris-4,7-diphenyl-1,10-phenanthroline (Ru(dpp)OS), platinum(II) meso-tetra-phenyl porphyrin (PtTPP) and palladium(II) meso tetra (pentafluoro-phenyl) porphyrin, (PdTFPP) in polysulfone and PVC.

The sensing membrane was mounted either on glass or on optical fiber substrates and exhibits better functioning characteristics compared to available commercial oxygen sensors. Membranes were completely tested in terms of composition, thickness (by ellipsometry) thermal stability, signal stability, light emission profile characteristics (shape, rise time and in general response speed), oxygen concentration range.

Better characteristics come from:

1. Signal improvement coming from the correction of the SV model for light sources unaffected by quenching. Consequence of this was a robust linearization of the SV plots. Experimental data, interpreted with mathematical functions, demonstrated that the curvature from linearity and the discrepancy between data obtained with light emission intensity, I, and in excited state life-time, τ, are only apparent and due to the background emission. Consequently, multisite emission hypotheses or other correction procedures appeared in the literature, must be invoked only after a careful evaluation of the background light really present in the system. After corrections, the sensors behaviour was that foreseen by the SV theory. The proposed equation has the advantage to obtain the K'_{SV} and the effective background with a simple un-weighed regression method.
2. Extension of the working range with dynamic calibrations: the maximum detectable oxygen concentration has been increased using transient intensity light profiles as analytical quantity instead of equilibrium light intensity. Two calibration approaches, alternative to the SV one (Model (I)) have been presented presented. One is based on the emission profile inflection point (Model (II): $\gamma_{flex} \cong P_1 + P_2 \cdot \ln(\%O_2)$), the other, on a suitable integral of the light emission profile (Model (III): $A = P_1 \cdot \ln(1 + P_2 \cdot \%O_2^{0.92})$). The comparison with the classical SV calibration approach (Model (I)) was done in terms of calibration sensitivity, precision and $\%O_2$ working interval. Model (I) works up to $\%O_2$ =98, 50 and 25 with Ru(dpp)OS-PSF, PtTPP-PSF and PdFTPP-PSF,

respectively. The other two models work in the whole 0 – 100 % interval. Model (II) is more sensitive than Model (I) for $\%O_2$ <60, <6 and <2, for Ru(dpp)OS-PSF, PtTPP-PSF and PdFTPP-PSF membranes, respectively. Concerning precision, Models (II) and (III) are preferable than the classic Model (I) at low $\%O_2$ values which exhibits an averaged experimental precisions of 3.5, 0.7 and 0.4 % for Ru(dpp)OS, PtTPP and PdFTPP, respectively. A disadvantage of Model (II) and (III) is that the complete emission profile is required.

3. Optimization of sensitivity for required working range with "bi-label" sensor, embedding two luminophores in the same polymeric membrane. Increasing of sensitivity is achieved by varying luminophores composition. An increase of the less sensitive luminophore amount produces a lower overall sensitivity at low oxygen concentration but higher at larger concentration. The two luminophores behave as if they were independent, giving to the sensing layer enlarged working range with respect to the most sensitive membrane and improved precision with respect to the less sensitive membrane
4. Temperature correction up to 90°C, coupling LED and detector to optical fibres to insulate temperature-influenced electronics from temperature variation in the analyzed mixture. If electronic is thermostated the temperature effect on sensor response is determined only by the sensing membrane and it is easier to take into account.
5. Extended operating time employing pulsed light sources to minimize luminophores photo-degradation. Luminescence drift resulted significant at room temperature only for Ru(dpp)OS membranes ($1{,}01 \cdot 10^{-4}\ s^{-1}$) whilst porphyrin based membranes exhibited a drift at least two order of magnitude smaller. Sensors embedding PtTFPP have been tested continuously 24 hours a day for one month at room temperature and at 90°C.
6. No need of drift compensation and improved robustness with relative intensity-based measurement, using light intensity difference between analyzed and reference mixtuire as analytical parameter. Relative light intensity is not modified by luminophore degradation, variations of LED and photodiode efficiency. Air may be used as reference mixture, providing an inexpensive reference.

Moreover, Stern Volmer constants, K'_{SV}, light intensity in the absence of oxygen, I_0, and response time, t_1, have been determined at various temperatures from 40 to 90°C for PttFPP membranes. From experimental data activation energies of non radiative, ΔE_{nr}, and diffusion processes, ΔE_D, have been determined. Enthalpy, ΔE_s, relative to solubility has been determined too. The obtained data (ΔE_{nr} = 16.5(0.5) KJ/mol, ΔE_D = 2.8(0.3) KJ/mol and ΔE_s = 13(3) KJ/mol) were comparable with those reported in the literature.

REFERENCES

1. IUPAC Compendium of Analytical Nomenclature (Orange Book). a <http://old.iupac.org/publications/analytical_compendium/>
2. Wolfbeis, O.S. Chemical sensors - survey and trends. *Fresenius J Anal Chem* **337**, 522-527 (1990).
3. Hulanicki, A., Glab, S. & Ingman, F. Chemical sensors: definitions and classification. *Pure Appl. Chem.* **63**, 1247-1250 (1991).
4. Thevenot, D.R., Toth, K., Durst, R. & Wilson, G. Electrochemical Biosensors: Recommended Definitions and Classification. *Pure Appl. Chem.* **71**, 2333-2348 (1999).
1. Gründler, P. *Chemical Sensors - An Introduction for Scientists and Engineers*. (Springer: 2007).
6. Cywinski, P.J., Moro, A.J., Stanca, S.E., Biskup, C. & Mohr, G.J. Ratiometric porphyrin-based layers and nanoparticles for measuring oxygen in biosamples. *Sensors and Actuators B: Chemical* **135**, 472-477 (2009).
7. O'Mahony, F.C., O'Riordan, T.C., Papkovskaia, N., Kerry, J.P. & Papkovsky, D.B. Non-destructive assessment of oxygen levels in industrial modified atmosphere packaged cheddar cheese. *Food Control* **17**, 286-292 (2006).
8. Wang, Y. et al. Fluorescence optical fibre sensor provides accurate continuous oxygen detection in rabbit model with acute lung injury. *Respirology* **15**, 99-106 (2010).
9. Baleizão, C., Nagl, S., Schäferling, M., Berberan-Santos, M.N. & Wolfbeis, O.S. Dual Fluorescence Sensor for Trace Oxygen and Temperature with Unmatched Range and Sensitivity. *Analytical Chemistry* **80**, 6449-6457 (2008).
10. Scherer, B. & Woellenstein, J. Optical sensor for online-monitoring of oxygen traces in hydrogen electrolysis. *Sensors and Actuators B: Chemical* **138**, 96-99 (2009).
11. Caillé, S. et al. Sensory characteristics changes of red Grenache wines submitted to different oxygen exposures pre and post bottling. *Analytica Chimica Acta* **660**, 35-42 (2010).
12. Wang, W. et al. Effect Of Oxygen Concentration On The Composting Process And Maturity. *Compost Science & Utilization* **15**, 184-190 (2007).
13. Topal, S.Z., Ertekin, K., Topkaya, D., Alp, S. & Yenigul, B. Emission based oxygen sensing approach with tris(2,2′-bipyridyl)ruthenium(II)chloride in green chemistry reagents: room temperature ionic liquids. *Microchim Acta* **161**, 209-216 (2008).
14. Clark, L. U.S. Patents, n° 2 1956, 913, 386.
15. Ramamoorthy, R., Dutta, P.K. & Akbar, S.A. Oxygen sensors: Materials, methods, designs and applications. *j. Mat.Science* **38**, 4271-4282 (2003).
16. Brailsford, A., Yussouff, M., Logothetis, E., Wang, T. & Soltis, R. Experimental and theoretical study of the response of ZrO2 oxygen sensors to simple one-reducing-gas mixtures. *Sensors and Actuators B: Chemical* **42**, 15-26 (1997).
17. Cao, W., Tan, O.K., Zhu, W., Jiang, B. & Gopal Reddy, C.V. An amorphous-like x[alpha]-Fe2O3-(1 - x)ZrO2 solid solution system for low temperature resistive-type oxygen sensing. *Sensors and Actuators B: Chemical* **77**, 421-426 (2001).
18. Burkhard, D., Hanson, B. & Ulmer, G. ZrO2 oxygen sensors: An evaluation of behavior at temperatures as low as 300°C. *Solid State Ionics* **48**, 333-339 (1991).

19. Xin Guo, Yao-Qing Sun & Kun Cui Darkening of zirconia: a problem arising from oxygen sensors in practice. *Sensors and Actuators B: Chemical* **31**, 139-145 (1996).
20. Kocache, R. Gas sensors. *Sensor Review* **14**, 8-12 (1994).
21. Baldini, F. & Organization, N.A.T. *Optical chemical sensors.* (Springer: 2006).
22. Wolfbeis, O.S. Fiber-Optic Chemical Sensors and Biosensors. *Analytical Chemistry* **78**, 3859-3874 (2006).
23. Bergman, I. Rapid-response Atmospheric Oxygen Monitor based on Fluorescence Quenching. *Nature* **218**, 396 (1968).
24. Wolfbeis, O.S. Materials for fluorescence-based optical chemical sensors. *J. Mater. Chem.* **15**, 2657 (2005).
25. Wolfbeis, O.S. *In Fibre optical fluorosensors in analytical and clinical chemistry from molecular luminescence spectroscopy: methods and applications;* Schulman, S.G.. Ed. Wiley, New York (1988).
26. Borisov, S. et al. Photophysical properties of the new phosphorescent platinum(II) and palladium(II) complexes of benzoporphyrins and chlorins. *Journal of Photochemistry and Photobiology A: Chemistry* **206**, 87-92 (2009).
27. Borisov, S.M., Mayr, T. & Klimant, I. Poly(styrene-block-vinylpyrrolidone) Beads as a Versatile Material for Simple Fabrication of Optical Nanosensors. *Analytical Chemistry* **80**, 573-582 (2008).
28. Florescu, M. & Katerkamp, A. Optimisation of a polymer membrane used in optical oxygen sensing. *Sensors and Actuators B: Chemical* **97**, 39-44 (2004).
29. Oter, O., Ertekin, K. & Derinkuyu, S. Photophysical and optical oxygen sensing properties of tris(bipyridine)ruthenium(II) in ionic liquid modified sol-gel matrix. *Materials Chemistry and Physics* **113**, 322-328 (2009).
30. Ciriminna, R. & Pagliaro, M. Organofluoro-silica xerogels as high-performance optical oxygen sensors. *Analyst* **134**, 1531 (2009).
31. Scheicher, S.R. et al. Optical oxygen sensors based on Pt(II) porphyrin dye immobilized on S-layer protein matrices. *Biosensors and Bioelectronics* **25**, 797-802 (2009).
32. Mcdonagh, C., Shields, A., Mcevoy, A., Maccraith, B. & Gouin, J. Optical Sol-Gel-Based Dissolved Oxygen Sensor: Progress Towards a Commercial Instrument. *Journal of Sol-Gel Science and Technology* **13**, 207-211 (1998).
33. Khalil, G.E. et al. Dual-luminophor pressure-sensitive paint: I. Ratio of reference to sensor giving a small temperature dependency. *Sensors and Actuators B: Chemical* **97**, 13-21 (2004).
34. Chu, C. & Lo, Y. Optical fiber dissolved oxygen sensor based on Pt(II) complex and core-shell silica nanoparticles incorporated with sol-gel matrix. *Sensors and Actuators B: Chemical* **151**, 83-89 (2010).
35. Borchert, N.B., Ponomarev, G.V., Kerry, J.P. & Papkovsky, D.B. O2/pH Multisensor Based on One Phosphorescent Dye. *Analytical Chemistry* **83**, 18-22 (2011).
36. Waskitoaji, W., Hyakutake, T., Watanabe, M. & Nishide, H. Pt-porpholactone- and -porphyrin-based luminescent sensory polymer coating for visualization of oxygen pressure distribution on biplanar surface. *Reactive and Functional Polymers* **70**, 669-673 (2010).
37. Hyakutake, T. et al. Luminescent Sensory Polymer Coating Composed of Platinumporphyrin and Poly(trimethylsilylpropyne) for Real-Time Oxygen Visualization in Operating PEFCs. *Macromol. Chem. Phys.* **212**, 42-47 (2011).
38. Trettnak, W. et al. Optical oxygen sensor instrumentation based on the detection of luminescence lifetime. *Advances in Space Research* **22**, 1465-1474 (1998).

39. McDonagh, C. et al. Phase fluorometric dissolved oxygen sensor. *Sensors and Actuators B: Chemical* **74**, 124-130 (2001).
40. Gonçalves, D. & Irene, E.A. Fundamentals and applications of spectroscopic ellipsometry. *Química Nova* **25**, 794-800 (2002).
41. Aleksandrov, M.L., Asinovskii, L.M., Mel'tsin, A.L. & Tolokonnikov, V.A. Methods and apparatus for complete ellipsometry (review). *J Appl Spectrosc* **44**, 559-578 (1986).
42. Klimant, I. & Wolfbeis, O.S. Oxygen-Sensitive Luminescent Materials Based on Silicone-Soluble Ruthenium Diimine Complexes. *Analytical Chemistry* **67**, 3160-3166 (1995).
43. Mink, L. et al. Platinum(II) and platinum(IV) porphyrin complexes: synthesis, characterization, and electrochemistry. *Polyhedron* **16**, 2809-2817 (1997).
44. Biesaga, M., Pyrzynska, K. & Trojanowicz, M. Porphyrins in analytical chemistry. A review. *Talanta* **51**, 209-224 (2000).
45. Fernández-Sánchez, J.F., Cannas, R., Spichiger, S., Steiger, R. & Spichiger-Keller, U.E. Novel nanostructured materials to develop oxygen-sensitive films for optical sensors. *Analytica Chimica Acta* **566**, 271-282 (2006).
46. O'Neal, D. et al. Oxygen sensor based on the fluorescence quenching of a ruthenium complex immobilized in a biocompatible Poly(Ethylene glycol) hydrogel. *Sensors Journal, IEEE* **4**, 728-734 (2004).
47. Hyakutake, T., Taguchi, H., Kato, J., Nishide, H. & Watanabe, M. Luminescent Multi-Layered Polymer Coating for the Simultaneous Detection of Oxygen Pressure and Temperature. *Macromol. Chem. Phys.* **210**, 1230-1234 (2009).
48. Wu, X., Song, L., Li, B. & Liu, Y. Synthesis, characterization, and oxygen sensing properties of Ru(II) complex covalently grafted to mesoporous MCM-41. *Journal of Luminescence* **130**, 374-379 (2010).
49. Estella, J., Wencel, D., Moore, J.P., Sourdaine, M. & McDonagh, C. Fabrication and performance evaluation of highly sensitive hybrid sol-gel-derived oxygen sensor films based on a fluorinated precursor. *Analytica Chimica Acta* **666**, 83-90 (2010).
50. Shinar, R., Zhou, Z., Choudhury, B. & Shinar, J. Structurally integrated organic light emitting device-based sensors for gas phase and dissolved oxygen. *Analytica Chimica Acta* **568**, 190-199 (2006).
51. Pieper, S.B., Mestas, S.P., Lear, K.L., Zhong, Z. & Reardon, K.F. Phosphorescence characteristics of ruthenium complex as an optical transducer for biosensors. *Appl. Phys. Lett.* **92**, 081915 (2008).
52. Woller, E.K. & DiMagno, S.G. 2,3,7,8,12,13,17,18-Octafluoro-5,10,15,20-tetraarylporphyrins and Their Zinc Complexes: First Spectroscopic, Electrochemical, and Structural Characterization of a Perfluorinated Tetraarylmetalloporphyrin. *The Journal of Organic Chemistry* **62**, 1588-1593 (1997).
53. Lai, S. et al. Electronic Spectroscopy, Photophysical Properties, and Emission Quenching Studies of an Oxidatively Robust Perfluorinated Platinum Porphyrin. *Inorganic Chemistry* **43**, 3724-3732 (2004).
54. Innocenzi, P., Kozuka, H. & Yoko, T. Fluorescence Properties of the Ru(bpy)32+ Complex Incorporated in Sol−Gel-Derived Silica Coating Films. *The Journal of Physical Chemistry B* **101**, 2285-2291 (1997).
55. Gouterman, M. Spectra of porphyrins. *Journal of Molecular Spectroscopy* **6**, 138-163 (1961).
56. Gouterman, M. In Porphyrins; Dolphin, D., Ed.; Academic: New York, Vol. III, pp 1-165. (1978).

57. Shelnutt, J.A. & Ortiz, V. Substituent effects on the electronic structure of metalloporphyrins: a quantitative analysis in terms of four-orbital-model parameters. *The Journal of Physical Chemistry* **89**, 4733-4739 (1985).
58. Che, C. et al. [meso-Tetrakis(pentafluorophenyl)porphyrinato]platinum(ii) as an efficient, oxidation-resistant red phosphor: spectroscopic properties and applications in organic light-emitting diodesElectronic supplementary information available: details of photoluminescence measurements, transient absorption spectra of PtF20TPP, photophysical properties of PtF20TPP in different solvents, EL spectra and performances of OLEDs using PtF20TPP as emitters at various doping levels and crystallographic data for PtF20TPP. See http://www.rsc.org/suppdata/jm/b2/b212204a/. *J. Mater. Chem.* **13**, 1362 (2003).
59. Klimant, I., Ruckruh, F., Liebsch, G., Stangelmayer, A. & Wolfbeis, O.S. Fast Response Oxygen Micro-Optodes Based on Novel Soluble Ormosil Glasses. *Microchimica Acta* **131**, 35-46 (1999).
60. Grenoble, S., Gouterman, M., Khalil, G., Callis, J. & Dalton, L. Pressure-sensitive paint (PSP): concentration quenching of platinum and magnesium porphyrin dyes in polymeric films. *Journal of Luminescence* **113**, 33-44 (2005).
61. Chu, C. & Lo, Y. Ratiometric fiber-optic oxygen sensors based on sol-gel matrix doped with metalloporphyrin and 7-amino-4-trifluoromethyl coumarin. *Sensors and Actuators B: Chemical* **134**, 711-717 (2008).
62. Papkovsky, D.B. New oxygen sensors and their application to biosensing. *Sensors and Actuators B: Chemical* **29**, 213-218 (1995).
63. Fuhrhop, J.H. & Mauzerall, D. One-electron oxidation of metalloporphyrins. *Journal of the American Chemical Society* **91**, 4174-4181 (1969).
64. Draxler, S., Lippitsch, M.E., Klimant, I., Kraus, H. & Wolfbeis, O.S. Effects of Polymer Matrixes on the Time-Resolved Luminescence of a Ruthenium Complex Quenched by Oxygen. *The Journal of Physical Chemistry* **99**, 3162-3167 (1995).
65. Badocco, D., Mondin, A., Pastore, P., Voltolina, S. & Gross, S. Dependence of calibration sensitivity of a polysulfone/Ru(II)-Tris(4,7-diphenyl-1,10-phenanthroline)-based oxygen optical sensor on its structural parameters. *Analytica Chimica Acta* **627**, 239-246 (2008).
66. Mills, A. Optical sensors for oxygen: a log-gaussian multisite-quenching model. *Sensors and Actuators B: Chemical* **51**, 69-76 (1998).
67. Hartmann, P., Leiner, M.J.P. & Lippitsch, M.E. Response characteristics of luminescent oxygen sensors. *Sensors and Actuators B: Chemical* **29**, 251-257 (1995).
68. Mills, A. Controlling the sensitivity of optical oxygen sensors. *Sensors and Actuators B: Chemical* **51**, 60-68 (1998).
69. Han, B., Manners, I. & Winnik, M.A. Oxygen Sensors Based on Mesoporous Silica Particles on Layer-by-Layer Self-assembled Films. *Chemistry of Materials* **17**, 3160-3171 (2005).
70. Mills, A. Response characteristics of optical sensors for oxygen: a model based on a distribution in τo and kq. *Analyst* **124**, 1309-1314 (1999).
71. Carraway, E.R., Demas, J.N. & DeGraff, B.A. Luminescence quenching mechanism for microheterogeneous systems. *Analytical Chemistry* **63**, 332-336 (1991).
72. Demas, J. & DeGraff, B. Luminescence-based sensors: microheterogeneous and temperature effects. *Sensors and Actuators B: Chemical* **11**, 35-41 (1993).
73. James, D.R. & Ware, W.R. A fallacy in the interpretation of fluorescence decay parameters. *Chemical Physics Letters* **120**, 455-459 (1985).
74. Badocco, D., Mondin, A., Fusar, A., Favaro, G. & Pastore, P. Influence of the Real

Background Signal on the Linearity of the Stern–Volmer Calibration for the Determination of Molecular Oxygen with Optical Sensors. *The Journal of Physical Chemistry C* **113**, 15742-15750 (2009).

75. Huynh, L. et al. Evaluation of Phosphorescent Rhenium and Iridium Complexes in Polythionylphosphazene Films for Oxygen Sensor Applications. *Chemistry of Materials* **17**, 4765-4773 (2005).
76. Mays, J.E., Birch, J.B. & Einsporn, R.L. An overview of model-robust regression. *Journal of Statistical Computation and Simulation* **66**, 79 (2000).
77. Strawderman, W.E. Minimax Adaptive Generalized Ridge Regression Estimators. *Journal of the American Statistical Association* **73**, 623-627 (1978).
78. Lavagnini, I. & Magno, F. A statistical overview on univariate calibration, inverse regression, and detection limits: Application to gas chromatography/mass spectrometry technique. *Mass Spectrom. Rev.* **26**, 1-18 (2007).
79. Ji, S. et al. Real-time monitoring of luminescent lifetime changes of PtOEP oxygen sensing film with LED/photodiode-based time-domain lifetime device. *Analyst* **134**, 958 (2009).
80. Lu, X., Han, B. & Winnik, M.A. Characterizing the Quenching Process for Phosphorescent Dyes in Poly[((n-butylamino)thionyl)phosphazene] Films. *The Journal of Physical Chemistry B* **107**, 13349-13356 (2003).
81. Michaels, A.S. & Bixler, H.J. Solubility of gases in polyethylene. *J. Polym. Sci.* **154**, 393–412 (1961).
82. Bahadur, N.P., Shiu, W., Boocock, D.G.B. & Mackay, D. Temperature Dependence of Octanol–Water Partition Coefficient for Selected Chlorobenzenes. *Journal of Chemical & Engineering Data* **42**, 685-688 (1997).
83. Gouin, S. & Gouterman, M. Ideality of pressure-sensitive paint. II. Effect of annealing on the temperature dependence of the luminescence. *J. Appl. Polym. Sci.* **77**, 2805-2814 (2000).
84. Badocco, D. & Pastore, P. Definition and Use of the Experimental Sensible Parameters To Characterize Sensitivity and Precision of a Generic Oxygen Optical Sensor. *Analytical Chemistry* **80**, 2091-2096 (2008).
85. Lu, X. & Winnik, M.A. Luminescence Quenching in Polymer/Filler Nanocomposite Films Used in Oxygen Sensors. *Chemistry of Materials* **13**, 3449-3463 (2001).
86. Badocco, D., Mondin, A., Fusar, A. & Pastore, P. Calibration Models under Dynamic Conditions for Determining Molecular Oxygen with Optical Sensors on the Basis of Luminescence Quenching of Transition-Metal Complexes Embedded in Polymeric Matrixes. *The Journal of Physical Chemistry C* **113**, 20467-20475 (2009).
87. Mori, H., Niimi, T., Hirako, M. & Uenishi, H. Pressure sensitive paint suitable to high Knudsen number regime. *Meas. Sci. Technol.* **17**, 1242-1246 (2006).
88. Schappacher, G. & Hartmann, P. Partial Analytical Solution of a Model Used for Measuring Oxygen Diffusion Coefficients of Polymer Films by Luminescence Quenching. *Analytical Chemistry* **75**, 4319-4324 (2003).
89. Koo, Y.L. et al. Real-Time Measurements of Dissolved Oxygen Inside Live Cells by Organically Modified Silicate Fluorescent Nanosensors. *Analytical Chemistry* **76**, 2498-2505 (2004).
90. Stich, M.I., Borisov, S.M., Henne, U. & Schäferling, M. Read-out of multiple optical chemical sensors by means of digital color cameras. *Sensors and Actuators B: Chemical* **139**, 204-207 (2009).
91. Schroeder, C.R., Neurauter, G. & Klimant, I. Luminescent dual sensor for time-resolved imaging of pCO2 and pO2 in aquatic systems. *Microchim Acta* **158**, 205-218

(2007).

92. Fischer, L. et al. Red- and Green-Emitting Iridium(III) Complexes for a Dual Barometric and Temperature-Sensitive Paint. *Chem. Eur. J.* **15**, 10857-10863 (2009).
93. Lu, X., Han, B. & Winnik, M.A. Characterizing the Quenching Process for Phosphorescent Dyes in Poly[((n-butylamino)thionyl)phosphazene] Films. *The Journal of Physical Chemistry B* **107**, 13349-13356 (2003).
94. Wang, Z. et al. Microfluidic cooling of semiconductor light emission diodes. *Microelectronic Engineering* **84**, 1223-1226